

# **Investigating the Influence of Electron Extraction Layers on the Photostability of Inverted Organic Solar Cells**

by

Mozhgan Sadeghianlemraski

A thesis  
presented to the University of Waterloo  
in fulfillment of the  
thesis requirement for the degree of  
Doctor of Philosophy  
in  
Electrical and Computer Engineering (Nanotechnology)

Waterloo, Ontario, Canada, 2021

© Mozhgan Sadeghianlemraski 2021

## Examining Committee Membership

The following served on the Examining Committee for this thesis. The decision of the Examining Committee is by majority vote.

External Examiner	Zheng-Hong Lu Professor, Dept. of Materials Science & Engineering, University of Toronto
Supervisor(s)	Hany Aziz Professor, Dept. of Electrical & Computer Engineering, University of Waterloo
Internal Member	Dayan Ban Professor, Dept. of Electrical & Computer Engineering, University of Waterloo
Internal Member	Siva Sivoththaman Professor, Dept. of Electrical & Computer Engineering, University of Waterloo
Internal-external Member	Yuning Li Professor, Dept. of Chemical Engineering, University of Waterloo

## **Author's Declaration**

I hereby declare that I am the sole author of this thesis. This is a true copy of the thesis, including any required final revisions, as accepted by my examiners.

I understand that my thesis may be made electronically available to the public.

## Abstract

Decades of active research on organic solar cells (OSCs) have recently led to a significant increase in their power conversion efficiency (PCE). However, large-scale commercialization of the technology has not yet been realized, primarily due to the OSCs' short lifetimes. Generally, OSC degradation mechanisms can be categorized as extrinsic or intrinsic. In contrast to extrinsic degradation, which directly results from the cells being exposed to atmospheric species (oxygen and water), intrinsic degradation occurs even when OSCs are kept in an inert atmosphere and can proceed either in the dark or under illumination due to a variety of degradative processes. While extrinsic degradation can be adequately addressed by utilizing advanced encapsulation techniques and inverted device architecture, as well as by the discovery of novel active materials, the latter is still impeding progress.

In inverted OSCs, the bottom electrode (i.e., the one contacting the substrate) serves as an electron collection contact and is usually made of a transparent conductive oxide, mostly ITO, to allow for solar light collection. ITO, however, has a work function (WF) of  $\sim 4.7$  eV, which lies close to the middle of the bandgap of most organic active layer materials and thus can allow for undesirable hole collection. Therefore, in most cases, an electron extraction layer (EEL) is used in between the ITO electrode and active layers. The EEL, usually made of a solution-processable wide bandgap metal oxide, blocks the extraction of photogenerated holes from the active layer by the ITO and thus enhances the electron selectivity of the ITO/EEL contact. ZnO has been the most commonly used material for that purpose owing to its low toxicity, high electron mobility, inherent transparency, and its forming a large energy barrier against hole collection (often more than 1 eV). Despite these promising properties, one potential drawback of ZnO is its susceptibility to changes after irradiating by UV components in the solar spectrum. Therefore, alternative EEL materials are sometimes used.

Incorporating various materials as EELs has substantially advanced the improvement of OSC performance and lifetimes. However, there is still a need to gain a clearer fundamental understanding of the effect of EELs on the intrinsic photostability of OSCs and explore approaches for improving their lifetime. To this end, the research described in this thesis investigates the effects of EELs on intrinsic photostability by (i) studying ZnO, the most widely used EEL (as a reference cell), (ii) modifying ZnO EELs, and (iii) replacing ZnO EELs with alternatives.

The investigations on ZnO show that the ITO/ZnO and ZnO/bulk-heterojunction (BHJ) interfaces both influence photostability. Analysis of the surface potential and surface chemistry of contacts

indicate that the UV-induced losses of the chemisorbed oxygen on the ITO surface reduce its WF and thus decrease the contact selectivity. In addition, surface defects of ZnO and UV-induced increased charge trapping at these defects reduce the electron selectivity of the ITO/ZnO contact. The reduction in the electron selectivity increases surface recombination at the contact, reducing device photostability.

The work on modifying ZnO EELs investigates the effects of adding amine-containing materials in them either mixed with the ZnO or in a separate layer on photostability. Results show that mixing ZnO with the additive significantly reduces UV-induced changes in surface potential and WF and creates a new chemical interface that is electronically more stable. As a result, the electron collection efficiency remains stable under UV irradiation. Using the material in a separate layer enhances photostability by passivating ZnO surface defects, and consequently, preventing the UV-induced increased surface recombination that has been found to play a major role in the low photostability of ZnO cells.

The studies on replacing the ZnO EEL with alternatives involve pursuing large dipole moment materials (both polymeric or small molecular) as single layer EELs (DM-EELs). Results show that using DM-EELs suppresses the UV-induced increase in surface recombination observed in the ZnO cells and maintains the hole-blocking properties of the contact upon UV irradiation. The findings provide direct evidence of the importance of maintaining the charge selectivity of contacts to suppress surface recombination and enhance device photostability. A systematic study on degradation phenomena in fullerene-based and non-fullerene-based OSCs reveals that the dominant degradation mechanism is different in each case: photoinduced degradation in the first versus temporal degradation in the second. Regardless of the specific degradation mechanism, the directional dipole moment of the DM-EELs helps maintain charge selectivity irrespective of any UV-induced contact WF shifts. The findings show that using materials with large dipole moments in EELs can provide a universal route for enhancing the stability of inverted OSCs while allowing for green-solvent processability.

## Acknowledgments

This Ph.D. journey, with its numerous ups and downs, has indeed formed me both professionally and personally. A supportive group of people has helped me navigate this challenging journey, and I would like to thank them all.

First, I would like to express deep gratitude to my supervisor, Professor Hany Aziz, for his outstanding support, availability, and most importantly, his constructive and detailed feedback, which has significantly elevated my personal and professional growth. Notably, thank you for your excellent "Organic Electronics" course. I enjoyed every minute of your lectures, and I could not have done my research without the valuable insights and strong motivations gained from this course.

Next, I would like to acknowledge my advisory committee, Professor Siva Sivothythaman, Professor Yuning Li, and Professor Dayan Ban. I would also like to thank Professor Zheng-Hong Lu for accepting the role of my external Ph.D. examiner.

I am sincerely thankful for being in a lab, Giga-to-Nano, with supportive and handy people like Richard Barber and Dr. Czung-Ho Lee, our lab managers, and my colleagues, Mohammad Nouri, Dr. Mohsen Asad, Dr. Tyler Davidson-Hall, Dr. Hyeonghwa Yu, Dr. Yongjoo Cho, Elizabeth Salsberg, Dr. Jenner Ngai, Pankaj Kumar, Dr. Celal Con, Ahmed Elbaroudy, Viviane Nogueira Hamanaka, Peng Wang, Dong Seob Chung, Dr. Fatemeh Samaeifar, Atefeh Ghorbani Koltapeh, Mohsen Azadinia, and Junfei Chen.

I would like to extend my sincere thanks to the Graduate Student Association of the University of Waterloo (GSA-UW) and the University of Waterloo Writing and Communication Center for their tremendous impact on my wellness and professional growth.

I am deeply indebted to Mary McPherson and Grace Tang for their care, compassion, and kindness. I could not have stood firm in the first year of my immigration without your generosity and selflessness.

I cannot begin to express my thanks to my amazing mom and dad and my lovely sister, Masoumeh, for their unconditional support, kindness, and love. If not for your faith in me, I would not have made it this far. Mom and dad, your wise and compassionate parenting has had a powerful impact on my life, and you are the inspiration behind my endeavors and successes.

Last but not least, I especially thank my best friend, soul mate, and husband, Mohammad Nouri. Mohammad, thank you for being an excellent supporter and an effective listener, and for

unconditionally loving me, although these past years have not been an easy ride. I believe that the hardships of us both being international graduate students have strengthened our commitment to each other and our determination to succeed and given us the chance to live life to the fullest together.

Financial support from the Natural Sciences and Engineering Research Council of Canada (NSERC) Strategic Grants Program and from the NSERC-Green Electronics Network (GreEN) is gratefully acknowledged.

## **Dedication**

I dedicated this thesis to my love Mohammad and my beloved parents, Fatemeh and Ahmad, for their endless support and care.



## Table of Contents

Examining Committee Membership.....	ii
Author’s Declaration .....	iii
Abstract .....	iv
Acknowledgments .....	vi
Dedication .....	viii
List of Figures .....	xii
List of Tables.....	xix
List of Abbreviations.....	xx
Chemical Names.....	xxi
Chapter 1 Introduction.....	1
1.1 Motivation .....	1
1.2 Organic Semiconductors .....	3
1.2.1 Fundamentals of Organic Semiconductors.....	4
1.2.2 Electronic Transport in Organic Semiconductors .....	5
1.3 OSC Operational Principle and Active Layer Structures .....	7
1.3.1 Light Absorption .....	8
1.3.2 Exciton Diffusion .....	9
1.3.3 Exciton Dissociation.....	10
1.3.4 Charge Collection.....	13
1.4 Solar Cell Circuit Model and Photovoltaic Characteristics.....	19
1.4.1 Short-Circuit Current Density .....	20
1.4.2 Open-Circuit Voltage .....	20
1.4.3 Fill Factor .....	21
1.4.4 Power Conversion Efficiency.....	21
Chapter 2 Stability of OSCs .....	22
2.1 Introduction .....	22
2.2 Degradation Mechanisms in OSCs.....	22
2.2.1 Extrinsic Degradation.....	22
2.2.2 Intrinsic Degradation .....	25
2.3 Summary of Outstanding Issues.....	32
2.4 Thesis Objectives .....	33

Chapter 3 Experimental Procedures.....	35
3.1 Introduction.....	35
3.2 Device Geometry .....	38
3.3 Material Preparation and Device Fabrication .....	38
3.4 Device Characterization.....	40
3.4.1 Solar Simulator <i>J-V</i> Measurements.....	41
3.4.2 Light-Intensity-Dependent PV Characteristics .....	41
3.4.3 Low-Temperature Electrical Measurement.....	42
3.4.4 Atomic Force Microscopy .....	42
3.4.5 Kelvin Probe Force Microscopy .....	42
3.4.6 Absorption Spectra.....	44
3.4.7 Time-Resolved Transient Photoluminescence Spectroscopy .....	44
3.4.8 Photoelectron Emission Spectroscopy .....	44
Chapter 4 The Role of Introducing Polyethylenimine into the ZnO EEL on the Intrinsic Photostability of OSCs.....	47
4.1 Introduction.....	47
4.2 Results and Discussion .....	48
4.3 Conclusions.....	60
Chapter 5.....	61
The Effect of Modifying ZnO Surface with an N-annulated Perylene Diimide (PDIN-H) on the Intrinsic Photostability of OSCs .....	61
5.1 Introduction.....	61
5.2 Results and Discussion .....	62
5.3 Conclusion .....	75
Chapter 6.....	77
The Influence of Replacing ZnO with Polyethyleneimine as a Large Dipole Moment EEL on the Intrinsic Photostability of OSCs .....	77
6.1 Introduction.....	77
6.2 Results and Discussion .....	78
6.3 Conclusion .....	87
Chapter 7.....	88

The Effect of Replacing ZnO EELs with Green-Solvent Processable Molecules with Large Dipole Moments as a Universal Route for Enhancing Stability.....	88
7.1 Introduction .....	88
7.2 Results and Discussion.....	89
7.3 Conclusion.....	101
Chapter 8 .....	103
8.1 Summary of Main Conclusions .....	103
8.2 Suggestions for Future Work.....	104
Bibliography .....	106
Appendix A .....	117
Supplementary Information for Chapter 4 .....	117
Appendix B.....	118
Supplementary Information for Chapter 6 .....	118
Appendix C.....	120
Supplementary Information for Chapter 7 .....	120
Appendix D .....	125
Potential Benefits of Polyethyleneimine as an Electron Extraction Layer for Inverted Organic Solar Cells' Manufacturing.....	125
Introduction .....	125
Results and Discussion.....	126
Solvent-Robustness of PEI Film .....	126
Temporal stability of PEI film.....	129
Conclusions .....	131

## List of Figures

Figure 1. 1. Best research-cell efficiencies for various photovoltaic technologies plotted from 1976 to the present; confirmed by Natural Resource Energy Laboratory (NREL), adapted from [6].	2
Figure 1. 2. (a). Orbital bonding configuration of ethylene, illustrating the unique orientation of $\sigma$ - and $\pi$ -bonds. (b). Molecular orbital energy diagram of ethylene.	5
Figure 1. 3. Electronic structure for (a) organic semiconductors and (b) inorganic semiconductors. Band transport occurs within the continuous conduction band (CB) in (a), whereas hopping transport occurs between two adjacent molecules in (b).	6
Figure 1. 4. Main operational mechanisms of OSCs: (a). exciton generation by photon absorption, (b). exciton diffusion, (c). CT exciton formation and its dissociation at the interface, and (d). charge collection.	7
Figure 1. 5. Illustration of the three types of excitons based on the degree of charge delocalization: Frenkel exciton, charge-transfer exciton, and Wannier-Mott exciton.	8
Figure 1. 6. Illustration of the exciton diffusion process under $T = 4\text{ K}$ and $T = 300\text{ K}$ . The Gaussian density of states is represented by the distribution of the energies of excitonic states. (a) The downhill migration fully determines the exciton diffusion process at low temperatures. (b) At high temperatures, the thermally activated hopping also contributes to the exciton diffusion. Reproduced with permission from [21]. Copyright 2008, American Chemical Society.	9
Figure 1. 7. Common active layer structures of OSCs: (a) bilayer and (b) bulk-heterojunction layer.	11
Figure 1. 8. Chemical structures of some promising (a) donors and (b) acceptors used in OSCs.	12
Figure 1. 9. BHJ OSCs with (a) a conventional and (b) an inverted architecture.	14
Figure 1. 10. Schematic view of the energy level alignment in an inverted OSC with extraction layers providing ohmic contacts and charge selectivity. Reproduced from Ref.[38] with permission from the Royal Society of Chemistry.	15
Figure 1. 11. (a) Schematic of a single electric dipole with equipotential lines. (b) The potential distribution of an electric dipole layer. (c) An abrupt shift ( $\Delta$ ) in $E_{\text{vac}}$ , induced by an interfacial dipole layer, reducing the apparent work function of the electrode, $\Phi' = \Phi - \Delta$ . Reproduced with permission from [39]. Copyright 2020, American Chemical Society.	17
Figure 1. 12. Effects of interfacial dipole layers on the energy diagram. (a) and (b) are the energy levels of ITO and active layer before and after contact, respectively; (c) ZnO EEL, a representative of an n-type metal oxide with a deep valance band, facilitates electron transport while blocks holes; (d) ZnO/dipole-layer EEL, adding a dipole layer reduces the ZnO apparent WF and enhances the electron	

selectivity at the bottom contact; (e) ITO/Dipole layer, adding a dipole layer between the ITO and active layer can act as an EEL. Dipoles with positive charge end toward the active layer and negative charge end pointing toward ITO reduce the apparent WF of ITO and facilitate electron transport while blocks hole transports [39].	18
Figure 1. 13. (a) A simple equivalent circuit model for a solar cell. (b) Typical current density–voltage ( $J$ – $V$ ) characteristics for a solar cell in the dark and under illumination. Reproduced from Ref.[36], with permission from the Royal Society of Chemistry.	20
Figure 2. 1. The degradation pathways of ambient oxygen/water into OSCs. Reproduced with permission from [61]. Copyright 2020, Elsevier.	23
Figure 2. 2. Normalized $J_{sc}$ versus illumination time in an inert atmosphere for various polymer–fullerene OSCs. Reproduced from Ref.[92] with permission from the Royal Society of Chemistry.	27
Figure 2. 3. (a) Images of IT-4F thin films on glass, glass/ZnO, and glass/SnO <sub>2</sub> substrates under continuous UV illumination (365 nm, 5 mW.cm <sup>-2</sup> ). The UV-vis absorption spectra of (b) ZnO/IT-4F and (c) SnO <sub>2</sub> /IT-4F films upon AM1.5 illumination in a N <sub>2</sub> -filled atmosphere. Reproduced with minor changes from Ref.[102] with permission from the Royal Society of Chemistry.	30
Figure 2. 4. Schematic diagram of the mechanism of improved performance and stability with acid-treated ZnO films: (a) removal of surface hydroxyl groups on the ZnO surface and (b) regulation of vertical separation in the heterojunction films. Reproduced with permission from [32]. Copyright 2021, American chemical Society.	31
Figure 3. 1. (a) OSC structure used in this study, and (b) energy level diagram of the control device in this thesis with each layer's value derived from literature [117].	35
Figure 3. 2. The molecular structures of organic EELs used in this thesis.	37
Figure 3. 3. Schematic of the device geometry used in this thesis.	38
Figure 3. 4. Electronic energy levels of the sample and AFM tip in different conditions: (a) tip and sample are separated by distance $d$ with no electrical contact, (b) tip and sample are in electrical contact, and (c) external bias ( $V_{DC}$ ) is applied between tip and sample. $E_v$ , $E_{fs}$ , and $E_{ft}$ are the vacuum energy level, sample Fermi energy, and tip Fermi energy, respectively. Reproduced with permission from [127]. Copyright 2010, Elsevier.	43
Figure 3. 5. Illustration of the principles of XPS and UPS.	45

Figure 4. 1. a) A schematic depiction of the structure of the OSCs used in this work. b) $J$ - $V$ characteristics of OSCs with the highest PCE with the ZnO, ZnO/PEI, and ZnO:PEI EELs, measured under 1-sun AM1.5G illumination.....	48
Figure 4. 2. Normalized PCE (a), $V_{oc}$ (b), FF (c), and $J_{sc}$ (d) versus time under continuous UV irradiation of OSCs with the ZnO, ZnO/PEI, and ZnO:PEI EELs.....	51
Figure 4. 3. a) $J$ - $V$ characteristics collected in the dark for EODs with ZnO, ZnO/PEI, or ZnO:PEI contacts. Insets: the structure of EODs used in this work. b) Net change in the driving voltage ( $\Delta V$ ), defined as voltage needed to maintain a current density of 20 mA.cm <sup>-2</sup> at any time t minus the initial voltage at the same current density, under 5 h UV irradiation for the three contacts of interest. ....	52
Figure 4. 4. AFM (golden) and KPFM (blue) images of ITO Control, ZnO, ZnO/PEI, and ZnO:PEI films; before (a, b, and c, d respectively) and after 2 hours of UV irradiation (e, f, g, and h).....	54
Figure 4. 5. Average CPD versus time for the ITO, ITO/ZnO, ITO/ZnO/PEI, and ITO/ZnO:PEI samples. The samples were kept in the dark during the first 2 hours, exposed to UV irradiation during the next 2 hours, and then kept in the dark again during the last 28 hours. The height of each column represents the average value of 100 points on the sample surface.....	55
Figure 4. 6. XPS spectrum of (I). O 1s, and (II). Zn 2P, for pristine and UV-irradiated ZnO and ZnO:PEI films; at the surface (a and c), and at the ITO/EEL interface (b and d).....	59
Figure 5. 1. UV-Vis absorption spectra of pristine (solid lines) and 200 h UV-irradiated (dotted lines) of ZnO (black), ZnO/PDIN-H (blue), and PDIN-H (purple) films.....	63
Figure 5. 2. (a) $J$ - $V$ characteristics of the studied OSCs with the ZnO (black squares) and ZnO/PDIN-H (blue triangles) EELs, measured under 1-sun AM1.5G illumination. The inset shows the schematic depiction of the architecture of the studied OSCs. (b) $J$ - $V$ characteristics of electron-only devices with the two studied EELs. ....	64
Figure 5. 3. Normalized $V_{oc}$ (a), FF (b), $J_{sc}$ (c), and PCE (d) versus different time intervals of UV irradiation of OSCs with the ZnO (black squares) and ZnO/PDIN-H (blue triangles) EELs. Insets in (a) and (c) magnifies their trends in the 0-120 h time range. The right axis in (b) represents the normalized ideality factor of the cells versus the aging time extracted from their dark $J$ - $V$ curves, in the voltage range of 0.4-0.6 V. The sign of the ideality factors is flipped, and the curves are shifted to start from 1. The dotted lines in (d) indicate $T_{80}$ , where the PCE decreases to 80 % of its initial value. The error bars represent the standard deviation of each measurement. ....	65

Figure 5. 4. % change in PV parameters of OSCs with the ZnO (a) and ZnO/PDIN-H (b) EELs after UV illumination for 780 h and of a control set of identical OSCs that was kept in the dark (i.e., no UV) for the same period. Error bars represent the standard deviation in each measurement..... 66

Figure 5. 5. UV-Vis absorption spectra of pristine (solid lines) and 200 h UV-irradiated (dotted lines) P3HT:PC60BM coated on ZnO (black) and ZnO/PDIN-H (blue). ..... 67

Figure 5. 6. Dark  $J$ - $V$  characteristics of fresh and after different time intervals of UV irradiation of OSCs with ZnO (a) and ZnO/PDIN-H (b), on a semilogarithmic scale. The dotted vertical guides point to the voltage range from which the cells' dark ideality factors were extracted. .... 68

Figure 5. 7. Illuminated  $J$ - $V$  (a) and  $J \cdot dV/dJ$  against  $J$  of the dark  $J$ - $V$  characteristics under forward bias (b) of fresh (filled symbols) and 780 h UV-irradiated (open symbols) cells with the ZnO (black/grey squares) and ZnO/PDIN-H (blue triangles) EELs. The shunt and series resistance values extracted from the slope of the curves are written inside each figure. Error bars indicate the standard deviation of each measurement. .... 70

Figure 5. 8.  $J_{sc}$  (a) and FF (b) vs. light intensity of the fresh (filled symbols) and 780 h UV-irradiated (open symbols) cells with the ZnO (black/grey squares) and ZnO/PDIN-H (blue triangles) EELs. ... 72

Figure 5. 9. Ideality factors as a function of the voltage of the fresh (filled symbols) and 780 h UV-irradiated (open symbols) cells with the (a) ZnO and (b) ZnO/PDIN-H EELs. The black/grey squares represent the dark ideality factors ( $n_d$ ) derived from the dark  $J$ - $V$  characteristics. The red circles represent the light ideality factors ( $n_l$ ) from the open-circuit voltage's light-intensity-dependent characteristics. .... 73

Figure 5. 10. (a). UPS spectra of ITO/ZnO (black) and ITO/ZnO/PDIN-H (blue). (b). Secondary-electron cutoff regions and Fermi-edge regions. Work functions of ITO/ZnO and ITO/ZnO/PDIN-H are calculated as 4.46 eV and 3.89 eV, respectively. .... 75

Figure 6. 1. Schematic depictions of the structure of the P3HT:PC60BM-based BHJ OSCs (a) and PCDTBT:PC70BM-based BHJ OSCs, with the molecular structures of the materials used in the BHJ active layer in each case. ZnO or PEI is used as EELs in each case. Normalized PCE versus time under continuous UV illumination of OSCs with the ZnO and PEI EELs: (c) P3HT:PC60BM BHJ system; (d) PCDTBT:PC70BM BHJ system. Insets show the normalized  $V_{oc}$  versus time. .... 79

Figure 6. 2. Dark  $J$ - $V$  characteristics of the fresh (filled circles) and after different time intervals of UV irradiation (open circles) of OSCs with ZnO (blue circles), and PEI (red circles): (a) & (c) linear scale at reverse voltage; (b) & (d) semi-logarithmic scale at forward voltage; based on

P3HT:PC60BM OSCs (top), and PCDTBT:PC70BM OSCs (bottom). The blue arrows point to the order the characteristics were collected at the time of the aging. ....	82
Figure 6. 3. $J$ - $V$ characteristics of the fresh (filled circles) HODs and the same devices after different time intervals of UV aging (open circles) with ITO (a ), ZnO (b & d), and PEI (c & e), where only P3HT and PCDTBT is used as an organic layer without the addition of acceptor. Schematic depictions of the HODs are provided within each figure.....	84
Figure 6. 4. Illustration of the mechanism by which the UV-induced hole leakage through ITO (a) and ITO/ZnO (b) contacts occur; Blue arrows show the vacuum energy level variation after UV exposure. The hole-blocking functionality of ITO/PEI contact is also shown (c). ....	85
Figure 6. 5. $J_{sc}$ (a) and $V_{oc}$ (b) vs. light intensity of PCDTBT:PC70BM-based OSCs with ZnO (blue squares) and PEI (red squares) EELs. ....	86
Figure 7. 1. Architecture of the studied OSCs with the chemical structures of the Histidine and Sarcosine DM-EELs and of the P3HT:PC60BM and PM6:Y6 active layers. ....	89
Figure 7. 2. Normalized $V_{oc}$ , FF, $J_{sc}$ , and PCE versus different time intervals of UV irradiation of (a) P3HT:PC60BM and (b) PM6:Y6 OSCs, with the ZnO, Histidine, and Sarcosine EELs. ....	91
Figure 7. 3. $J_{sc}$ versus light intensity on a log-log scale of fresh vs. aged (a) P3HT:PC60BM and (b) PM6:Y6 cells with the ZnO, Histidine, and Sarcosine EELs. Aged means after UV-irradiation in case of (a) and after dark storage in case of (b). The lines represent the linear fits in each case.....	93
Figure 7. 4. Dark and light ideality factor values versus voltage of the fresh (filled symbols) and UV-irradiated (open symbols) P3HT:PC60BM OSCs with the ZnO, Histidine, and Sarcosine EELs. The black/grey squares represent the dark ideality factors ( $n_d$ ) derived from the dark $J$ - $V$ characteristics. The red circles represent the light ideality factors ( $n_l$ ) obtained from the $V_{oc}$ -light intensity characteristics.....	94
Figure 7. 5. Dark and light ideality factor values versus voltage of the fresh (filled symbols) and dark-stored (open symbols) of PM6:Y6 OSCs with the ZnO, Histidine, and Sarcosine EELs. The black/grey squares represent the dark ideality factors ( $n_d$ ) derived from the dark $J$ - $V$ characteristics. The red circles represent the light ideality factors ( $n_l$ ) obtained from the $V_{oc}$ vs. light intensity characteristics.....	96
Figure 7. 6. $J$ - $V$ characteristics of the electron-only devices with the structure of ITO/ZnO or Histidine/PC60BM/LiF/Al and (b) ITO/ZnO or Sarcosine/Y6/LiF/Al.....	97



Figure 7. 7. Normalized values of $J_{sc}$ , $V_{oc}$ , and FF of a) P3HT:PC60BM with the ZnO and Histidine EELs and PM6:Y6 OSCs with the ZnO and Sarcosine EELs. Values are extracted from fresh cells (as a reference) and from aged cells before and after replacing the electrodes ( $\text{MoO}_3/\text{Al}$ ). .....	98
Figure 7. 8. Dark $J$ - $V$ characteristics of the UV-irradiated and dark control P3HT:PC60BM OSCs with ZnO (a & b) and Histidine (c & d) EELs, measured at different temperatures. The $T = 140$ K and $T = 300$ K characteristics are presented together in (e) to facilitate comparison.....	100
Figure 7. 9. $n_d \ln(J_0)$ versus $1/K_B T$ plots, extracted from the dark $J$ - $V$ characteristics in Figure 7.8. ....	101
Figure S4. 1. C 1s and O 1s peaks of pristine and 2h-UV-irradiated ITO (left), and C 1s peaks of pristine and 2h-UV-irradiated ITO/ZnO and ITO/ZnO:PEI (right), at the surface versus at the ITO/EEL interface.....	117
Figure S6. 1. (a) & (c): Normalized FF, and (b) & (d) Normalized $J_{sc}$ , versus time under continuous UV illumination of OSCs with the ZnO (blue circles), and PEI (red circles) EELs; P3HT:PC60BM BHJ system (top), and PCDTBT:PC70BM BHJ system (bottom).....	118
Figure S6. 2. AFM images of the fresh and after different time intervals of UV aging of ZnO/P3HT:PC60BM (first row) and PEI/P3HT:PC60BM (second row). Roughness values are provided within each image.....	119
Figure S7. 1. Illuminated $J$ - $V$ characteristics of P3HT:PC60BM (red curve) and PM6:Y6 (blue curve) OSCs with the ZnO EEL. The cells were measured under 1-sun AM1.5G illumination.....	120
Figure S7. 2. Normalized $V_{oc}$ , FF, $J_{sc}$ , and PCE versus time of (a) P3HT:PC60BM and (b) PM6:Y6 OSCs with ZnO (blue squares), Histidine (green circles), and Sarcosine (red triangles) EELs. The cells were stored in a $\text{N}_2$ -filled atmosphere in the dark to serve as a control. ....	121
Figure S7. 3. AFM images of PM6:Y6 on a) ZnO, b) Histidine, and c) Sarcosine. Roughness values are shown in each image.....	121
Figure S7. 4. UV-Vis absorption spectra of PM6:Y6 films coated on a) ZnO, b) Histidine, and c) Sarcosine; collected from pristine samples, after storage in $\text{N}_2$ (solid blue line), after UV irradiation in $\text{N}_2$ (dotted blue lines) and air (red lines).....	122
Figure S7. 5. Normalized TRPL spectra of pristine and dark-stored a) ZnO/PM6, b) Histidine/PM6, and c) Sarcosine/PM6.....	122

Figure S7. 6. $V_{oc}$ versus the natural logarithm of light intensity of (a) P3HT:PC60BM (Fresh vs. UV-irradiated) cells and (b) PM6:Y6 (Fresh vs. Dark-stored) cells. Aged means after UV-irradiation in (a) and after dark storage in (b). .....	123
Figure S7. 7. Differential resistance ( $dV/dJ$ ) versus the applied voltage, extracted from dark $J$ - $V$ characteristics of PM6:Y6 OSCs with (a) ZnO, (b) Histidine, and (c) Sarcosine. Shunt and series resistance values were extracted at voltages around 0 V and above 0.8 V, respectively. The data is obtained from the fresh cells and after their storage in the dark. ....	124
Figure AD. 1. Schematic illustrations of the device fabrication sequence, including the solvent exposure process. ....	127
Figure AD. 2. Normalized $J_{sc}$ (a), $V_{oc}$ (b), FF (c), and PCE (d) versus time under continuous UV illumination of OSCs with pristine PEI (black squares), PEI soaked in 1-propanol (blue triangles), and PEI soaked in toluene (red circles). ....	128
Figure AD. 3. (a) N 1s spectrum for pristine ITO/PEI sample and ITO/PEI sample soaked in 1-propanol. (b) N 1s spectrum for ITO/PEI and glass/PEI samples.....	129
Figure AD. 4. Normalized $J_{sc}$ (a), $V_{oc}$ (b), FF (c), and PCE (d) versus time under continuous UV illumination of OSCs with the fresh PEI and N <sub>2</sub> -stored PEI EELs.....	130

## List of Tables

Table 4. 1. PV parameters of OSCs with the ZnO, ZnO/PEI (bilayer), and ZnO:PEI (mixture) EELs. .....	49
Table 4. 2. PV parameters of OSCs with ZnO:PEI EEL with different weight mixing ratios of (1:0.01), (1:0.02), (1:0.03), and (1:0.04). .....	49
Table 4. 3. % change in PV parameters of OSCs with the different EELs after 276 hours of UV irradiation and a control set of identical OSCs kept in the dark (i.e., no UV) for the same period.....	51
Table 5. 1. PV parameters of fresh and UV-irradiated solar cells with the ZnO and ZnO/PDIN-H EELs. ....	63
Table 6. 1. PV parameters of P3HT:PC60BM-based and PCDTBT:PC70BM-based OSCs with the ZnO and PEI EELs. ....	79
Table 7. 1. PV parameters of P3HT:PC60BM-based and PM6:Y6-based organic solar cells with the Histidine, Sarcosine, and ZnO EELs. ....	90
Table 7. 2. Shunt resistance obtained at voltages around 0 V and series resistance obtained at voltages above 0.9 V, both extracted from dark <i>J-V</i> characteristics of the PM6:Y6 OSCs with the different EELs. The data is obtained from the fresh cells and after storage in the dark. ....	96
Table S7. 1. Values of alpha ( $\alpha$ ), extracted from the slope of the linear fit in Figure 3. The Aged cells refer to the UV-irradiated cells for the P3HT:PC60BM case and the Dark-stored cells for the PM6:Y6 case. ....	123
Table AD. 1. PV parameters of OSCs with pristine PEI as a control, PEI soaked in 1-propanol, and PEI soaked in toluene. ....	127
Table AD. 2. PV parameters of organic solar cells with fresh and N <sub>2</sub> -stored PEI. ....	130

## List of Abbreviations

AFM	Atomic Force Microscopy
BHJ	Bulk Heterojunction
DM-EEL	Electron Extraction Layer with Large Dipole Moment
EL	Electroluminescence
EEL	Electron Extraction Layer
FF	Fill Factor
HEL	Hole Extraction Layer
HOMO	Highest Occupied Molecular Orbital
$J_{sc}$	Short-Circuit Current Density
KPFM	Kelvin Probe Force Microscopy
LUMO	Lowest Unoccupied Molecular Orbital
$n_d$	Dark Ideality Factor
$n_l$	Light Ideality Factor
OSC	Organic Solar Cell
PCE	Power Conversion Efficiency
PL	Photoluminescence
$R_s$	Series Resistance
$R_{sh}$	Shunt Resistance
UPS	Ultraviolet Photoelectron Spectroscopy
$V_{oc}$	Open-Circuit Voltage
WF	Work Function
XPS	X-ray Photoelectron Spectroscopy

## Chemical Names

ITO	Indium Tin Oxide
MDMO-PPV	Poly(2-methoxy-5-(30,70-dimethyloctyloxy)-1,4-phenylene vinylene
MEH-PPV	poly[2-methoxy-5-(2 ethylhexyloxy)-1,4-phenylenevinylene
MoO <sub>3</sub>	Molybdenum Trioxide
PCBM	[6,6]-phenyl-C61-butyric acid methyl ester
PCDTBT	Poly[N-9'-heptadecanyl-2,7-carbazole-alt-5,5-(4',7'-di-2-thienyl-2',1',3'-benzothiadiazole)], Poly[[9-(1-octylnonyl)-9H-carbazole-2,7-diyl]-2,5-thiophenediyl-2,1,3-benzothiadiazole-4,7-diyl-2,5-thiophenediyl]
PDI	Perylene Diimide
PDIN-H	N-annulated perylene diimide dye with a pyrrolic NH functional group
PEDOT:PSS	Poly(ethylenedioxythiophene):polystyrene sulfonate
PEI	Polyethyleneimine
PEIE	Polyethyleneimine Ethoxylated
P3HT	Poly(3-hexylthiophene-2,5-diyl)
PM6	Poly[(2,6-(4,8-bis(5-(2-ethylhexyl-3-fluoro)thiophen-2-yl)-benzo[1,2-b:4,5-b']dithiophene))-alt-(5,5-(1',3'-di-2-thienyl-5',7'-bis(2-ethylhexyl)benzo[1',2'-c:4',5'-c']dithiophene-4,8-dione)]
PTB7	Poly[[4,8-bis [(2-ethylhexyl)oxy]benzo[1,2-b:4,5-b']dithiophene-2,6-diyl][3-fluoro-2-[(2-ethylhexyl)carbonyl]thieno[3,4-b] thiophenediyl]]
TPBi	1,3,5-tris(2-N-phenylbenzimidazolyl)-benzene
Y6	2,2'-((2Z,2'Z)-((12,13-bis(2-ethylhexyl)-3,9-diundecyl-12,13-dihydro-[1,2,5]thiadiazolo[3,4-e]thieno[2'',3'':4',5']thieno[2',3':4,5]pyrrolo[3,2-g]thieno[2',3':4,5]thieno[3,2-b]indole-2,10-diyl)bis(methanylylidene))bis(5,6-difluoro-3-oxo-2,3-dihydro-1H-indene-2,1-diylidene))dimalononitrile



# Chapter 1

## Introduction

### 1.1 Motivation

Climate change and the significant increase in global temperatures demand a rapid transformation of our energy supply system. Photovoltaic (PV) technology, a vital source of renewable energy generation, is helping to address this challenge. The International Energy Agency predicts that, by 2050, 16% of the world's electricity will be provided by PV systems [1]. Notably, from 2008 to 2018, global photovoltaic electricity generation saw 50% annual growth [2]. Maintaining this annual growth for nine additional years would mean producing ~34,000 TWh, more than the predicted global electricity demand [2].

In PV technology, electric power is generated using solar cells, which convert energy from the sunlight into electricity by the photovoltaic effect. The goal of providing low-cost, efficient, and stable solar electricity has led to the development of different PV technologies during the last decades [3]. **Figure 1.1** provides the best efficiencies of research cells using different technologies, confirmed by the National Research Energy Laboratory (NREL). The first solar cell, a mono-crystalline Si cell, developed in 1954 by Chapin et al. [4], exhibited a power conversion efficiency (PCE) of 6 %. The mono-crystalline Si solar cell is archetypical of semiconducting p-n junction technology, named 1st-generation PV technology, which eventually has exceeded 27 % PCE (**Figure 1.1**) and is environmentally and intrinsically very stable [3]. However, massive material use, high manufacturing thermal budgets, and recycling complexities in these solar cells resulted in the emergence of alternatives, the 2<sup>nd</sup>-generation or thin-film PV technology. Amorphous Si solar cells are the most typical representative of the 2<sup>nd</sup>-generation technology. Although advantageous in manufacturing costs and complexities, amorphous Si cells suffer from inferior performance and stability. By contrast, other 2<sup>nd</sup>-generation solar cell systems, copper indium diselenide (CIS)/copper indium gallium diselenide (CIGS) and cadmium sulfide (CdS)/cadmium telluride (CdTe) solar cells, exhibit outstanding performance (~23 % PCE) and good stability. Yet, the scarcity and toxicity of their constituents triggered the pursuit of a 3<sup>rd</sup>-generation technology, which encompasses a wide range of material and device structures, such as dye-sensitized solar cells (DSSC), organic solar cells (OSCs), quantum dot solar cells, and perovskite solar cells [3]. So far, no single technology meets all requirements, and further research is still necessary for large-scale production.

After extensive research on DSSC solar cells, they have been almost completely dismissed due to low performance (maximum PCE of 12 %) and instability issues (mainly due to the use of a liquid electrolyte). Perovskite cells have recently become more popular because of their low-cost fabrication methods and high efficiency (~25%). However, their low ambient stability and having toxic elements have become their Achilles' heel. Therefore, researchers are currently working on nontoxic alternatives and stability-enhancement approaches [5].

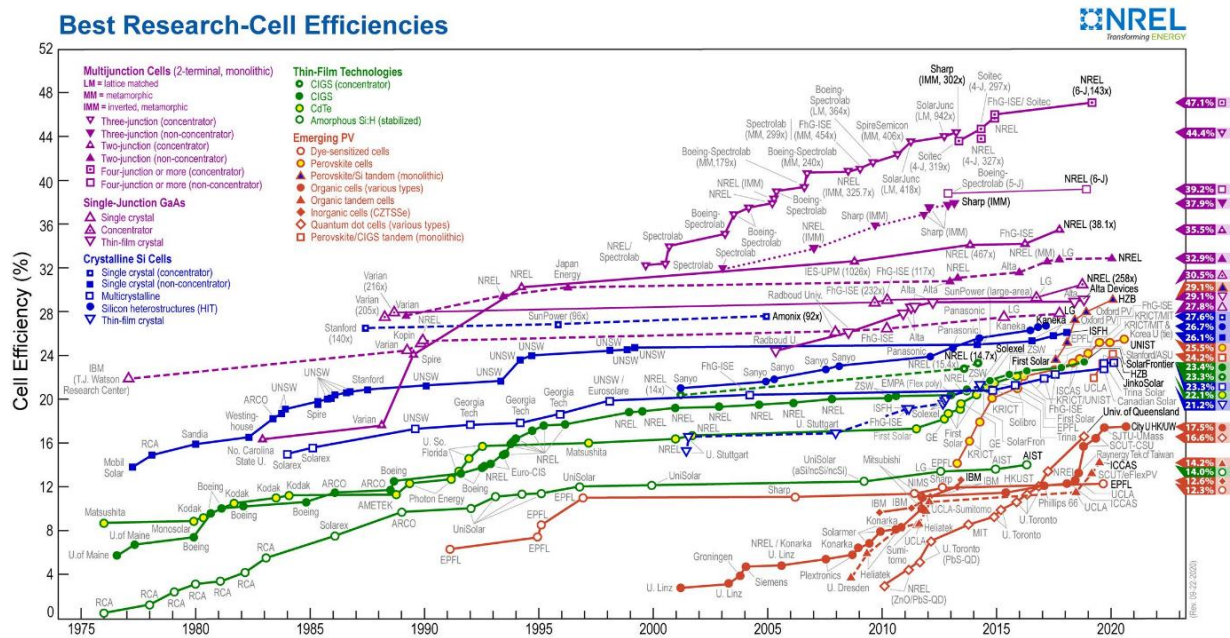


**Figure 1. 1.** Best research-cell efficiencies for various photovoltaic technologies plotted from 1976 to the present; confirmed by Natural Resource Energy Laboratory (NREL), adapted from [6].

Recently, OSCs have attracted enormous interests thanks to their low-temperature manufacturing, non-toxicity, low carbon footprint, easy recycling, mechanical flexibility, and compatibility with low-cost mass-production fabrication technology [7-11]. As the cost of Si continues to fall, OSCs' flexibility and ability to be transparent (promising for windows integration), as opposed to their cost-effectivity, enable OSCs to fill a niche that Si cells cannot easily fill; OSCs are being suggested as a remarkable candidate for building-integrated photovoltaics [5]. Despite these unique advantages, the mass-scale application of this technology has been impeded by the relatively limited efficiency and stability. Early OSCs consisted of a simple metal/organic/metal structure (organic Schottky cell), which exhibited poor PCE (0.10%) [12]. In 1986, Tang [13] increased the PCE to 1% with a bilayer OSC consisting of copper



phthalocyanine (CuPc) and a perylene derivative. After that, the invention of bulk-heterojunction (BHJ) active layers (will be explained in section 1.7) has led to a substantial PCE enhancement. Since then, several advancements have been made, and PCEs of BHJ devices are now reaching 17% in a single junction cell [14], as indicated in **Figure 1.1**. Despite a vast body of work on improving efficiency, the stability issue has not been adequately addressed, although it has recently drawn attention. It is therefore imperative to investigate the causes of low stability and improve the lifetime of OSCs.

This thesis addresses the urgent topic by investigating certain degradation mechanisms leading to the low stability of OSCs, with a particular focus on intrinsic OSC photostability in an inert atmosphere (which will be further discussed in Chapter 2). The thesis is organized into eight chapters. Chapter 1 provides an introduction to organic semiconductors, OSCs, and their equivalent circuit model. Chapter 2 reviews prior and existing work on OSCs' degradation mechanisms and strategies to mitigate them and outlines the objectives of this study. Chapter 3 outlines the fabrication methodologies and intended characterization techniques used in this study. Chapter 4 and 5 discuss the effect of modifying ZnO on contact photodegradation and the intrinsic photostability of OSCs. Then, Chapter 6 explains the effects of replacing the ZnO with polyethyleneimine (PEI). Chapter 7 examines the effect of Histidine and Sarcosine. Finally, Chapter 8 summarizes the main findings of this work along with the recommendation for future work.

## 1.2 Organic Semiconductors

High electrical conductivity in an organic semiconductor (doped polyacetylene) was discovered in 1977 [15]. Since then, extensive research has been dedicated to exploring organic semiconductors, bringing on their applications in light-emitting diodes, transistors, and solar cells. Due to their inherent technological advantages over inorganic semiconductors, such as low cost, lightweight, flexibility, and compatibility with roll-to-roll fabrication methods, the application of organic semiconductors gained a particular interest in OSC technology. Organic semiconductors constitute the light-absorbing layer of OSCs. Other layers of OSCs can also be made of organic materials. This section, therefore, first discusses the electrical and physical properties of organic semiconductors to better understand and study OSCs. Section 1.2.1 covers the basic definition, the origin of the electronic structure, and the classification of organic semiconductors. Section 1.2.2 discusses electronic transport in organic semiconductors.

## 1.2.1 Fundamentals of Organic Semiconductors

Organic semiconductors are solids with  $\pi$ -conjugated molecules or polymers that consist of carbon, hydrogen, and heteroatoms such as nitrogen, oxygen, and sulfur. The molecular structures of  $\pi$ -conjugated systems have alternating carbon-containing single and double bonds [16]. Carbon atoms have four valence electrons and thus need four extra electrons to fill their valence shells. When two carbon atoms are next to each other, the large overlap of 2s-2p hybrid atomic orbitals ( $sp^1$ ,  $sp^2$ , or  $sp^3$ ) creates  $\sigma$ -bonds, whereas  $\pi$ -bonds are formed by an adequate overlap of similar, adjacent p atomic orbitals. In general, contrary to the localized electrons in strong  $\sigma$ -bonds, the  $\pi$ -electrons are mostly delocalized. Interaction of two atomic orbitals creates two molecular orbitals (MOs): (i) bonding-orbital, formed by overlapping in-phase orbitals and has energy lower than its constituent atomic orbitals, and (ii) anti-bonding orbital, which is made up of overlapping out-of-phase atomic orbitals and has higher energy than the atomic ones.

**Figure 1.2** shows orbital configuration in an ethene (ethylene) molecule ( $C_2H_4$ ), the simplest  $\pi$ -conjugated system with covalent bonds. As shown in **Figure 1.2.a**, ethylene consists of a C-C  $\sigma$ -bond (overlapping of  $sp_x^2$  hybridized orbitals), four C-H  $\sigma$ -bonds (overlapping of C  $sp^2$  with H 1s orbitals, in the XY direction), and a  $\pi$ -bond (overlapping of  $p_z$  orbitals) [17]. The combination of a  $\sigma$ -bond and a  $\pi$ -bond in ethylene forms a double bond. The large overlapping within the  $\sigma$ -bonds yields strong bonding ( $\sigma$ ) and antibonding ( $\sigma^*$ ) MOs [16]. By contrast, interactions form the  $\pi$ -bonds are weaker due to the dumbbell shape of the  $p_z$  orbitals, and hence form weaker bonding ( $\pi$ ) and antibonding ( $\pi^*$ ) MOs, making the  $\pi$ - $\pi^*$  transition the smallest possible electronic excitation within the molecule, schematically depicted in **Figure 1.2.b** [16]. The  $\pi$ -bonding and  $\pi^*$ -antibonding MOs are named “highest occupied molecular orbital (HOMO)” and “lowest unoccupied molecular orbital (LUMO),” respectively. HOMO and LUMO are respectively analogous to the valence band (VB) and conduction band (CB) in inorganic semiconductors and determine the electrical and optical properties of organic solids. In the ground state, all bonding orbitals up to the HOMO are filled with a maximum of two electrons with opposite spins per orbital, whereas all antibonding orbitals (from the LUMO onwards) are empty. The energy difference between HOMO and LUMO determines the bandgap, typically between 1.5 eV and 3.5 eV for organic semiconductors [16].

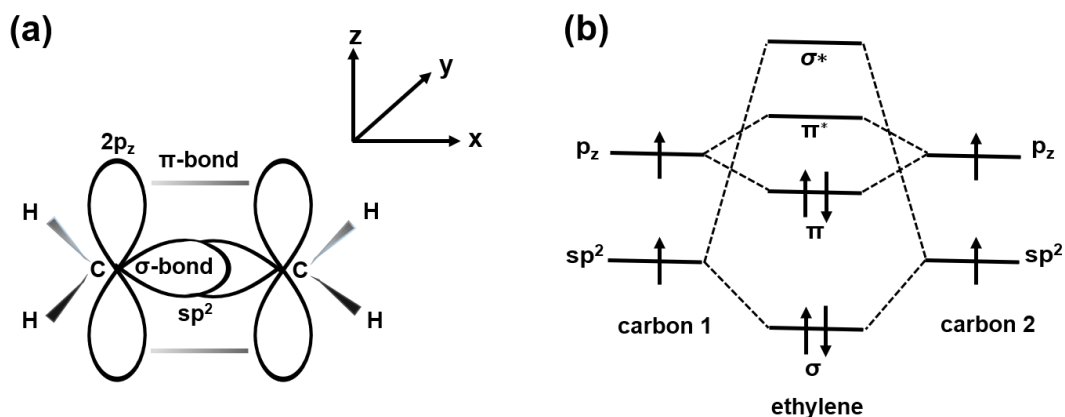


**Figure 1. 2.** (a). Orbital bonding configuration of ethylene, illustrating the unique orientation of  $\sigma$ - and  $\pi$ -bonds. (b). Molecular orbital energy diagram of ethylene.

Organic semiconductors can be divided into two groups; small molecules and polymers. Small molecules, the simplest type of organic solids, are low molecular weights organic compounds with identical structures. They benefit from easier purification processes, higher film crystallinity, and distinct chemical structures. Polymers are high molecular weight species composed of long chains of repeating units with a carbon-containing backbone. In comparison to small molecules, polymers normally have higher viscosities, boiling points, and mechanical strength. Since most small molecules have low molecular weights, they do not adhere strongly to the underlying layer. As a result, easy erosion of small molecule layers occurs during solution coating of the next layer. Therefore, small molecules are processed mostly through thermal deposition. In contrast, as polymers' decomposition temperature is less than their evaporation temperature, they cannot be deposited with thermal evaporation. Instead, polymers are easily solution-processable, making them suitable for flexible electronics.

### 1.2.2 Electronic Transport in Organic Semiconductors

Generally, intermolecular electronic charge transport in organic solids can be categorized into band transport and hopping transport. In inorganic solids, small distances and strong interactions between atoms creates continuous bands (CB and VB) in which charges are highly delocalized (**Figure 1.3.a**). As a result, carrier transport is considered as the free-carrier motion (assigning an effective mass), with electric-field-independent mobility (typically greater than 100 cm<sup>2</sup>V<sup>-1</sup>s<sup>-1</sup>). In crystalline organic

semiconductors with highly-ordered molecular crystals (such as pentacene and rubrene), charges are sufficiently delocalized (similar to inorganic semiconductors), and thus band transport occurs. However, in less-crystalline or amorphous materials, intermolecular transport is limited by weak Van der Waals intermolecular coupling among molecules, causing significant localization of charge carriers in individual molecules [16]. In addition, the high degree of disorder in amorphous solids leads to a Gaussian distribution of HOMO and LUMO energy states, as opposed to forming continuous bands. Consequently, as illustrated in **Figure 1.3.b**, transport occurs through the hopping of carriers among this Gaussian density of states (DOS), with limited charge carrier mobility ( $10^{-5}$  to  $10^{-2}$   $\text{cm}^2 \text{V}^{-1}\text{s}^{-1}$  range for photovoltaic materials). In the materials in this study, hopping transport is the dominant mechanism.

For hopping to occur, charge carriers must overcome an energy barrier needed to move from one molecule to the next. As a result, charge mobility depends on the energy barrier height, electric field, and temperature and is usually modeled by Poole Frankel model (Equation (1-1)) [16]:

$$\mu(F, T) \propto \exp\left(\frac{-E_A}{k_B T}\right) \cdot \exp\left(\frac{-\beta\sqrt{F}}{k_B T}\right), \quad \text{Equation 1- 1}$$

where  $k_B$  is the Boltzmann constant,  $F$  is the electric field,  $T$  is the temperature,  $E_A$  is the energy barrier height, and  $\beta$  is a material-dependent constant.

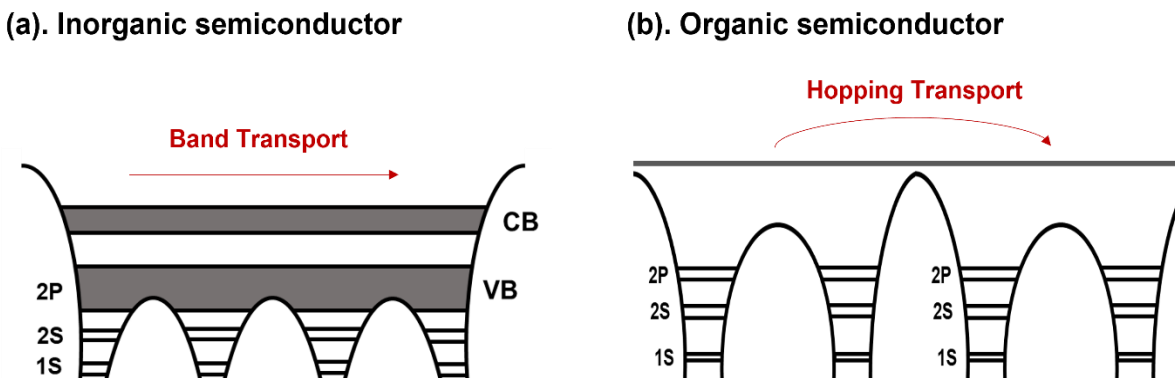


**Figure 1. 3.** Electronic structure for (a) organic semiconductors and (b) inorganic semiconductors. Band transport occurs within the continuous conduction band (CB) in (a), whereas hopping transport occurs between two adjacent molecules in (b).

In organic semiconductors, weak intermolecular interactions and the relatively long residence time of charges on a molecule result in stronger intermolecular coupling between electrons and phonons (a quantum of vibration). As a result, the residence of a charge in a molecule causes a significant polarization or deformation of its surrounding. A charge carrier (i.e., electron or hole) combined with its caused molecular distortion is called a polaron. The polaron is essentially a trapped charge carrier, which governs electrical conduction. Conduction requires the polarons to hop from one molecule to another [18].

### 1.3 OSC Operational Principle and Active Layer Structures

The basic principle of an OSC operation can be described by four main steps [19] (**Figure 1.4**):

- a. Upon photon absorption, an exciton is generated.
- b. The exciton diffuses toward a donor (D)-acceptor (A) interface.
- c. A charge-transfer (CT) exciton creates at the D/A interface and gets dissociated, creating free carriers.
- d. Free photogenerated carriers drift toward the respective electrodes, where they are collected.

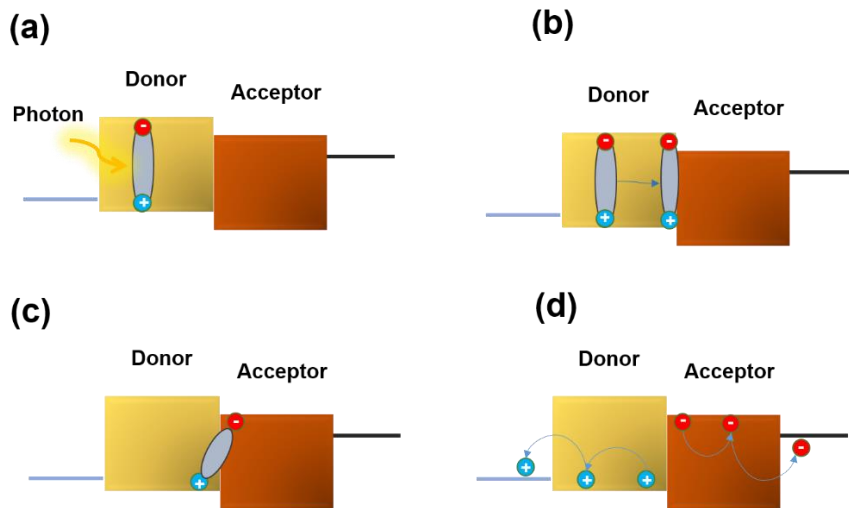


**Figure 1. 4.** Main operational mechanisms of OSCs: (a). exciton generation by photon absorption, (b). exciton diffusion, (c). CT exciton formation and its dissociation at the interface, and (d). charge collection.

### 1.3.1 Light Absorption

The first step of the operational mechanism in every OSC is the absorption of a photon by exciting an electron (**Figure 1.4.a**). In organic semiconductors, the electron is excited from the HOMO to the LUMO ( $\pi$ - $\pi^*$  transition) and binds with the hole left behind in the HOMO, creating an exciton.

The degree of charge delocalization and the strength of the e-h binding energy in materials lead to three types of excitons: Frenkel, CT, and Wannier-Mott, as shown in **Figure 1.5**. In organic semiconductors, limited charge delocalization and small dielectric constant result in a small Bohr radius, and thus the excitons have a very large binding energy and are located on a single molecule, forming Frenkel excitons. In addition to the unimolecular Frenkel excitons, CT excitons, with electrons and holes on adjacent molecules (bimolecular), are often formed. In contrast, in inorganic semiconductors, Wannier-Mott excitons form due to large dielectric constant and thus long-distance delocalization of charges. Unlike large binding energies of Frenkel and CT excitons ( $\geq 0.1$  eV), Wannier-Mott binding energies are only a few meV, and hence can be dissociated at room temperatures by thermal energy; thereby, inorganic solar cells are not considered “excitonic.”

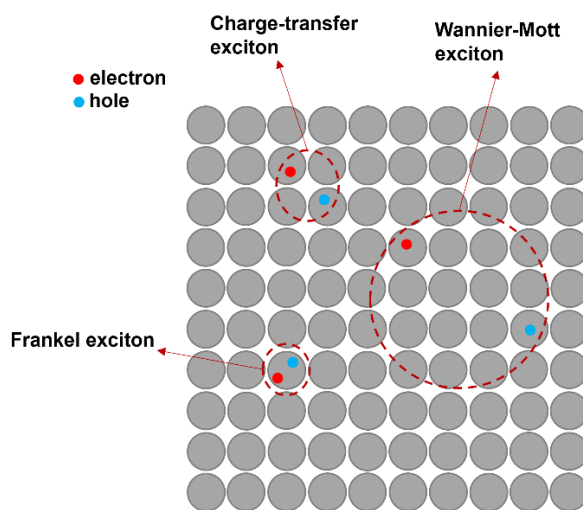


**Figure 1. 5.** Illustration of the three types of excitons based on the degree of charge delocalization: Frenkel exciton, charge-transfer exciton, and Wannier-Mott exciton.

### 1.3.2 Exciton Diffusion

After exciton generation in the donor or acceptor, it has to move toward a D/A interface. Excitons cannot drift under an applied electric field within a solid as they are charge neutral. Instead, they diffuse through a material via energy transfer processes [20]. During an energy transfer process, one pre-excited molecule transfers its excitation to another molecule. Eventually, the first molecule resides in the ground state while the second molecule is in the excited state. The high degree of disorder in most organic films, especially the solution-processed ones (active layers through this thesis), induces a Gaussian distribution of HOMO and LUMO energy states. As a result, energy transfers occur through random hopping between these disordered states, and hence, are regarded as a diffusion motion. **Figure 1.6** schematically shows the exciton diffusion in a disordered medium, with a Gaussian distribution of energy states (distribution width  $\sigma$ ), at two different temperatures. Upon photon absorption, an exciton is generated at a conjugated segment with a specific energy. At low temperatures ( $T \leq 150$  K), the exciton migrates downhill to an available conjugated segment with lower energy (**Figure 1.6.a**). This downward migration of excitons continues until reaching a quasi-equilibrium level of the most populated states, located at  $-\sigma^2/KT$  below the center of the Gaussian DOSs [21]. In contrast, at temperatures above 150 K, after initial downhill migration, thermally activated hopping occurs between similar energy states with almost constant distance.

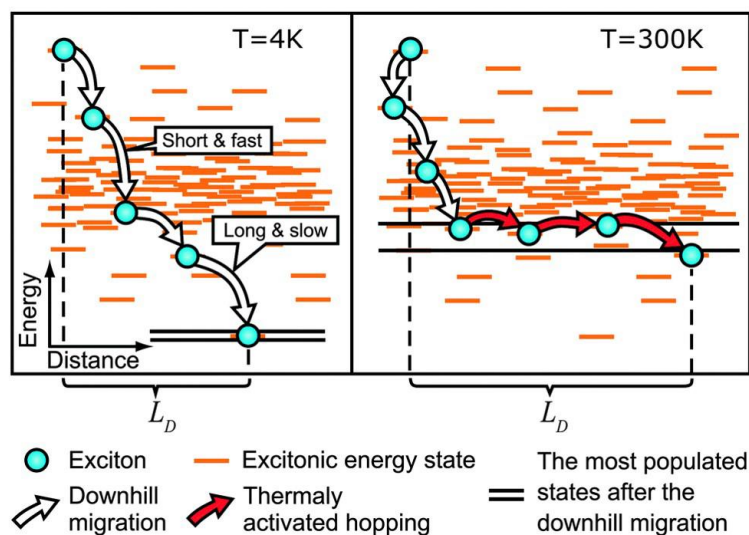


**Figure 1. 6.** Illustration of the exciton diffusion process under  $T = 4$  K and  $T = 300$  K. The Gaussian density of states is represented by the distribution of the energies of excitonic states. (a) The downhill migration fully determines the exciton diffusion process at low temperatures. (b) At high temperatures, the thermally activated hopping also contributes to the exciton diffusion. Reproduced with permission from [21]. Copyright 2008, American Chemical Society.

### 1.3.3 Exciton Dissociation

As discussed earlier, in organic semiconductors, for separating excitons (Frankel and CT) into free carriers, an energy larger than the exciton binding energy (0.3 – 0.4 eV) is required, much larger than the average thermal energy in the system ( $kT$  @300K = 25.9 meV,  $k$  is the Boltzmann constant, and  $T$  is temperature). Thus, an extra driving force is needed for dissociation.

Early OSCs consisted of a single light absorber layer, known as an active layer, embedded between electron collection and hole collection electrodes (called organic Schottky solar cell) [12]. Devices based on this structure gave poor PCE ( $\leq 0.10\%$ ) as they relied only on the built-in electric field induced by the work-function (WF) difference of the electrodes for exciton dissociation, which needs a larger driving force in organic solids [12]. To address this challenge, in 1986, Tang [13] introduced a bilayer OSC that consists of two distinct layers of organic small molecules; the first acted as an electron donor while the second acted as an electron acceptor. The donor and acceptor were selected such that the energy offset between the donor's and acceptor's LUMO makes transferring of an electron from the donor to the acceptor energetically favorable, enabling exciton dissociation.

The exciton dissociation mechanism involves two steps; (1) a Frenkel exciton relaxes first to a CT exciton state by electron transfer to the acceptor's LUMO. The CT formation releases excess vibrational energy. If this extra energy is equal to or larger than the CT binding energy, it may transfer back to the CT exciton, dissociating it into free charge carriers. Notably, due to larger intermolecular distances in organic solids, the intramolecular vibrations prevail for the exciton dissociation than the intermolecular vibrations. The exciton dissociation rate depends on the exciton binding energy, LUMO offset between donor and acceptor, molecular vibrational energy generated by Frenkel to CT exciton relaxation, excitonic Bohr radius, and the dielectric constant of the donor material [22]. As a rough guide, the available exciton dissociation energy is determined by the energy offset between the LUMOs of the donor and acceptor at their interface [23]. Thus, to ensure that all photogenerated excitons can reach the D/A interface to generate unbound charges, the excitons should be created within an exciton diffusion length from the interface. On the other hand, the typical exciton diffusion length in many organic materials is around 5-20 nm [24], while the thickness required to absorb most of the incident light is significantly larger ( $\geq 100$  nm). It means that excitons created far from the D/A interface do not contribute to photogeneration.



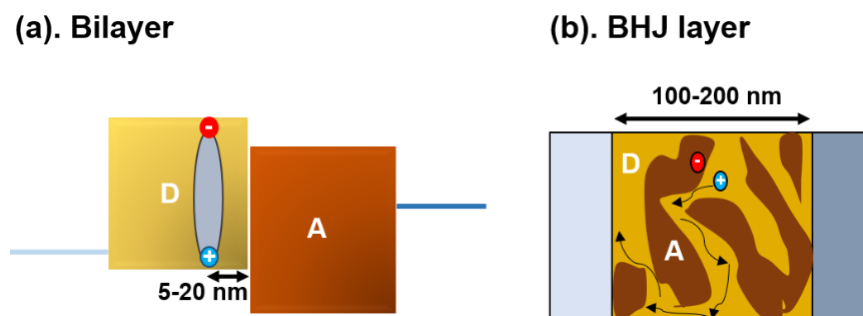


**Figure 1. 7.** Common active layer structures of OSCs: (a) bilayer and (b) bulk-heterojunction layer.

### 1.3.3.1 Bulk Heterojunction OSC

To overcome the exciton dissociation problem caused by the limited exciton diffusion length, Yu et al. [25] introduced the bulk heterojunction (BHJ) active layer, which consists of an intimately intermixed blend of donor and acceptor phases, as shown in **Figure 1.7**. This interdigitated blend enables the photogenerated excitons to easily find a heterojunction interface within their diffusion length throughout the whole BHJ layer. As a result, this structure allows for an optically thick active layer (~100 nm-200 nm) [26]. Efficient exciton dissociation occurs when the BHJ intermixing provides sufficient D/A interfacial areas. For preparing the BHJ layer, both donor and acceptor materials are dissolved in the same solvent, then cast as a single blended layer, followed by post-deposition thermal annealing. This process yields an interpenetrating network of donors and acceptors with bi-continuous phase separation. An optimized BHJ morphology usually consists of three phases; an aggregated polymer phase, an aggregated fullerene phase, and an amorphous phase of intermixed polymer and fullerene.

### 1.3.3.2 Promising Donor and Acceptor Materials

For donor and acceptor choice, various material combinations have been used so far. **Figure 1.8** provides the chemical structures of some of the most famous materials used in OSCs. For donor polymers, poly (phenylene vinylene) (PPV) derivatives, namely poly[2-methoxy-5-(2 ethylhexyloxy)-1,4-phenylenevinylene (MEH-PPV) and poly(2-methoxy-5-(30,70-dimethyloctyloxy)-1,4-phenylene vinylene (MDMO-PPV), was widely used from the mid-1990s till the early 2000s. The most widely used acceptor was buckminsterfullerene (C60) derivatives, owing to its deep LUMO level, high

electron mobility, and efficient charge separation kinetics combined with donor polymers. Since 2002, when poly(3-hexylthiophene-2,5-diyl) (P3HT) was first introduced, it shifted the focus from PPV-based polymers, thanks to its higher hole mobility ( $\sim 0.1 \text{ cm}^2\text{V}^{-1}\text{s}^{-1}$ ) and proper morphology control. Notably, P3HT: [6,6]-Phenyl-C61-butyric acid methyl ester (PC60BM) combination has been the "best seller" in polymer photovoltaic research for almost a decade [27], and the efficiency of its BHJ OSCs has been improved markedly. Since then, a large variety of donors and acceptors have been continuously emerging. Poly[N-9'-heptadecanyl-2,7-carbazole-alt-5,5-(4',7'-di-2-thienyl-2',1',3'-benzothiadiazole)], Poly[[9-(1-octylnonyl)-9H-carbazole-2,7-diyl]-2,5-thiophenediyl-2,1,3-benzothiadiazole-4,7-diyl-2,5-thiophenediyl] (PCDTBT), with a low-lying HOMO of -5.5 eV and relatively greater coverage of solar spectrum gained attention because of their outstanding performance, the highest efficiency at the time. The polymer has been mostly blended with [6,6]phenyl- C71-butyric acid methyl ester (PC70BM), a higher adduct of PC60BM that increases the absorption range and thus the photocurrent [28]. Then, another novel donor polymer poly[[4,8-bis [(2-ethylhexyl)oxy]benzo[1,2-b:4,5-b']dithiophene-2,6-diyl][3-fluoro-2-[(2-ethylhexyl)carbonyl]thieno[3,4-b] thiophenediyl]] (PTB7) with a high hole mobility of  $5.8 \times 10^{-4} \text{ cm}^2\text{V}^{-1}\text{s}^{-1}$  also blended with PC70BM to achieve a better coverage of the solar spectrum, have made it one of the most popular donor materials [28].

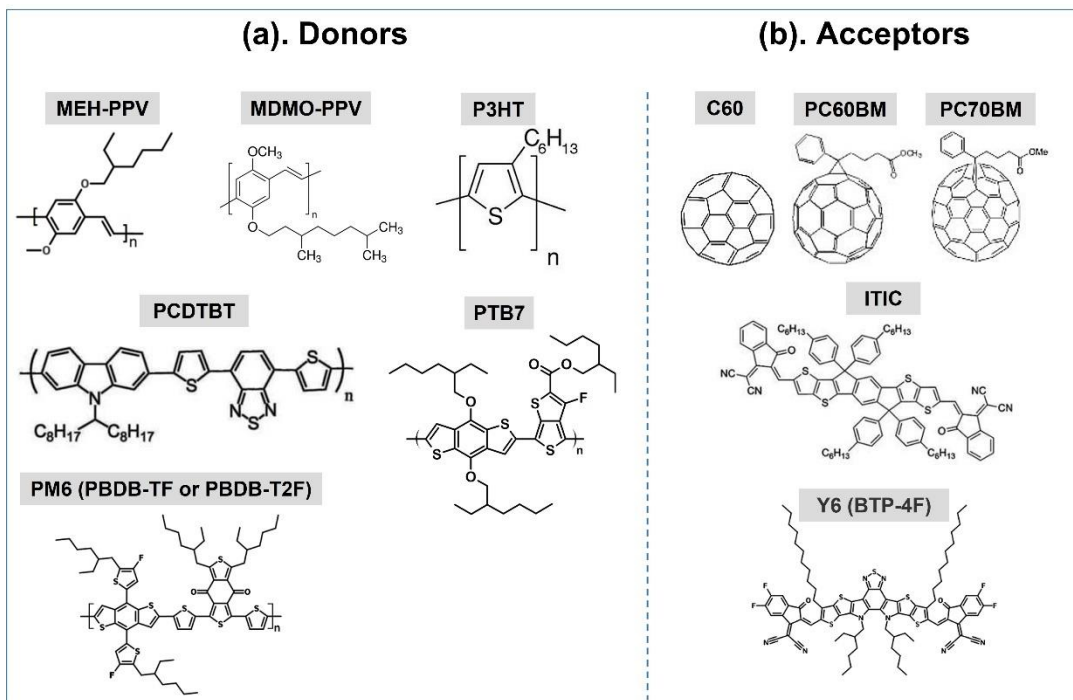


**Figure 1. 8.** Chemical structures of some promising (a) donors and (b) acceptors used in OSCs.

Although designing novel polymers led to an increase in efficiency to a great extent, further improvement was not feasible due to the limitations of donor:fullerene systems, namely the weak contribution of fullerene in harvesting solar light, non-complementary absorption with donors [29], and photodimerization (will be further discussed in Chapter 2). Recently, properly addressing fullerene limitations, the invention of non-fullerene acceptors (NFA), electron-accepting small molecules, has led to a significant improvement in device efficiency. The first NFA that outperforms the fullerene counterparts is 2,2'-[[[6,6,12,12-Tetrakis(4-hexylphenyl)-6,12-dihydrodithieno[2,3-d':2',3'-d']-s-indaceno[1,2-b:5,6-b']dithiophene-2,8-diyl]bis[methylydyne(3-oxo-1H-indene-2,1(3H)-diylidene)]]bis[propanedinitrile] (ITIC). Two main merits of ITIC are: its favorable energy level alignment with low band-gap polymers, which enhances charge separation efficiency, and its strong and broad absorption from visible to near-infrared (peaking at 700 nm), which increases the absorption [30]. Zhang et al.[31] synthesized Poly[(2,6-(4,8-bis(5-(2-ethylhexyl)-3-fluoro)thiophen-2-yl)-benzo[1,2-b:4,5-b']dithiophene))-alt-(5,5-(1',3'-di-2-thienyl-5',7'-bis(2-ethylhexyl)benzo[1',2'-c:4',5'-c']dithiophene-4,8-dione)] (PM6, also named PBDB-TF or PBDB-T2F), which has been proved to be a star polymer donor and can be mixed with different NFAs. Mixing PM6 with 2,2'-((2Z,2'Z)-((12,13-bis(2-ethylhexyl)-3,9-diundecyl-12,13-dihydro-[1,2,5]thiadiazolo[3,4-e]thieno[2'',3':4',5']thieno[2',3':4,5]pyrrolo[3,2-g]thieno[2',3':4,5]thieno[3,2-b]indole-2,10-diyl)bis(methanylylidene))bis(5,6-difluoro-3-oxo-2,3-dihydro-1H-indene-2,1-diylidene))dimalononitrile (Y6) led to a leap in OSC PCE to 15.7 % [32, 33]. Further development of PM6:Y6 OSCs has resulted in PCEs exceeding 17 %, making this combination one of the most striking blends recently [34].

### 1.3.4 Charge Collection

The final step of photocurrent generation in an OSC is the collection of photogenerated carriers. The transport of photogenerated electrons and holes within donor and acceptor phases is governed mainly by hopping transport (Equation (1-1)). In order to collect the photogenerated charges from the active layer, it is sandwiched between several layers and electrodes (**Figure 1.9**). Materials with different WFs are used for the bottom and top electrodes to induce a built-in potential, which helps driving photogenerated electrons and holes to the appropriate electrodes. Initially, researchers used a conventional architecture (**Figure 1.9.a**) in which the bottom transparent electrode (mostly ITO) was used for hole-collection, while the top electrode, made of a low-WF metal (e.g., Al), was used for

electron collection. However, low-WF metals, which easily oxidize in air, compromises the ambient stability of the device (will be discussed in Chapter 2). This problem was later addressed by introducing inverted geometry (**Figure 1.9.b**) with reversed charge polarity-- the top electrode used for hole collection-- enabling the use of a high-WF metal (e.g., Ag) instead of a low-WF one. The inverted architecture benefits from the solution processability of its contact (Ag) and higher device ambient stability (will be discussed in Chapter 2).

In each device architecture, for efficient charge extraction, the WF of the electrodes must match appropriately with the energy level of the organic layer to minimize the energy barrier that respective charge carriers must overcome. However, poor ohmic contacts form between organic materials and electrodes in OSCs due to a high energetic barrier, interfacial dipoles, and high density of interfacial traps [35]. Therefore, to further optimize charge extractions and provide ohmic contacts, interfacial extraction layers are inserted between the organic active layer and the relevant electrodes. Depending on their location in the device, these layers can be classified according to their functionality as (i) hole extraction layers (HEL) and (ii) electron extraction layer (EEL). In literature, the EEL is also named electron transport layer (ETL) or electron selective layer (ESL), and the HEL is hole transport layer (HTL) or hole selective layer (HSL). For the sake of clarity, EEL and HEL are used in this thesis. Common HELs are poly(3,4-ethylenedioxythiophene) polystyrene sulfonate (PEDOT:PSS), molybdenum trioxide ( $\text{MoO}_3$ ), or tungsten trioxide ( $\text{WO}_3$ ), and the most widely used EELs are metal oxides like ZnO or  $\text{TiO}_2$ .

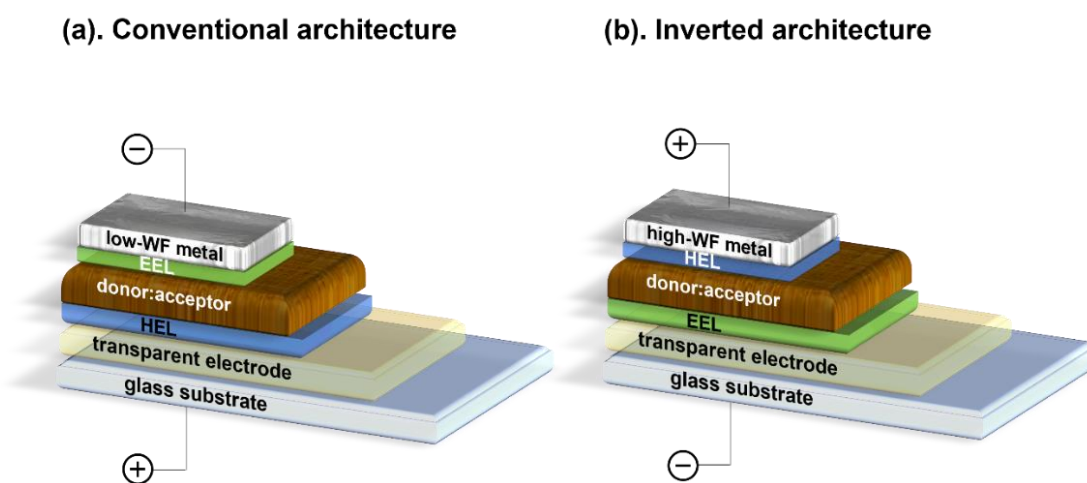


**Figure 1. 9.** BHJ OSCs with (a) a conventional and (b) an inverted architecture.

### 1.3.4.1 The Role of Charge Extraction Layers

The major role of the extraction layers at their corresponding contacts is to provide charge selectivity; (i) they control the energy barrier for respective photogenerated charge extraction (electron for EELs), and (ii) they block the opposite charges (holes for EELs). Aside from the charge selectivity, depending on the device geometry, each of the extraction layers that is inserted underneath the active layer can also (i) affect the morphology of the solution-processed active layer due to introducing new surface topography and surface energy, and (ii) enhance absorption of photons through adjusting the spectral overlap of incident radiation with the bulk thickness [36]. Although the latter is essential, it is not the purpose of this thesis and will not be discussed further. In addition, changes undergone by these extraction layers over time or under operational conditions are also likely to be a key determinant of device lifetime and have been recently one of the key research themes [37]; this will be further explained in Chapter 2.

In BHJ OSCs, and thus in this study, since donor and acceptor phases exist throughout the active layer, holes or electrons can easily reach the opposite electrodes. Therefore, controlling the energy level alignments at the organic/electrode interfaces is critical to prevent energy losses caused by resultant charge recombination at the organic/electrode interface in BHJ OSCs. Hence, EELs and HELs play key roles in the performance of BHJ OSCs.

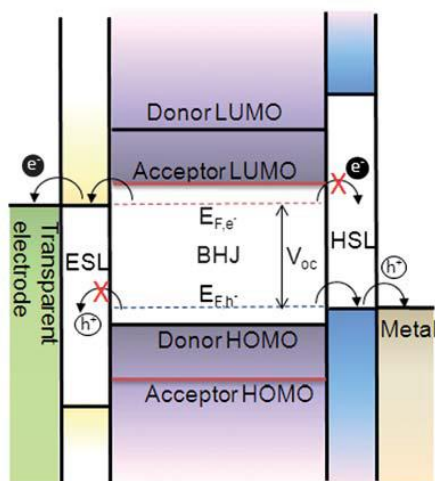


**Figure 1. 10.** Schematic view of the energy level alignment in an inverted OSC with extraction layers providing ohmic contacts and charge selectivity. Reproduced from Ref.[38] with permission from the Royal Society of Chemistry.

**Figure 1.10** is a schematic of an ideal energy level of interlayers and electrodes. Ideally, the VB or HOMO of the HEL should match with the hole quasi-Fermi level ( $E_{F,h}$ ) of the donor, while EEL should have a CB or LUMO close to the electron quasi-Fermi level ( $E_{F,e}$ ) of the acceptor to facilitate electronic equilibrium and minimize barriers for respective charges [38]. This, however, does not account for the known midgap states in the interlayer material, specifically exist in the surface of oxides and polymers. Plus, the impact of interface dipole and consequent local vacuum level shifts, resulting from dipolar or charged molecules at the organic/interlayer interface, is not considered in **Figure 1.10**. Practically, organic/oxide and organic/metal interfaces often exhibit vacuum level shifts up to 0.8 eV, which can affect (negatively or positively) the energy barrier and so the ohmic characteristics of contacts [37]. Recently, intentionally utilizing this dipole effect at both interfaces has been a popular approach for modifying injection/extraction barriers as well as for controlling surface free energy and wettability [37, 39].

#### 1.3.4.2 Electric Dipole Interlayer

An electric dipole consist of two point charges, one with charge  $+q$  and the other with charge  $-q$ , separated by a distance  $\vec{d}$ , shown in **Figure 1.11.a**. The electric dipole moment is a measure of the separation of positive and negative electrical charges within a system, defined as  $\vec{p} = q \vec{d}$ , with the direction of the vector  $\vec{p}$  points from the  $-q$  toward the  $+q$ . An electric dipole forms with any asymmetry in the chemical bond or in the atoms' electronegativity. The microscopic dipole moments are neutralized in most (non-ferroelectric) bulk materials owing to the random orientation (in gas, liquid, or amorphous medium) or lattice symmetry (in crystals). However, the intrinsic asymmetry at interfaces induces the orientation of microscopic dipole moments in its vicinity. When charge transfer, polarization, or rearrangement of the electron cloud occurs across the interface, interfacial dipole moment forms even if the molecules are symmetric.

Understanding the role of interfacial dipoles requires defining the WF first; the minimum energy needed for removing an electron from a material's Fermi level to the local vacuum level ( $E_{vac}$ ) (a few nanometers above the material's surface). Generally, a material's WF depends on electron chemical potential and surface dipole. The former represents the Fermi energy relative to the absolute vacuum level (far away from the surface). The latter (surface dipole) depends on various factors and induces an additional energetic barrier for an electron to leave the solid's surface [40].

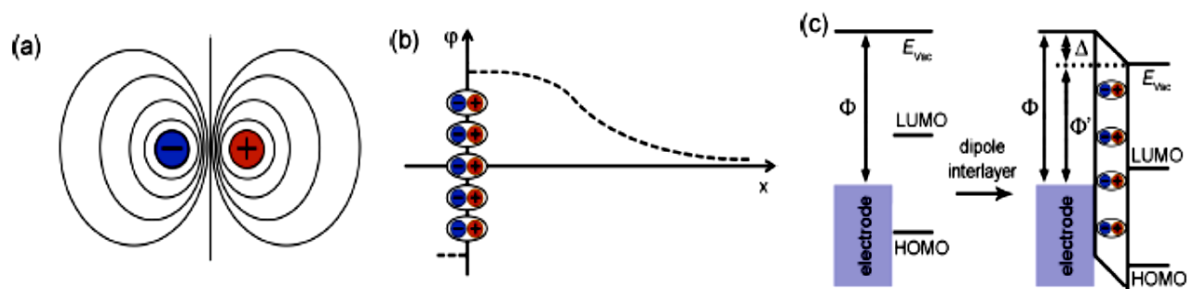


**Figure 1. 11.** (a) Schematic of a single electric dipole with equipotential lines. (b) The potential distribution of an electric dipole layer. (c) An abrupt shift ( $\Delta$ ) in  $E_{vac}$ , induced by an interfacial dipole layer, reducing the apparent work function of the electrode,  $\Phi' = \Phi - \Delta$ . Reproduced with permission from [39]. Copyright 2020, American Chemical Society.

**Figure 1.11** schematically shows the electrostatic characteristics of dipole interfacial layers. When a large number of positive and negative charges are distributed asymmetrically in a thin layer, an electric dipole layer is formed. This thin dipole layer is approximated as a large number of parallel electric dipole moments, causing a potential drop at its vicinity, from the positive side to the negative side:

$$\delta = n\vec{p}/\epsilon_0\epsilon, \quad \text{Equation 1- 2}$$

where  $n$  is the density of the electric dipole,  $\epsilon_0$  is the vacuum permittivity, and  $\epsilon$  is the dielectric constant of the dipole material. This potential cause an abrupt shift in the vacuum energy level at the interface, defined by Equation (1-3):

$$\Delta = ne\vec{p}/\epsilon_0\epsilon, \quad \text{Equation 1- 3}$$

where  $e$  is the elementary electron charge. This shift changes the apparent WF of the electrode and consequently affects charge carrier transport across the interface (**Figure 1.11.c**) [39].

As this thesis focuses on EELs in inverted BHJ OSCs, we narrow down our discussion to the effect of dipole interlayers in EELs. In inverted OSCs, ITO is the commonly used electrode as an electron collection contact; it however has a WF of  $\sim 4.7$  eV, which lies close to the middle of the bandgap of most organic active layer materials (**Figure 1.12.a**) [41] and thus can allow for undesirable hole collection [42]. As shown in **Figure 1.12.b**, ITO allows the extraction of both electrons and holes simultaneously. Therefore, using EEL is critical for inverted OSCs [43-46].

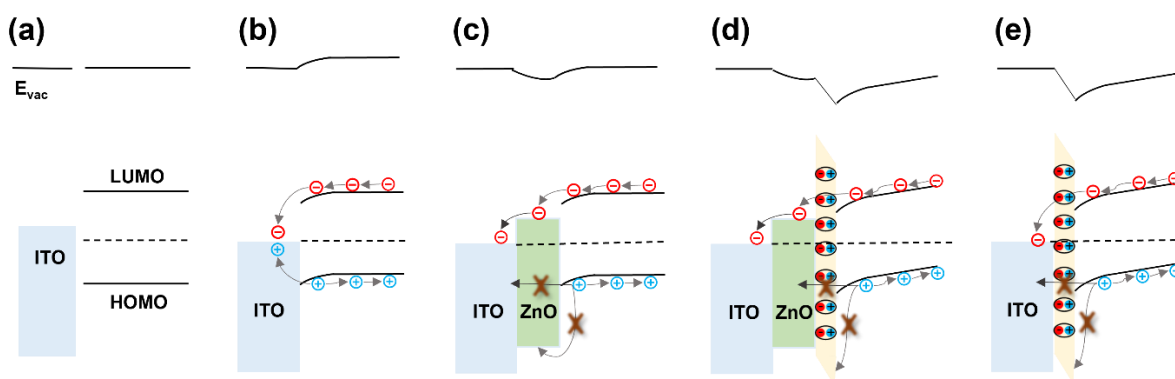


**Figure 1.12.** Effects of interfacial dipole layers on the energy diagram. (a) and (b) are the energy levels of ITO and active layer before and after contact, respectively; (c) ZnO EEL, a representative of an n-type metal oxide with a deep valence band, facilitates electron transport while blocks holes; (d) ZnO/dipole-layer EEL, adding a dipole layer reduces the ZnO apparent WF and enhances the electron selectivity at the bottom contact; (e) ITO/Dipole layer, adding a dipole layer between the ITO and active layer can act as an EEL. Dipoles with positive charge end toward the active layer and negative charge end pointing toward ITO reduce the apparent WF of ITO and facilitate electron transport while blocks hole transports [39].

One approach is to use n-type metal oxides with a deep VB as an EEL. ZnO has been the most commonly used material for that purpose owing to its low toxicity, high electron mobility, and inherent transparency [47]. As schematically depicted in **Figure 1.12.c**, the high electron mobility of ZnO facilitates electron extraction while its deep valence band provides a large energy barrier against holes (often more than 1 eV), increasing contact selectivity. Despite these benefits, OSCs with ZnO face some challenges, which will be elaborated in Chapter 2.

Another approach that has recently been employed to modify the contact electron selectivity is to use a bilayer of metal oxide (e.g., ZnO) with a thin dipole layer on top. For a dipole interlayer to be used in the bottom electron collection contact in inverted OSCs, it has to upshift the Fermi level, i.e., decrease the work function, to facilitate selective electron collection. This energy level shift requires an interfacial dipole with its positive end pointing toward the organic active layer and the negative end pointing toward the ITO (**Figure 1.12.d**). Thus, the bilayer EEL facilitates electron transport due to the high electron mobility of metal oxides while lowering the electron barrier by interfacial dipole moment, providing a higher degree of electron selectivity.

An alternative strategy is employing a thin dipole layer alone as an EEL (**Figure 1.12.e**). Using a thin layer of conjugated polyelectrolyte PFN on ITO, He et al. reported a  $\sim 0.6$  eV downshift in  $E_{vac}$ ; a reduction in ITO WF from 4.7 to 4.1 eV. As a result, the ITO/PFN contact provided a lower barrier for electron transport but a higher barrier for hole transport, improving device performance [48]. Since



then, many polyelectrolyte dipole interlayers have been employed in the contacts of optoelectronic devices [39]. Next, Zhou et al. [49] reported that non-conjugated polyelectrolytes containing amine groups, polyethyleneimine ethoxylated (PEIE), and branched polyethyleneimine (PEI), form an interfacial dipole at the surface of various metals and metal oxides, lowering their WF. This discovery inspired the use of PEIE or PEI interlayer-modified ITO in organic optoelectronic devices. Utilizing PEIE and PEI in the EEL of OSCs showed excellent initial electron selectivity, leading to efficiency improvement.

#### 1.4 Solar Cell Circuit Model and Photovoltaic Characteristics

The electrical and photovoltaic performance of solar cells can be described by their current density ( $J$ ) versus voltage ( $V$ ) characteristics in the dark and under illumination. The illuminated  $J$ - $V$  characteristics are measured under standard test conditions (STC): an incident irradiance of  $1000 \text{ W}\cdot\text{m}^{-2}$  ( $100 \text{ mW}\cdot\text{cm}^{-2}$ ) with an AM1.5 spectrum and a temperature of  $25^\circ\text{C}$ .

A solar cell's performance can be modeled by a simple equivalent circuit, a parallel diode, and a constant current source. However, practically, solar cells are not ideal and have several non-idealities in the device structure and operation. These non-idealities are considered by defining series resistance ( $R_s$ ) and shunt resistance ( $R_{sh}$ ).  $R_s$  originates from resistances throughout the bulk of the active layers, as well as contact resistances between the electrodes and the organic semiconductor, and the resistances of the electrodes themselves, whereas  $R_{sh}$  is a result of leakage current and recombination within the device. The modified equivalent circuit model considering the series resistance and the shunt resistance is illustrated in **Figure 1.13.a**.

The main photovoltaic properties that are used to characterize the performance of solar cells are the short-circuit current density ( $J_{sc}$ ), the open-circuit voltage ( $V_{oc}$ ), the fill factor (FF), the maximum power point ( $P_{max}$ ), and the power conversion efficiency (PCE). These parameters are extracted from the illuminated  $J$ - $V$  characteristic of solar cells, as illustrated in **Figure 1.13.b**.

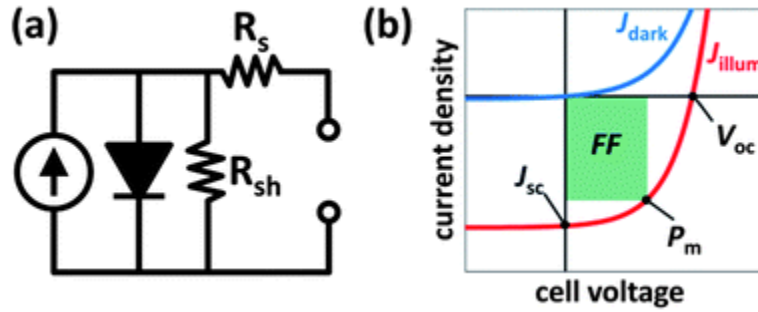


**Figure 1. 13.** (a) A simple equivalent circuit model for a solar cell. (b) Typical current density–voltage ( $J$ – $V$ ) characteristics for a solar cell in the dark and under illumination. Reproduced from Ref.[36], with permission from the Royal Society of Chemistry.

#### 1.4.1 Short-Circuit Current Density

The short-circuit current density is the maximum current density that flows through the external circuit when no external bias is applied and represents the number of photogenerated charge carriers that are successfully collected by the respective electrodes at zero applied voltage.

#### 1.4.2 Open-Circuit Voltage

The open-circuit voltage is the voltage at which no current flows through the external circuit. When a solar cell is at the open-circuit state, the free photogenerated charges will accumulate at their respective electrodes, inducing a potential difference. At the steady-state condition, this potential cancels out the built-in potential. Consequently, carrier generation and recombination balance each other, resulting in a zero net current. The system is now in a quasi-equilibrium state, and the potential difference formed between the two electrodes is the open-circuit voltage, which represents the maximum voltage a solar cell can deliver to an external circuit.

Generally,  $V_{oc}$  is defined by electron and hole quasi-Fermi level splitting under illumination according to Equation (1-4):

$$V_{oc} = \left(\frac{1}{q}\right)(E_{Fn} - E_{Fp}), \quad \text{Equation 1- 4}$$

where  $E_{Fn}$  and  $E_{Fp}$  are the electron and hole quasi-Fermi levels, respectively. In crystalline Si solar cells (with normal doping and under normal sunlight illumination), the electron and hole quasi-Fermi levels are close to the conduction and valence bands, respectively, resulting in a  $V_{oc}$  almost equal to the bandgap. However, in disordered amorphous Si and organic solar cells, accumulation of photogenerated carriers in disorder-induced gap tail states downshifts the electron quasi-Fermi level

and upshifts the hole quasi-Fermi level, resulting in  $V_{oc}$  reduction. The highest  $V_{oc}$  reported so far for solution-processed OSCs is 1.3 V [50].

### 1.4.3 Fill Factor

The fill factor is the ratio of the 'actual' maximum output power to the 'possible' maximum power (where the OSC acts as an ideal diode). Schematically, the FF indicates how "square" the  $J-V$  curve is or how close the cell is to an ideal solar cell and is defined by Equation (1-5):

$$FF = \frac{V_m I_m}{V_{oc} I_{sc}}, \quad \text{Equation 1- 5}$$

where  $V_m$  and  $I_m$  are the voltage and current values at the maximum power point. Even in inorganic solar cells with high PCEs, FF cannot reach 100%. In OSCs, FF is usually in the range of only 50–77% [50, 51].

### 1.4.4 Power Conversion Efficiency

The power conversion efficiency is the ratio between the maximum electrical energy flux ( $P_m = V_m I_m$ ) and the intensity of the incident illumination ( $P_{in}$ ), when the characterization is done under the STC, and expressed by Equation (1-6).

$$PCE = \frac{P_m}{P_{in}} = \frac{FF V_{oc} I_{sc}}{\text{Input Optical Power (W)}} \quad \text{Equation 1- 6}$$

Other important parameters of a solar cell are:

$\eta_{EQE}$ : external quantum efficiency (EQE) – the ratio of the number of collected photogenerated carriers per number of incident photons at a given wavelength, defined by Equation (1-7):

$$EQE = \eta_{EQE} = \frac{hc \cdot I_{sc}(\lambda)}{q \lambda \cdot P(\lambda)}, \quad \text{Equation 1- 7}$$

where  $h$  is Planck's constant,  $c$  is the speed of light,  $I_{sc}(\lambda)$  is the wavelength-dependent short circuit current,  $q$  is an electron charge,  $\lambda$  is the wavelength of the incident light, and  $P(\lambda)$  is the wavelength-dependent light intensity.

$\eta_{IQE}$ : internal quantum efficiency – the number of collected photogenerated carriers per number of absorbed photons by the active layer.  $\eta_{EQE} = (1 - R)\eta_{IQE}$ , where  $R$  is the reflectivity of the substrate-air interface.

## Chapter 2

### Stability of OSCs

#### 2.1 Introduction

Current research and advances in OSC technology have now increased OSC efficiency to 17% [14, 34]. With this efficiency improvement, one main barrier to commercializing organic photovoltaic technology is their limited operational stability [52-54]. Therefore, the scientific community is changing its focus from enhancing OSCs' efficiency to understanding their degradation and optimizing their stability. In OSCs, degradation causes a decrease in PCE over time; this degradation arises from various aging stressors, including atmospheric oxygen and moisture [52], temperature, and solar irradiation [55-57]. Therefore, controlling degradation requires understanding the mechanisms and their effects on device performance as the first step. This chapter will present a literature review of degradation mechanisms in OSCs and strategies to control them and will highlight the gap in the knowledge, concluding with the motivations and objectives of this work.

#### 2.2 Degradation Mechanisms in OSCs

Generally, OSC degradation mechanisms can be grouped into two categories: (i) extrinsic degradation, which occurs when cells are subjected to the ambient oxygen and water, and (ii) intrinsic degradation, which occurs when atmospheric components are excluded. For each category, a variety of strategies have been employed to minimize these effects [58]. In each category, different degradation pathways are involved when cells are in the dark versus under illumination.

##### 2.2.1 Extrinsic Degradation

Extrinsic degradation is also known as “ambient-induced degradation,” as it occurs via reactions between the atmosphere and the device constituents (either in the dark or under illumination). Here, ambient oxygen/water can diffuse into the device through different entrance channels (**Figure 2.1**) and degrade the electrodes, the charge extraction layers, and the active layers [59]. For example, both oxygen and water are prone to react with the cells' low-WF metal electrode (Ca, Al) and form an

electrically insulating metal oxide layer, which impedes charge transport and extraction. Another example is the reaction of water with Al-C bonds at the metal electrode interface, which has been found to degrade PV properties [3]. One extra path of ambient degradation is the easy absorption of ambient water by PEDOT:PSS (widely used HEL) due to its hygroscopic nature, impeding hole extraction [56]. Aside from the HELs, oxygen diffusion into the EELs (such as TiO<sub>2</sub>) forms oxygen defects, acting as electron traps and hindering electron extraction [60].

Organic active layers also degrade in the presence of oxygen and moisture. Atmospheric oxygen can react with organic layers under illumination and cause photobleaching [58]. Photooxidation of active layers degrades device performance via various pathways: 1) changing donors' or acceptors' molecular structures, thereby decreases their absorption efficiency [61]; 2) increasing the energetic disorder in the film [62, 63]; and 3) shifting the energy levels of organic layers which can misalign energy levels between donors and acceptors [64, 65]. In addition to chemical degradation, the permeation of ambient components can induce physical changes in the active layer morphology and thus reduce exciton dissociation rates [60]. The oxygen and water can also dope the active layer and increase hole concentration, reducing  $V_{oc}$  and FF. Additionally, the accumulation of photogenerated carriers in the trap states of active layers changes the energy band slope, reducing  $V_{oc}$  over time [66, 67].

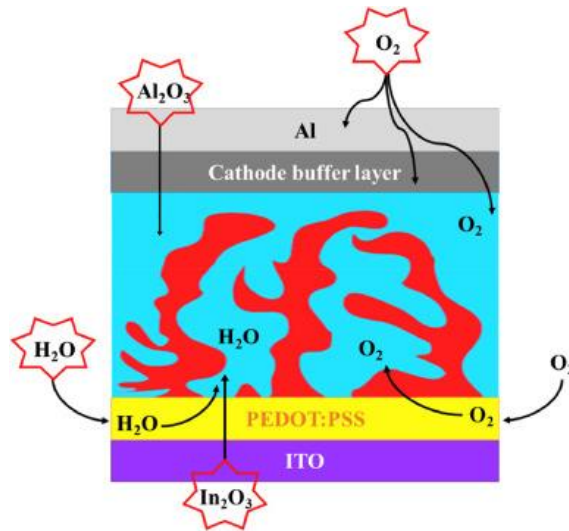


**Figure 2. 1.** The degradation pathways of ambient oxygen/water into OSCs. Reproduced with permission from [68]. Copyright 2020, Elsevier.

Ambient-induced degradation can be effectively controlled via proper device encapsulation [54, 69]. Further improvement has been achieved by replacing the conventional geometry with an inverted configuration in which the top electrode consists of a high WF metal instead of a low WF one, which readily reacts with atmospheric oxygen and water. As a result, extrinsic degradation related to the top electrode can be significantly reduced [3, 70, 71]. Replacement of PEDOT:PSS with metal oxides such as MoO<sub>x</sub>, nickel oxide (NiO<sub>x</sub>), and tungsten oxide (WO<sub>x</sub>) has provided more stable alternatives [60].

In addition, reports on the photo-oxidation of organic materials show a direct correlation between crystallinity and photo-oxidation stability [66, 72, 73]. For instance, Chasse *et al.* [74] demonstrated that regiorandom (RRa) P3HT (fully amorphous) shows a five times higher photobleach rate compared to regioregular (more crystalline) P3HT. The fact that these two materials are identical in terms of their chemical structures and differ only in the orientations of their side chains and consequently in their molecular packing illustrates the strong impact of molecular packing on photostability. Further research by Durrant *et al.* [73] investigating several amorphous and crystalline polymers has confirmed that the crystalline polymers exhibit a much lower photobleaching rate. The role of film morphology and molecular packing density on the photo-oxidative stability of OSCs was also studied by Mateker *et al.* [72]. Based on their study, since a dense-packed film can suppress the movement of radical species, increasing the packing density of the film enhances OSC stability. They also illustrated a significant decrease in the photobleaching rate as a result of increasing polymer backbone planarity. Based on these observations, increasing polymer crystallinity, molecular packing, and backbone planarity are potential approaches to diminishing photo-oxidative degradation. Thus, tuning polymer crystallinity and using antioxidizing stabilizers have been used as approaches to enhance ambient stability [60, 75].

In the case of NFA-based OSCs, it is found that the chemical structure of NFAs contributes to device photostability in air. Guo *et al.* [76] systematically investigated the correlation between the NFA material structure and photobleaching rate and suggested some design strategies for NFAs to enhance their OSCs photo-oxidation stability. They also suggested using an antioxidizing agent, nickel chelate S6, as an additive into the BHJ layer as a cost-effective route to increase photostability. In addition, recent studies [77] [78] [79] focused on using ternary BHJ blends instead of the standard donor-acceptor binary counterparts for simultaneously improving device efficiency and stability. The ternary active layers offer higher photostability owing to a crystalline and molecular packing structure and thus interlocked morphology of the ternary films.

## 2.2.2 Intrinsic Degradation

Degradation studies have recently focused on intrinsic mechanisms, which have proven to be more challenging. Even in the absence of atmospheric stressors, OSCs show intrinsic PCE deterioration, which can occur in both dark and illuminated conditions due to a variety of reasons. Dark intrinsic degradation can occur either only over time at room temperature or under operational temperature. The following section reviews these degradation mechanisms in OSCs and several approaches to help mitigate them.

### 2.2.2.1 Intrinsic Degradation in the Dark

One origin of intrinsic degradation is the morphological instability over time that arises from the movement of organic molecules. Particularly, BHJ OSCs, whose active layer consists of an interpenetrating network of donor and acceptor phases, suffer from morphological instability due to the metastable characteristics of their blends. For instance, devices with poly[(5,6-dihydro-5-octyl-4,6-dioxo-4H-thieno[3,4-c]pyrrole-1,3-diyl)[4,8-bis[(2-ethylhexyl)oxy]benzo[1,2-b:4,5-b']dithiophene-2,6-diyl] (PBDTTPD):PCBM and MDMO-PPV:PCBM BHJs, exhibit 10-20 % PCE degradation within a day, even when stored at room temperature in an inert atmosphere [58]. Moreover, high boiling point solvent additives, usually used in the active layer to improve device efficiency, can exacerbate morphological instability, and hence, increase intrinsic degradation of OSCs over time [54, 58]. In addition to the BHJ layer, the electrodes (ITO and Al) and interfacial layers may also move within the device at room temperature and degrade device performance over time by changing the energy levels of interfacial layers or acting as charge traps at the interface or inside the active layer [54].

Aside from the degradation at room temperature, OSCs can degrade by thermal stressors arising from prolonged solar illumination. Generally, the working temperature of OSCs is much lower than the chemical decomposition temperature of their organic layers; still, many OSCs suffer from thermal degradation linked with the physical degradation caused by heat. The temperature at which the thermal-induced degradation starts is above the lowest glass transition temperature of constituent organic materials [58]. At temperatures above  $T_g$ , molecules can start to move around in the films, leading to efficiency loss. The rearrangement under thermal stress mainly occurs in the BHJ layers and is attributable to their metastable morphology. Heating BHJ layers above  $T_g$  for a long time causes macroscopic phase separation, which reduces the exciton dissociation rate, causing a significant  $J_{sc}$  loss. The morphological changes in active layers can also change their adhesion to the electron extraction layers, limiting electron extraction [60]. Other than the BHJ rearrangement, thermal degradation can

occur through the diffusion of metal atoms from the electrodes into the next organic layer, causing efficiency losses [80, 81]. Moreover, the thermal-induced crystallization of organic small molecules used as interfacial layers can also degrade device performance. Some charge extraction layers like PEDOT:PSS exhibit a heat-induced reduction in their electrical conductivity [60].

Strategies like employing thermally cleavable side chains, controlling the polymer regioregularity, and using cross-linkable side chains are found to increase thermal stability [54]. However, the use of cross-linkable polymers or fullerenes degrades initial device performance [58]. Currently, the primary approach to preventing dark degradation at the operational temperature of solar cells is to use materials with a high  $T_g$  (e.g., PCDTBT) [53, 105].

#### 2.2.2.2 Intrinsic Degradation Under Illumination

Since solar cells inevitably work under light exposure, light-induced degradation is another intrinsic source of failure. Many encapsulated OSCs show a significant degradation under illumination in the first several hundred hours while they are stable in the dark [82, 83]. It has been demonstrated that the main part of the light-induced degradation depends on the availability of UV photons, which are high-energy components of the sunlight spectrum [69, 84-86]. Although photo-oxidation has been investigated extensively in a vast body of work, studies on the photodegradation of OSCs in the absence of atmospheric oxygen are still limited. Shaheen et al. [87] and Gevorgyan et al. [88] conducted the first experiments on OSC stability in an inert atmosphere. Illumination can affect active layers, interfacial layers, and electrodes.

In small-molecule OSCs, C60 fullerenes are shown to form oligomers upon irradiation in the absence of oxygen, causing a significant  $J_{sc}$  loss [89, 90]. Similarly, in polymer:fullerene OSCs, the photoinduced PCBM dimerization causes inefficient exciton dissociation and concomitant  $J_{sc}$  degradation [91]. Contrary to most polymer:PCBM systems, optimized P3HT:PC60BM devices do not exhibit significant dimerization-related  $J_{sc}$  losses [82]. Studying different polymer:PC60BM OSCs (**Figure 2.2**), Heumueller et al. [92] reported that smaller  $J_{sc}$  photodegradation is observed when: P3HT:PCBM is cast from dichlorobenzene instead of chloroform, PC60BM is replaced with PC70BM, and KP115:PC60BM is operated at a short-circuit instead of an open-circuit condition. Therefore, factors like the morphology and crystallinity of BHJ, processing solvents, and electrical bias during illumination significantly affect fullerene dimerization. Another type of photodegradation of fullerene-



based OSCs, intrinsic to UV photons, is triplet-induced nano-morphology disorder. Investigating the UV-induced degradation dynamics when a solar cell is encapsulated, Quan et al. [84] observed a significant irreversible change in the nano-morphology of the fullerene acceptor. This nano-morphology disorder was attributed to the release of the electrostatic potential energy accumulated by the formation of PCBM triplet anions under UV irradiation. They suppressed this UV-induced degradation by increasing the crystallinity of the acceptor phase through thermal annealing.

Aside from the fullerene degradation, polymer photodegradation is another root cause of limited intrinsic photostability. Photoinduced  $V_{oc}$  loss is observed in a variety of BHJ solar cells [93]. McGehee et al. [94] ascribed the  $V_{oc}$  degradation in the PCDTBT system to the formation of light-induced traps and a consequent increase in the energetic disorder of the polymer.

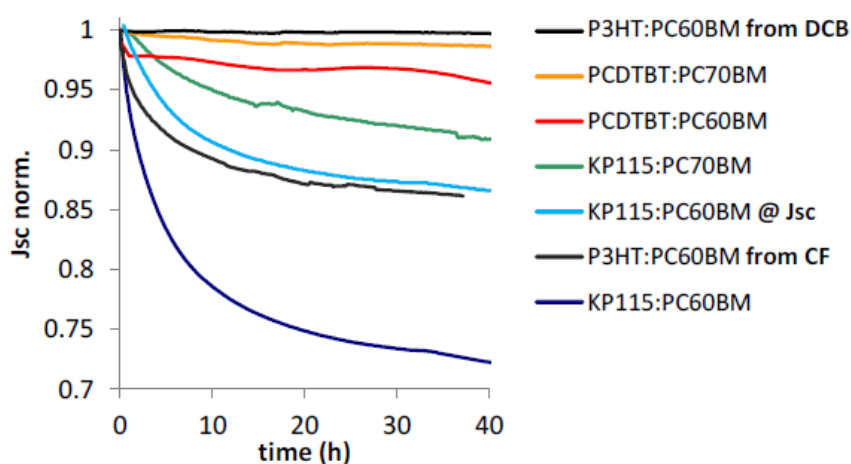


**Figure 2. 2.** Normalized  $J_{sc}$  versus illumination time in an inert atmosphere for various polymer-fullerene OSCs. Reproduced from Ref.[92] with permission from the Royal Society of Chemistry.

In addition to the active layer, interfacial layers and electrodes play a determinant role in the intrinsic photostability of OSCs. Aziz et al. have demonstrated the critical role of EELs in the photostability behavior of inverted OSCs [44, 45, 95]. In inverted devices, ZnO, the most commonly used EEL, is susceptible to changes by illumination [69, 96]. Manor et al. reported a significant  $V_{oc}$  loss, and a decrease in shunt resistance in ZnO-based OSCs under concentrated simulated sunlight [96]. While they attributed the decrease in  $R_{sh}$  to the photoinduced formation of shunting channels at the ZnO/organic interface, the origin of  $V_{oc}$  loss was not addressed adequately. Kam et al. investigated the

degradation of ZnO-based inverted OSCs under operational conditions, with and without filtering the UV component. They demonstrated that the occurrence of significant  $V_{oc}$  loss depends on the availability of UV light [69]. Aurélien, et al. [86] reported the formation of vacancies on the ZnO layer and found chemical products at the ZnO/active-layer interface after UV irradiation, increasing charge carrier density and thereby decreasing  $V_{oc}$ . Other than the EEL, ITO--the most widely used bottom electrode--shows WF alteration under UV exposure, significantly affecting performance and photostability [97].

Recently, the scientific community has started to replace the fullerene acceptors with non-fullerene ones as one potential approach toward enhancing organic solar cell efficiency [98]. Despite several photostability investigations for fullerene-based OSCs, studies on the photodegradation of NFA-based OSCs are still limited. Reports to date show that the photostability of NFA systems is strongly material-dependent. Unlike the fullerene-based BHJ OSCs, which exhibit dimerization-induced  $J_{sc}$  loss and disorder-induced  $V_{oc}$  loss upon illumination, FF degradation seems dominant in NFA-based systems [98]. Park et al. [99] compared fullerene-based ([70]PCBM) and non-fullerene-based (ITIC) cells to explore the role of the acceptor on the photostability of their respective OSCs with poly[2,6-(4,8-bis(5-(2-ethylhexyl)thiophen-2-yl)benzo[1,2-b:4,5-b0]dithiophene)-co-(1,3-di(5 thiophene-2-yl)-5,7-bis(2-ethylhexyl)-benzo[1,2-c:4,5 c0]dithiophene-4,8- dione)] (PBDB-T) and PTB7-Th polymers. Compared to the PC70BM-based OSCs, ITIC-based cells exhibit higher initial efficiency when blended with PBDBT and lower efficiency when blended with PTB7-Th. Interestingly, the ITIC-based devices were less photostable, mostly due to a significant FF loss irrespective of the initial performance. Morphology change after illumination was considered the primary origin for the severe burn-in degradation of ITIC-based devices. Investigating the degradation mechanisms indicates that morphological degradation is strongly linked with the miscibility between the donor and non-fullerene acceptor. A study by Xiao et al. [100] elucidates low stability of OSCs with ITIC or IDIC acceptors when mixed with poly[4,8-bis(5-(2-ethylhexyl)thiophen-2-yl)benzo[1,2-b:4,5-b']dithiophene-co-3-fluorothieno[3,4-b]thiophene-2-carboxylate] PCE10 donor as a result of their poor miscibility with PCE10. Moreover, an increase in trap states, originating from the photoinduced breaking of conjugation of NFA molecules, is suggested to be an origin of  $J_{sc}$  and FF losses in the NFA OSCs upon irradiation in an inert atmosphere [101].

In addition to the light-induced molecular deterioration, interfacial degradation has been recently introduced as a source of low photostability of NFA OSCs. The photocatalytic effect of the ZnO films on NFAs is found to be a dominant photodegradation process in many NFA OSCs. UV illumination

can excite electrons from the VB to the CB while leaving holes in the VB of ZnO. These electrons and holes are reductive and oxidative, which can attack carbonyl bonds. As a result, the photocatalytic effect of ZnO can induce the decomposition of organic compounds [102]. The photocatalytic effect of ZnO on IT-4F (ITIC-2F) acceptor is verified by the disappearance of bands in the region of 550-800 nm and the appearance of new bands in the region of 400-500 nm in the absorption spectra of ZnO/IT-4F sample (**Figure 2.3**). Generally, compared to the fullerene-acceptor-based OSCs, their NFA-based counterparts were found to be more sensitive to the surface ligands of ZnO. In a work by Park et al.[99], the inverted PBDB-T:ITIC OSCs with a ZnO EEL exhibit more than 30% PCE loss within the first 50 h of irradiation. They found that the vinyl group of ITIC reacts with the hydroxyl radicals on the ZnO surface under UV irradiation, leading to ITIC dimerization. This photocatalytic reaction can cause charge accumulation and recombination at the ZnO interface, resulting in device photodegradation.

Like extrinsic photo-oxidation stability, intrinsic photostability is found to increase with increasing active-layer crystallinity. Annealing the PCBM films into a crystalline morphology eliminates the photodimerization reactions and thus  $J_{sc}$  losses. Mitigating the dimerization can also be achieved using C70, PC71BM, or higher adduct fullerenes [58]. McGehee et al. [94] compared the crystalline polymers (regioregular)-P3HT and KP115 and the amorphous polymers PCDTBT and RRA-P3HT and showed that even though light-induced traps are observed in both amorphous and crystalline materials, the  $V_{oc}$  is not reduced in crystalline-based OSCs. They ascribed the higher stability of more-crystalline morphologies to one of the following effects: the higher robustness of more-ordered films to any chemical changes or the lower sensitivity of more-ordered films to any photoinduced defect states as a result of initially having less energetic disorder than amorphous films.

In the NFA-based OSCs, one way to achieve a more photostable active-layer morphology is increasing the miscibility of the donor and acceptor. The good miscibility of a PCE10 donor and an EH-IDT acceptor has been shown to enhance photostability, with a  $T_{80}$  exceeding 2100 h [100]. In addition to miscibility, Du et al. [101] found that subtle end-group and side-chain modifications of NFAs significantly influence OSC photostability. They studied the photostability of OSCs based on ITIC and its derivatives, blended with PBDB-T donor. Compared to the reference PCBM-based device, cells with ITIC, ITIC-M, and ITIC-DM show lower photostability, whereas devices with ITIC-2F and ITIC-Th exhibit a prominent extrapolated  $T_{80}$  lifetime of up to 11,000 and 9,500 h, respectively. They suggested that fluorination of the end-group could stabilize the NFA molecule against

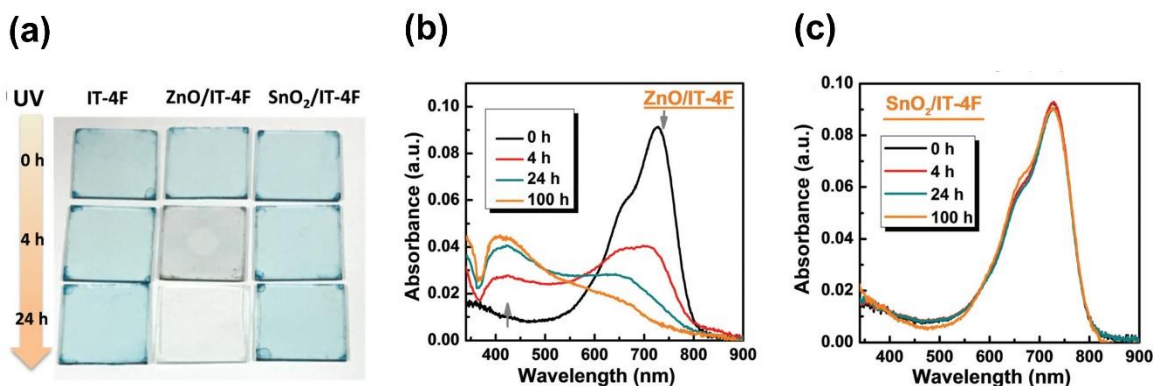


**Figure 2. 3.** (a) Images of IT-4F thin films on glass, glass/ZnO, and glass/SnO<sub>2</sub> substrates under continuous UV illumination (365 nm, 5 mW.cm<sup>-2</sup>). The UV-vis absorption spectra of (b) ZnO/IT-4F and (c) SnO<sub>2</sub>/IT-4F films upon AM1.5 illumination in a N<sub>2</sub>-filled atmosphere. Reproduced with minor changes from Ref.[102] with permission from the Royal Society of Chemistry.

photodegradation, whereas adding methyl groups might induce an opposite impact. By contrast, Doumon et al. [103] showed higher OSC stability with methylated ITIC than fluorinated counterparts, but only in the conventional device structure, not in the inverted one. This observation points to the effects of OSC architecture and interfaces on device photostability.

Beyond the active layer modification, interfacial engineering strategies have been recently employed to control photodegradation. In fullerene-based OSCs, some approaches have been proposed to overcome the UV-induced degradation of ZnO EELs, such as applying UV treatments to the ZnO layer before active layer deposition [104], thermally depositing a thin layer of Al on ZnO as a bilayer EEL [69], or doping the ZnO layer with hydrogen inside a high-temperature and vacuumed furnace [105]. These methods, however, increase the manufacturing complexity and cost. In addition, modifying ZnO with fullerene-based materials [106] leads to significant photostability benefits, but the need for halogenated solvents reduce the viability of these alternatives [107]. Therefore, there is still a need to develop easily processable and green EELs that are resistant to prolonged irradiation [108].

In addition, some ZnO treatments have been utilized to improve the photostability of NFA OSCs. Liu et al. [109] modified the ZnO surface with an organic conjugated small-molecule layer, which significantly improved the overall performance and photostability of the NFA OSCs. Later, using a C60 self-assembled monolayer as a ZnO surface modifier in the PTB7-Th: 2,2'-((2Z,2'Z)-(((4,4,9,9-tetrakis(4-hexylphenyl)-4,9-dihydro-sindaceno1,2-b:5,6-b'dithiophene-2,7-diyl)bis(4-((2-ethylhexyl)oxy)thiophene-5,2-diyl)bis(methanylylidene))bis(5,6-difluoro-3-oxo-2,3-dihydro-1H-

indene-2,1-diylidene))dimalononitrile (IEICO-4F) OSCs, Xu et al. [41] reported a  $T_{80}$  lifetime of over 20 years. Jiang et al. [102] significantly enhanced the photostability of OSCs by replacing ZnO EELs with SnO<sub>2</sub> EELs. They attributed this stability enhancement to eliminating the photocatalytic effect when SnO<sub>2</sub> is underneath the NFAs, as indicated by the UV-vis absorption shown in **Figure 2.3.c**. Recently, Han et al. [32] investigated the effect of ZnO surface PH conditions on the performance and stability of the NFA OSCs. They attributed inferior stability of OSCs with ZnO to the existence of the enormous surface hydroxyl groups, which cause interface recombination and accelerate the photocatalytic process of the acceptor molecules, degrading the NFA at the ZnO/active layer interface (illustrated in **Figure 2.4**). Treating ZnO films with different acids and bases, they found that a ZnO surface acid treatment removes the ZnO surficial hydroxyl groups and consequently enhances device stability and performance, with a significant lifetime improvement ( $T_{80} \geq 4000$  h) compared with pristine ZnO-based OSCs ( $T_{80} < 10$  h) for the PM6:Y6 devices.

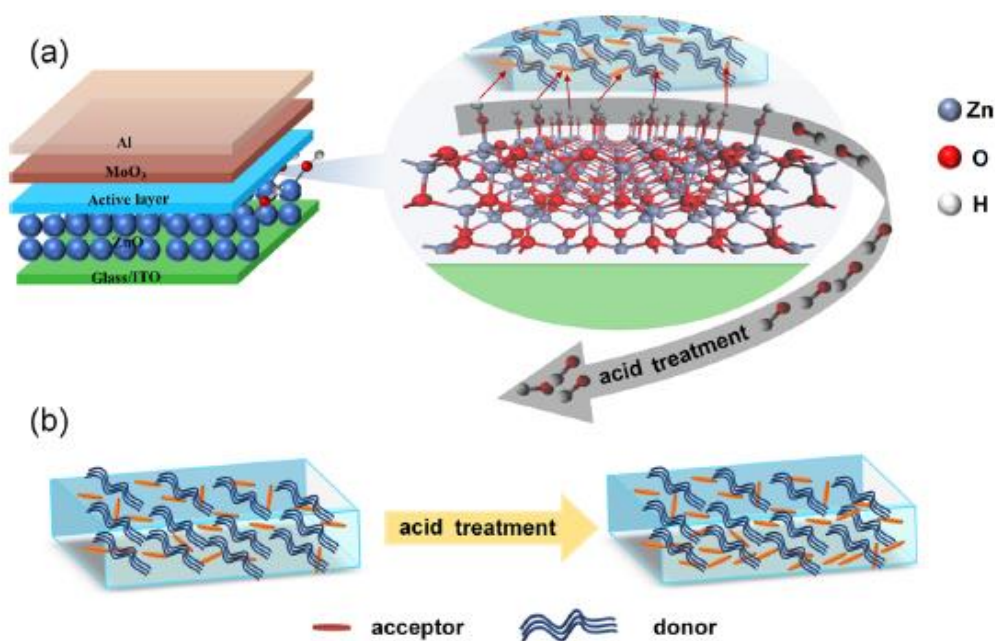


**Figure 2. 4.** Schematic diagram of the mechanism of improved performance and stability with acid-treated ZnO films: (a) removing surface hydroxyl groups on the ZnO surface and (b) regulation of vertical separation in the heterojunction films. Reproduced with permission from [32]. Copyright 2021, American Chemical Society.

## 2.3 Summary of Outstanding Issues

Recently, photodegradation in the absence of post-processed oxygen has gained particular attention, as better encapsulation techniques, inverted device geometry, and thermally robust polymers have been introduced. Many encapsulated OSCs show a significant degradation under illumination in the first several hundred hours even though they may be adequately stable in the dark [82, 83]. As mentioned earlier, the central part of the light-induced degradation depends on the availability of the high-energy UV photons of the sunlight spectrum [69, 84-86]. Thus, exposing OSCs to UV irradiation can simulate vital device degradation in a real-life operation. In addition to the synthesis of novel organic materials, recent interfacial engineering strategies have introduced a new avenue toward photostability enhancement, although more in-depth studies are still needed.

Susceptibility of ZnO, the most common EEL, to UV irradiation has been found to induce photodegradation in inverted OSCs [69, 105, 110]. The degradation is caused by the photoinduced-formation of shunting channels at the ZnO/organic interface. However, the exact mechanism is still unclear; particularly, whether the ZnO susceptibility is due to UV-induced changes in WF or in morphology. It is thus imperative to understand the mechanism and its origins. Additionally, knowing from the literature that ITO shows WF alteration under UV stress [97], the question of whether, in addition to the ZnO/active-layer interface, the ITO/ZnO interface contributes to contact photodegradation arises. Furthermore, the effect of this contact photodegradation on the selectivity of the electron collection contact, the charge recombination mechanisms of the device, and device photostability need to be systematically investigated.

In addition, several reports have shown that adding a new material to ZnO EELs, either in a bilayer or a mixture configuration, can decrease UV-induced degradation of ZnO and enhance photostability [41, 86, 109]; hence investigating the origins of photostability enhancement by modifying ZnO EEL becomes compelling. To do so, the possible influence of ZnO modification on the WF and selectivity of the contact and the resultant impact on charge recombination mechanisms within OSCs (upon UV irradiation) can be the focus of a work.

Aside from ZnO modification, replacing ZnO with fullerene-based materials [106] led to significant photostability benefits, but their use of halogenated solvents [107] brought a need for green-processable and photostable EELs [108]. In this context, using nontoxic materials with large dipole moments for EELs can provide a feasible alternative [39, 47, 97, 111, 112]. According to the "like-dissolves-like" rule-of-thumb, large dipoles make EELs highly soluble in polar green solvents such as water and

alcohol [113]. In addition, as elucidated in Chapter 1, dipole interlayers shift the vacuum Fermi level [114, 115], which provides carrier-selective contacts [116]. Nevertheless, the stability of this contact selectivity upon irradiation and how it affects OSCs' photostability is still a matter of investigation.

## 2.4 Thesis Objectives

This research aims to investigate the influence of the EELs on the photostability of inverted OSCs with the goal of further understanding the mechanisms behind intrinsic photodegradation under UV irradiation and thus improving device photostability. To this end, the following research objectives will be addressed:

- 1) Investigate the effect of modifying the ZnO EEL with amine-containing materials on the intrinsic photostability of inverted OSCs.
  - (a) Examine and compare the effect of introducing PEI to the ZnO EEL as a mixture (ZnO:PEI) or a bilayer (ZnO/PEI). Special consideration will be given to investigating:
    - (i) the impact of UV irradiation on the electron collection efficiency of the ITO/ZnO contact and the origins of contact photodegradation (WF alteration and/or morphological changes).
    - (ii) the role of ITO/EEL *vs.* EEL/active-layer interfaces on contact photodegradation.
    - (iii) any UV-induced changes in the WF, morphology, electrical conductivity, surface potential, and surface chemistry of the contacts of interest: ITO *vs.* ITO/ZnO-only *vs.* ITO/ZnO-modified by PEI.
  - (b) Examine the effect of PDIN-H as a ZnO contact interfacial layer. Special consideration will be given to investigating:
    - (i) the impact of EEL/BHJ shunting on the selectivity of the electron collection contact.
    - (ii) the role of EEL photodegradation on the charge recombination mechanisms of OSCs.

- (iii) the role of PDIN-H interfacial layer on contact selectivity and recombination mechanisms upon UV irradiation.
  - (iv) the role of PDIN-H on the surface characteristics of ZnO.
- 2) Investigate the effect of replacing ZnO EELs with DM-EELs (PEI, Histidine, and Sarcosine) on the intrinsic photostability of inverted OSCs. Special consideration will be given to investigating:
- (i) the role of eliminating ZnO on the stability of electron collection contact.
  - (ii) the impact of introducing large dipoles at EEL interfaces on maintaining electron selectivity upon UV irradiation.
  - (iii) the impact of large dipole moments on charge recombination mechanisms in fullerene-based and NFA-based OSCs.
  - (iv) the impact of EELs' surface defects and charge trapping on contact photostability.



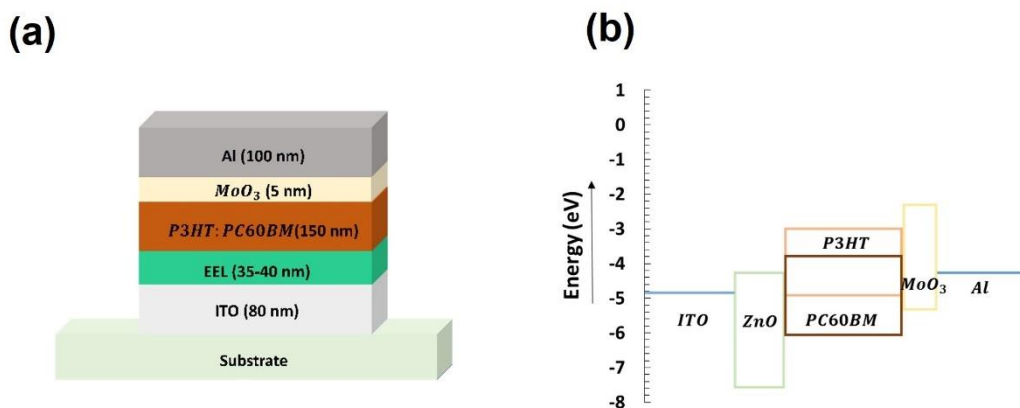
## Chapter 3

### Experimental Procedures

#### 3.1 Introduction

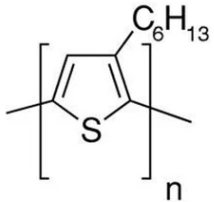
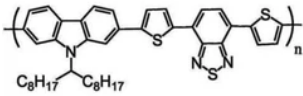
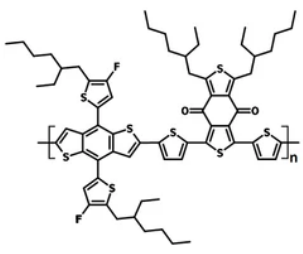
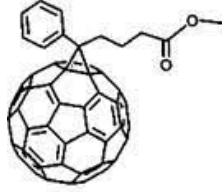
In this work, the intrinsic stability of OSCs is investigated experimentally, with the main focus on photostability. For this purpose, the inverted architecture of ITO/EEL/BHJ/MoO<sub>3</sub>/Al is used with different materials as EELs. ITO, MoO<sub>3</sub>, and Al serve as the bottom electrode, HEL, and the top electrode in these devices, respectively, unless stated otherwise. **Figure 3.1** depicts the main device structure used as a control in this work with its energy level diagram.

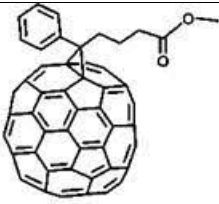
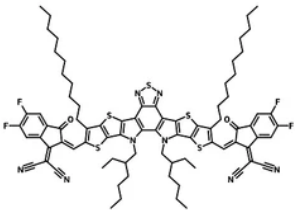
The ubiquitous P3HT:PC60BM is used as a preliminary BHJ active layer. As discussed in Chapter 2, optimized P3HT:PC60BM devices do not exhibit significant dimerization-related  $J_{sc}$  losses, enabling us to direct the main focus on interfacial photodegradation. In addition, to make this thesis widely applicable to OSC research, some of these studies are performed on other promising donors:acceptor materials as well: PCDTBT as a famous amorphous polymer, blended with a more stable fullerene acceptor, PC70BM; and PM6:Y6 as a representative of a non-fullerene high-efficiency BHJ system that has recently attracted significant attention and popularity [34]. Table 3.1 provides the chemical name, molecular structure, and HOMO and LUMO energy levels of the organic donors and acceptors used in active layers in this thesis.



**Figure 3. 1.** (a) OSC structure used in this study, and (b) energy level diagram of the control device in this thesis with each layer's value derived from literature [117].

**Table 3. 1.** The chemical name, molecular structure, and HOMO and LUMO energy levels of the organic donors and acceptors used in active layers in this thesis.

Chemical Name	Molecular Structure	HOMO (eV)	LUMO (eV)
<b>Donor</b>			
Regioregular Poly(3-hexylthiophene-2,5-diyl) (P3HT)		-5.2 [118]	-3.2 [118]
Poly[N-9'-heptadecanyl-2,7-carbazole-alt-5,5-(4',7'-di-2-thienyl-2',1',3'-benzothiadiazole)], Poly[[9-(1-octylonyl)-9H-carbazole-2,7-diyl]-2,5-thiophenediyl-2,1,3-benzothiadiazole-4,7-diyl-2,5-thiophenediyl]		-5.5 [118]	-3.6 [118]
Poly[[4,8-bis[5-(2-ethylhexyl)-4-fluoro-2-thienyl]benzo[1,2-b:4,5-b']dithiophene-2,6-diyl]-2,5-thiophenediyl[5,7-bis(2-ethylhexyl)-4,8-dioxo-4H,8H-benzo[1,2-c:4,5-c']dithiophene-1,3-diyl]-2,5-thiophenediyl]		-5.45 [119]	-3.65 [119]
<b>Acceptor</b>			
[6,6]-Phenyl-C61-butyric acid methyl ester (PC60BM)		-6.1 [120]	-3.7 [120]

<p>3'H-Cyclopropa[8,25] [5,6]fullerene-C70-D5h(6)-3'butanoic acid, 3'Phenyl-3'H-cyclopropa[8,25] [5,6]fullerene-C70-D5h(6)-3'butanoic acid, methyl ester</p> <p><b>(PC70BM)</b></p>		<p>-6.1 [121]</p>	<p>-4.3 [121]</p>
<p>2,2'-((2Z,2'Z)-((12,13-bis(2-ethylhexyl)-3,9-diundecyl-12,13-dihydro-[1,2,5]thiadiazolo[3,4-e]thieno[2'',3'':4',5']thieno[2',3':4,5]pyrrolo[3,2-g]thieno[2',3':4,5]thieno[3,2-b]indole-2,10-diyl)bis(methanylylidene))bis(5,6-difluoro-3-oxo-2,3-dihydro-1H-indene-2,1-diylidene))dimalononitrile</p> <p><b>(Y6)</b></p>		<p>-5.65 [33]</p>	<p>-4.1 [33]</p>

As mentioned in Chapter 2, ZnO is the most widely used EEL in inverted OSCs and will be used as a reference EEL in this thesis. The ZnO film is prepared by the sol-gel method using zinc acetate as a precursor, ethanol as a solvent, and ethanolamine as a stabilizing agent. As a wide bandgap polymer with a large dipole moment, PEI is introduced into the ZnO EEL (as a mixture or a bilayer) and also used as a neat EEL alone. In addition, an N-annulated perylene diimide derivative, PDIN-H, is used as a ZnO surface modifier. Moreover, Histidine and Sarcosine are used as small molecules with large dipole moments. The molecular structures of organic EELs are shown in **Figure 3.2**.

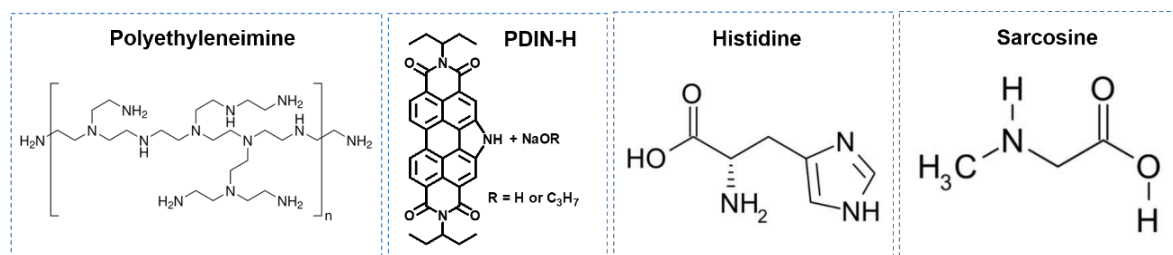


**Figure 3. 2.** The molecular structures of organic EELs used in this thesis.

### 3.2 Device Geometry

The substrate geometry used in this project is 80-nm-thick ITO patterned glass substrates (Kintec) with a sheet resistance of  $15 \Omega \text{ sq}^{-1}$  (shown in **Figure 3.3**), including 14 devices with each cell has a surface area of  $0.04 \text{ cm}^2$  determined by the intersection area of the Al and ITO electrodes. Since devices can be repeatedly tested by contacting only ITO pads on the sides of the substrates, metal scratching will be avoided.

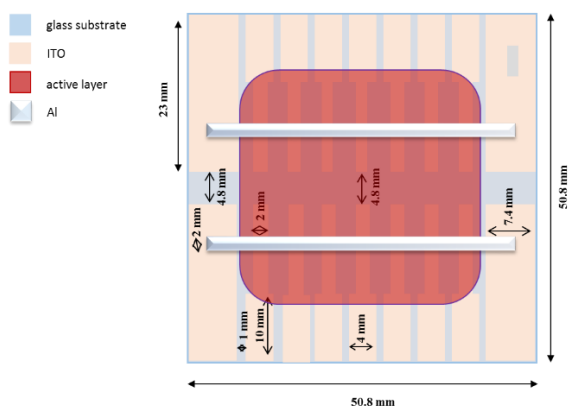


**Figure 3. 3.** Schematic of the device geometry used in this thesis.

### 3.3 Material Preparation and Device Fabrication

ZnO solution is prepared by adding 197 mg zinc acetate (Millipore-Sigma) to 6 mL ethanol and 54  $\mu\text{L}$  ethanolamine (Millipore-Sigma) and mixing at 600 RPM for 40 min at 45  $^{\circ}\text{C}$ . PEI (Millipore-Sigma) is diluted in 1-propanol to reach a 1 mg/ml solution, and for the case of ZnO:PEI mixture, PEI solution is mixed with 32 mg/ml ZnO solution to prepare ZnO:PEI mixtures of various PEI concentrations (0.01, 0.02, 0.03 or 0.04 %wt PEI). For PDIN-H preparation, first, 10 mg of NaOH (Millipore-Sigma) is dissolved in 1 mL ethanol (or 1-Propanol) and is stirred at 400 rpm for 30 min. After sonication, 162  $\mu\text{L}$  of the dilute sample and 2 mL of ethanol are added to 10 mg of PDIN-H [122], followed by stirring at 400 rpm for 30 min. This step yields a complete dissolution of PDIN-H and a color change from orange/red to purple. In this process, the NaOH deprotonates the PDIN-H and forms an alcohol soluble ionic dye, PDIN- $\text{Na}^+$ . Later, upon spin coating the solution, a transition from solution to film shifts back to the PDIN-H, giving the distinct neutral PDI red color. For small-molecule EELs with large

dipole moments, 10 mg of Histidine (Millipore-Sigma) is dissolved in 10 mL of ethanol: DI-water (1:1) mixture and is stirred at 400 rpm for 1 hour. Sarcosine processing is similar to that of Histidine, apart from being dissolved in a 1-Propanol: DI-water (1:1) mixture. All the above steps for all EEL preparation are done in air.

P3HT from Millipore-Sigma and PC60BM from 1-material Company are diluted in dichlorobenzene (Millipore-Sigma) in a 1:1 ratio to obtain a 45 mg/mL concentration and then stirred at 100 °C and 650 rpm overnight. PCDTBT:PC70BM (Millipore-Sigma) is dissolved in dichlorobenzene with a ratio of 1:4 and then stirred at 80 °C and 650 rpm overnight to obtain a 25 mg/mL concentration. A 15 mg/ml (1:1.2) PM6:Y6 (1-material Company) solution is prepared in Chloroform (Millipore-Sigma) through stirring at 650 rpm and 50 °C overnight. All the above steps for all active layer preparation are done inside a glovebox.

For OSC fabrication, the substrates are first cleaned via sequential ultrasonic treatments using Micro 90, deionized water, acetone, and isopropanol solutions, followed by drying on a hotplate for 5 min and then treated with  $O_2$  plasma for 5 min. Then, for coating the EELs, ZnO is spin-coated at 1000 rpm for 60 s with an annealing condition of 150 °C for 30 min, PEI and ZnO:PEI are cast at 5000 rpm for 60 s before annealing at 120 °C for 20 min and 150 °C for 30 min, respectively. For coating the PDIN-H film, the solution is filtered through a 0.22  $\mu\text{m}$  polypropylene before spin coating at 4000 rpm for 60 s, and the film is annealed at 120 °C for 10 min. For Histidine and Sarcosine, the solution is filtered through a 0.22  $\mu\text{m}$  polypropylene and spin-coated at 5000 rpm for 60 s, followed by annealing at 110 °C for 10 min. Both DM-EELs have a thickness of  $\sim 5$  nm. This procedure is known to provide DM-EELs with complete and smooth coverage as well as a moderate series resistance in OSCs [123].

After coating the EELs, samples are then transferred to a nitrogen-filled glovebox to coat the active layers. Before spin coating, all active-layer solutions are filtered through 0.22  $\mu\text{m}$  PTFE filters. The P3HT:PC60BM layer is coated at 1000 rpm for 80 s and annealed at 150 °C for 30 min, resulting in a thickness of  $\sim 150$  nm. For the PCDTBT:PC70BM active layer, spin coating at 700 rpm for 1min and annealing at 100 °C for 20 min yields an 80 nm-thick film. The PM6:Y6 solution was spin-coated at 3000 rpm for 30 s, followed by annealing at 130 °C for 30 min, resulting in a  $\sim 160$  nm-thick BHJ active layer.

In order to have a more accurate comparison between the different EELs and reduce other confounding factors (small variations in vacuum-deposited layers), each substrate is first cut into four equal pieces, and a different EEL is spin-coated on each piece, followed by the active layer. After

coating the BHJ layer, the four pieces are then taped together and mounted in the vacuum system, and 5 nm of MoO<sub>3</sub> (American Elements) and 100 nm of Aluminum (Angstrom Engineering) are sequentially deposited using an Angstrom Engineering EvoVac thermal evaporator under a base pressure of  $5 \times 10^{-6}$  Torr.

Electron-only devices (EODs) are fabricated using the same procedure, except that D:A BHJ layers are replaced with only acceptors, and LiF (1 nm) is deposited instead of MoO<sub>3</sub>. In addition, for some EODs, 1,3,5-tris(N-phenyl-benzimidazol-2-yl)-benzene (TPBi) purchased from Electronic Materials Index Co is also deposited by evaporation. Hole-only devices (HODs) are fabricated following the same procedure used for the OSCs. However, only donor solutions are spin-coated instead of D:A BHJ layers.

### 3.4 Device Characterization

For photostability tests, one set of the OSCs is exposed to continuous illumination from a 365-nm UV lamp. The 365 nm wavelength is used as it is in the UV<sub>A</sub> range (within the AM1.5 solar spectrum), which has been shown to cause degradation in OSCs [84-86]. The illumination intensity is 8 mA.cm<sup>-2</sup> and is measured with the use of a calibrated pyranometer. The temperature of the cells, monitored by a thermocouple, is ~ 28 °C after four hours of UV irradiation. Another set of cells on the same substrate is kept in the dark (by shielding from the light with a black mask) as a control for the temporal-stability test. The illuminated *J-V* characteristics of all OSCs are measured at consecutive time intervals. The UV illumination is temporarily stopped during the *J-V* measurements to prevent its interference in photogeneration. During all the electrical characterizations and photostability tests, the samples are kept in a N<sub>2</sub>-filled test box and fan-cooled to keep them close to room temperature.

Photodegradation investigations are then pursued through comparative studies of evolutions of encapsulated OSC output parameters under continuous irradiation. By considering decay trends in  $J_{SC}$ ,  $V_{oc}$ , and FF, the first clues about the physical origins of photodegradation can be extracted. For example,  $J_{SC}$  losses mainly originate from photon absorption or charge transport losses, whereas  $V_{oc}$  decay may be attributed to energy level/WF shifts or recombination, as established in Chapter 2. In order to verify whether the decay trends in PV properties are related to absorption loss, transport loss, WF shift or recombination, and how such changes would influence device performance under light exposure, the following characterization techniques are used depending on the PV parameter that shows a significant decay.

### 3.4.1 Solar Simulator *J-V* Measurements

The basic output parameters and OSC performances are measured via light and dark *J-V* characteristics. Illuminated *J-V* measurement is performed under standard 1-sun AM1.5G illumination from an ABET Sun 3000 Class AAA solar simulator using a Keithley 2400 source meter (with ABET Solar Simulator software). For unipolar devices, the same equipment is used in a dark mode.

### 3.4.2 Light-Intensity-Dependent PV Characteristics

The illuminated *J-V* measurements are conducted in the same way described earlier with the same solar simulator but under different illumination intensities. In this experiment, the power supply for the Xeon lamp is tuned to change the illumination intensity. The light intensity of the Xeon lamp with a different power supply is determined by the output parameters of a mono-crystalline silicon reference photodiode and also checked with a pyranometer. The dependence of  $J_{sc}$  on light intensity is given by  $J_{sc} \propto (\text{Light-Intensity})^\alpha$ , where alpha ( $\alpha$ ) is the slope of the  $J_{sc}$  versus light intensity curve on a log-log scale. Generally, an  $\alpha \sim 1$  points to negligible bimolecular recombination, whereas an  $\alpha < 1$  represents significant bimolecular recombination. Notably, there is a major difference between bimolecular recombination in neat inorganic semiconductors versus BHJ OSCs, whose active layer consists of an interpenetrating network of acceptor-rich and donor-rich phases. Because the electrons and holes reside on the acceptor and donor phases, respectively, bimolecular recombination in the case of BHJ OSCs, and thus in our study, refers to the recombination of electrons and holes across these donor/acceptor interfaces [124].

The slope of  $V_{oc}$  against  $\ln(\text{light intensity})$  provides some useful insights into recombination-induced voltage losses, using Equation (3-1) [124-126]. Under open-circuit conditions, generated electron/hole pairs are hardly extracted, where most of them are recombined through bimolecular recombination, which involves electron-hole pair recombination.

$$V_{oc} = \frac{E_g}{q} - \frac{nkT}{q} \ln \left[ \frac{(1-P_D)\gamma N_C^2}{P_D G} \right] \quad \text{Equation 3- 1}$$

In Equation (3-1),  $E_g$  is the energy bandgap,  $q$  is the elementary charge,  $n$  is the light diode ideality factor,  $K$  is the Boltzmann constant,  $T$  is the absolute temperature in Kelvins,  $P_D$  is the dissociation

probability,  $\gamma$  is the Langevin recombination constant,  $N_C$  is the effective density of states, and  $G$  is the generation rate of an electron/hole pair which is affected by the light intensity. Taking into account that  $G$  is proportional to light intensity, the slope of  $V_{oc}$  against the natural logarithm of light intensity gives  $(nKT/q)$ . When  $n$  approaches 1, it can be speculated that only bimolecular recombination exists. However, when additional recombination such as trap-assisted recombination at an open-circuit condition exists, the ideality factor increases from 1 to 2 to the maximum.

### **3.4.3 Low-Temperature Electrical Measurement**

Temperature-dependent  $J$ - $V$  characteristics are measured using a Lakeshore cryogenic probe station in a vacuum condition using a liquid nitrogen-cooled cryostat and under a  $10^{-6}$  Torr pressure.

### **3.4.4 Atomic Force Microscopy**

Atomic force microscopy (AFM) works on the basis of the oscillation of a cantilever with a sharp tip above the sample surface using a piezoelectric actuator. In the tapping mode, where the oscillation amplitude is constant, once the tip touches the sample surface, the cantilever's oscillation amplitude changes as a result of repulsive forces between the surface and the tip. The changes in the oscillation amplitude can be determined by detecting the reflection of a laser beam with a photodiode. To maintain a constant oscillation amplitude, an electronic servo re-adjusts the cantilever height above the sample surface. The vertical adjustments during the scan of the sample surface provide a topographical image of the surface.

In this study, AFM is performed in air with a Veeco-Digital Instruments Dimension 3100 scanning probe microscope in a tapping mode with an etched silicon tip. Roughness measurements are made over 5-10  $\mu\text{m}$  scan sizes and reported based on  $R_{\text{rms}}$ , which is the square root of the sum of squares of all heights from a surface over the entire measured area.

### **3.4.5 Kelvin Probe Force Microscopy**

Kelvin probe force microscopy (KPFM) is primarily based on the instrumentation of an AFM system and measures a contact potential difference (CPD) between the sample surface and the AFM tip, defined as:



$$V_{CPD} = \frac{(\phi_{tip} - \phi_{sample})}{-q}$$

**Equation 3- 2**

In Equation (3-2),  $\phi_{sample}$  and  $\phi_{tip}$  are the work functions of the sample and tip, and  $q$  is the electronic charge. When an AFM tip approaches the sample surface, the differences in the Fermi energy levels of the tip and the sample surface induce an electrical force between them. **Figure 3.4** depicts the energy levels of the tip and sample surface in distance  $d$  and without electrical contact (note, the vacuum levels are aligned, but Fermi energy levels are different). When tip and sample are connected, electrons flow from the material with the smaller WF to that with the larger WF. Thus, the former charges positively while the other charges negatively, forming an electric potential between them. When the electric field nullifies the WF difference between the tip and the sample surface, the electron flow stops. Hence, the system reaches an equilibrium state, and an apparent  $V_{CPD}$  will form. An electrical force acts on the contact area due to the  $V_{CPD}$ . To compensate this force and cancels charges at the contact, an external bias ( $V_{DC}$ ) must be applied with the same magnitude as the  $V_{CPD}$  with opposite direction. The  $V_{DC}$  value that nullifies the  $V_{CPD}$ -induced electrical force is equal to the WF difference between the tip and sample; therefore, the WF of the sample can be calculated when the tip's WF is known [127].

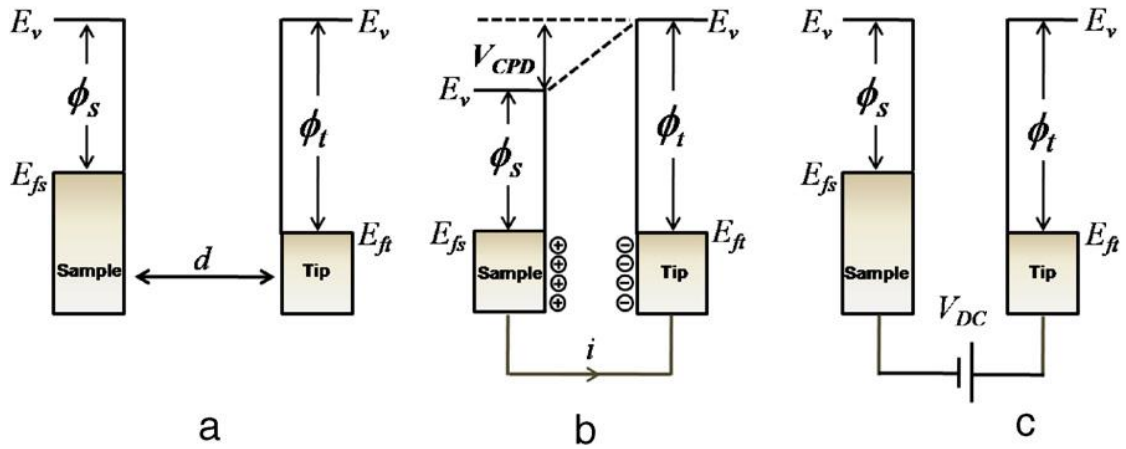


**Figure 3. 4.** Electronic energy levels of the sample and AFM tip in different conditions: (a) tip and sample are separated by distance  $d$  with no electrical contact, (b) tip and sample are in electrical contact, and (c) external bias ( $V_{DC}$ ) is applied between tip and sample.  $E_v$ ,  $E_{fs}$ , and  $E_{ft}$  are the vacuum energy level, sample Fermi energy, and tip Fermi energy, respectively. Reproduced with permission from [127]. Copyright 2010, Elsevier.

In this work, KPFM measurements are done in air using an AIST-NT™ SmartSPM 1000 atomic force microscope. A single MikroMasch® HQ:NSC14 Au coated conductive probe is used, with a tip radius of approximately 35 nm, a resonance frequency of 160 kHz, a force constant of 5 N/m, and a length of  $125 \mu\text{m} \pm 5 \mu\text{m}$ . At least two  $5 \times 5 \mu\text{m}$  images are taken for each of the samples made in each trial. From the images, at least 100 measurements are taken from different areas to determine the average CPD and height values.

### 3.4.6 Absorption Spectra

Absorption measurements are taken with the Shimadzu UV-2501PC on thin films deposited on quartz substrates.

### 3.4.7 Time-Resolved Transient Photoluminescence Spectroscopy

Time-resolved photoluminescence (TRPL) measurements are conducted under ambient conditions, with an Edinburgh Instruments FL920 spectrometer equipped with a 375 nm peak emission EPL375 picosecond pulsed laser diode. First, the sample is excited by the laser diode and generates photoluminescence. Then, the light emitted from the film is detected, at a determined wavelength, as a function of time. The obtained spectra give information about the materials' exciton lifetime.

### 3.4.8 Photoelectron Emission Spectroscopy

Photoelectron emission spectroscopies, namely X-ray photoelectron spectroscopy (XPS) and ultraviolet photoelectron spectroscopy (UPS), are based on the photoelectric effect, and they both are surface-sensitive techniques. The basic principles of XPS and UPS are shown in **Figure 3.5**.

In XPS, an X-ray beam is used to excite core-level electrons. As the binding energy is specific for each element and also depends on its chemical environment, the detected photoelectrons provide information about the samples' chemical composition [128]. The inelastic free mean path of the electron limits the XPS probe to  $\sim 10$  nm from the uppermost surface of the film. For depth profiling, XPS is combined with argon ion sputtering, which enables us to probe the chemical variations from the topmost surface of the film (i.e.,  $\leq \sim 10$  nm) to hundreds of nanometers or more into the bulk. In this thesis, XPS

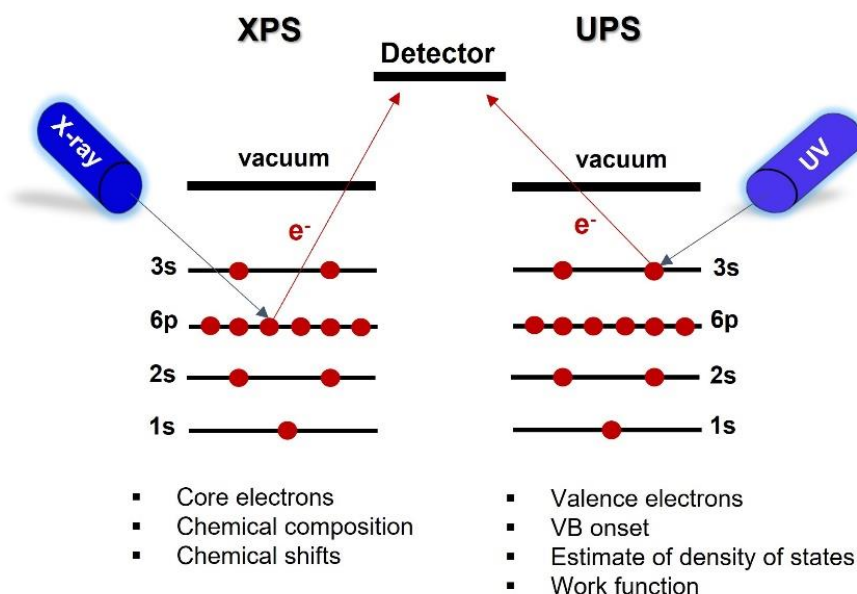


**Figure 3. 5.** Illustration of the principles of XPS and UPS.

measurements are performed by Thermo-VG Scientific ESCALab 250 Microprobe equipped with a monochromatic Al Kalpha X-ray source (1486.6 eV). We also collected XPS scans after sputtering the sample for 300 s using a monoatomic Ar<sup>+</sup> beam with 3 kV energy. CASAXPS software is used for analyzing the XPS spectra, including quantification and band deconvolution.

In UPS, an ultraviolet source is used to measure the kinetic energy of photoexcited electrons from a material. Measuring the onset of the valence band and the photoemission onset caused by inelastically scattered (secondary) electrons allows us to determine the material's work function and ionization potential. Based on the conservation of energy, we find:

$$\phi = h\nu - (E_{\text{cutoff}} - E_F) \quad \text{Equation 3- 3}$$

In Equation (3-3),  $h\nu$  is the excitation source (21.22 eV for HeI),  $E_{\text{cutoff}}$  is the secondary electron cutoff, and  $\phi$  is the WF of the sample. After the electrical contact between the analyzer and sample, the vacuum level shifts to align their Fermi energy levels. For correcting this measurement error, a calibration reference sample is measured to determine the analyzer work function and correct the measured kinetic energy. Therefore, samples must be negatively biased with a voltage  $V_D$  to shift the vacuum level of the sample above that of the detector. UPS measurements in this thesis are carried out by VGS ESCALab 250 electron analyzer operating at a pass energy of 1 eV in an ultrahigh vacuum

system. The excitation source is He I lamp with emission energy of 21.22 eV. A freshly sputtered gold sample is used for calibration, and a negative bias of 5 V is applied to the samples during UPS measurements so that the secondary electrons originating from the sample and spectrometer could be differentiated.

## Chapter 4

# The Role of Introducing Polyethylenimine into the ZnO EEL on the Intrinsic Photostability of OSCs

*This work has been published in Sadeghianlemraski, M., Lee, B. Y., Davidson-Hall, T., Leonenko, Z., and Aziz, H., Organic Electronics, vol. 73, pp. 26-35, 2019. It has been reproduced with minor changes with permission from the publisher.*

### 4.1 Introduction

It was recently shown that using polymeric interfacial layers, such as PEI [129-131] and ethoxylated polyethyleneimine (PEIE) [55, 132, 133], with ZnO can adjust its WF as a result of the formation of an interfacial dipole layer at the ZnO/PEI interface and lead to improvements in device performance. However, the low conductivity of these polymers poses challenges, inspiring the idea of using a ZnO:PEI mixture as an alternative approach [134-136]. Using ZnO:PEI mixture EEL, Liu et al. enhanced PCE of OSCs with PTB7:PC70BM active layer. They also showed that mixing ZnO with a small amount of PEI modifies its WF without appreciably affecting conductivity, optical transmission, or film morphology [136]. Venkatesan et al. [55] showed that introducing a layer of PEIE on ZnO EEL or AZO (Aluminum-doped ZnO) cathode of OSCs can increase their ambient stability; an effect that was attributed to suppressing surface oxidation of the metal oxide layers. Moreover, Shafket et al. [137] recently showed that mixing ZnO with PEIE, when used along with an additional layer of the latter, can improve the light-soaking behavior of OSCs under UV-free irradiation.

While incorporating PEI into EELs is starting to gain momentum in the field, its influence on OSC photostability has not yet been studied to the best of our knowledge. With recent findings by Tournebize et al. [86] of UV-induced shunt formation at the ZnO/active layer interface and the potential benefits of using interfacial buffer layers as a possible way to help eliminate that behavior [86], investigating the effect of modifying that interface on OSC photostability becomes even more compelling. Therefore, in this work, we systematically investigate and compare the behavior of inverted OSCs with ZnO, ZnO/PEI (bilayer), and ZnO:PEI (mixture) EELs, utilizing for that purpose the archetypal P3HT:PC60BM OSC donor:acceptor system. Results reveal that using ZnO:PEI EELs leads to significant

improvements in OSC photostability, resulting in  $\sim 5\times$  higher photostability (around 12% decrease of its initial PCE after 276 h of UV irradiation vs. 60% in the case of ZnO EEL). The stability enhancement is attributed primarily to a much more stable  $V_{oc}$ , the latter being the parameter that typically degrades the fastest in inverted OSCs under UV [86]. Findings from electron-only devices as well as AFM, KPFM, and XPS measurements reveal that the ITO/EEL interface plays a more influential role in the photodegradation behavior of OSCs relative to the EEL/BHJ interface, contrary to what was believed.

## 4.2 Results and Discussion

Three groups of OSCs of the structure: ITO/EEL/P3HT:PC<sub>60</sub>BM/MoO<sub>3</sub>/Al, each consisting of 8 identical cells, utilizing ZnO, ZnO/PEI bilayer, or ZnO:PEI mixture as EELs were fabricated. The EEL thickness was approximately 35-40 nm in all cases, included the thickness of the PEI layer ( $\sim 5-7$  nm) in the ZnO/PEI EEL case. **Figure 4.1.a** depicts the device structures. All devices were fabricated and tested under the same conditions. The PV parameters of these cells under 1 sun 1.5 AM radiation are provided in Table 4.1, where all numbers represent average values from the 8 cells in the group except for the last row, which presents the maximum PCE value in each group. The J-V characteristics of the cells with the highest PCE in each group are provided in **Figure 4.1.b**. We should point out that the specific ZnO:PEI mixing ratio (1:0.04 by weight) was selected based on preliminary work that showed that it gave better photovoltaic performance relative to other ratios (data from that work is provided in Table 4.2).

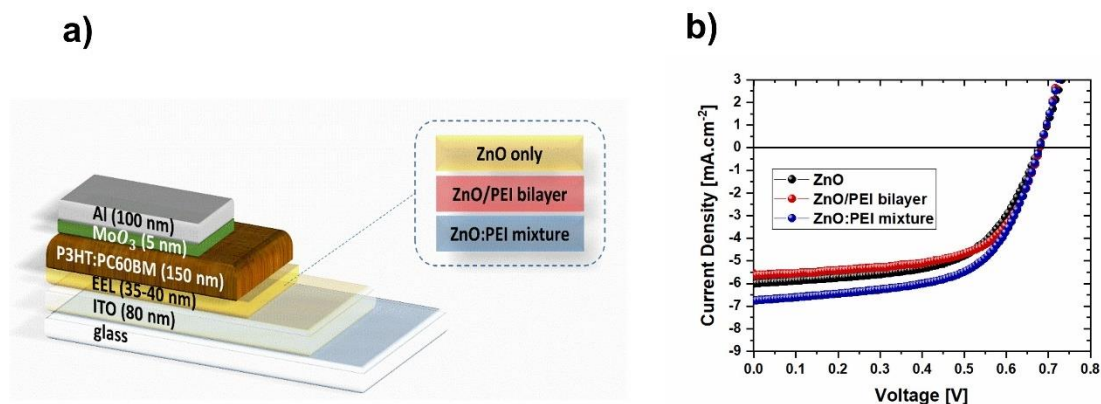


**Figure 4. 1.** a) A schematic depiction of the structure of the OSCs used in this work. b)  $J$ - $V$  characteristics of OSCs with the highest PCE with the ZnO, ZnO/PEI, and ZnO:PEI EELs, measured under 1-sun AM1.5G illumination.

As can be seen from the data in Table 1, devices with ZnO EEL, which are used here as reference devices, demonstrate an initial PCE of about 2.4%, on par with other reports for this device structure [86]. Generally, the PV parameters of devices from the three groups are comparable, with the ZnO:PEI EEL devices having somewhat higher PCE and  $J_{sc}$ , exhibiting average and maximum PCE of 2.56% and 2.75%, respectively, versus 2.38% and 2.46% in the ZnO reference devices, and a  $J_{sc}$  of 6.43 mA.cm<sup>-2</sup> versus 6.25 mA.cm<sup>-2</sup> in the reference devices. The small increase in  $J_{sc}$  on using ZnO:PEI instead of ZnO as EEL is in good agreement with previous reports [135]. We note that the  $J_{sc}$  in the ZnO/PEI devices was generally somewhat lower than in the ZnO case in our devices and was in line with the work by Venkatesan et al. [55].

**Table 4. 1.** PV parameters of OSCs with the ZnO, ZnO/PEI (bilayer), and ZnO:PEI (mixture) EELs.

<b>EEL</b>	<b>ZnO</b>	<b>ZnO/PEI bilayer</b>	<b>ZnO:PEI mixture</b>
<b>Parameters</b>			
$J_{sc}$ [mA.cm <sup>-2</sup> ]	6.25 ± 0.55	5.33 ± 0.23	6.43 ± 0.31
$V_{oc}$ [mV]	668.58 ± 14.4	666.98 ± 13.4	672.45 ± 4.6
FF [%]	57.11 ± 3.17	59.99 ± 1.47	59.25 ± 1.23
Ave – PCE [%]	2.38 ± 0.07	2.13 ± 0.11	2.56 ± 0.14
Max – PCE [%]	2.46	2.38	2.75

**Table 4. 2.** PV parameters of OSCs with ZnO:PEI EEL with different weight mixing ratios of (1:0.01), (1:0.02), (1:0.03), and (1:0.04).

<b>ZnO:PEI %wt</b>	<b>1 : 0.01</b>	<b>1 : 0.02</b>	<b>1 : 0.03</b>	<b>1 : 0.04</b>
<b>Parameters</b>				
$J_{sc}$ [mA.cm <sup>-2</sup> ]	6.18	6.31	6.14	6.75
$V_{oc}$ [mV]	676	672	685	679
FF [%]	56.04	55.68	58.68	59.97
PCE [%]	2.34	2.36	2.46	2.75

In order to investigate and compare between the photostability performance of the OSCs, the devices were exposed to continuous illumination from a 365 nm UV source at an illumination power density of  $8 \text{ mW/cm}^2$ . The  $J$ - $V$  characteristics (again under 1 sun, AM 1.5) of the OSCs were collected at various times during the UV exposure (with the UV illumination temporarily blocked during the measurements to prevent contributions from the UV illumination to carrier photogeneration). **Figure 4.2** shows the obtained PCE,  $V_{oc}$ , FF, and  $J_{sc}$  at those times, normalized to their initial (i.e., time zero) values. As can be seen from the figure, prolonged exposure to UV causes a deterioration in the PV parameters of all devices as expected, but the degradation was slower in devices containing PEI in their EELs. Remarkably, the ZnO:PEI OSC exhibited significantly higher stability, showing only about a 12% decrease in PCE after 276h UV irradiation,  $\sim 5$ x smaller than that observed in the ZnO OSC. The largest difference is observed in  $V_{oc}$  and FF, with the earlier showing a decrease of 1.26%, 11.9%, and 29.5% in the devices with the ZnO:PEI, ZnO/PEI, and ZnO EELs, respectively, after 276 hours of UV exposure. It should be noted that this large degradation in  $V_{oc}$  in the control device is consistent with the literature [55, 69, 85, 86]. Besides, we note that the  $V_{oc}$  photostability of OSCs with ZnO/PEI EEL is somewhat higher than the ZnO-based devices while lower than the cells with ZnO:PEI EEL. In contrast, the  $J_{sc}$  degradation trends were comparable in all devices, with the ZnO OSC showing only slightly faster degradation than the other two devices. The comparable  $J_{sc}$  loss indicates that, unlike  $V_{oc}$  and FF, its origins are independent of the EEL, and suggests it may be associated with changes in the active layer bulk, perhaps due to PC<sub>60</sub>BM dimerization, established earlier in chapter 2 [55, 84-86, 92].

In order to determine if the UV irradiation indeed caused the observed changes in the PV characteristics of the OSCs, we similarly tested the  $J$ - $V$  characteristics of an identical set of devices that were kept in the dark over the same period to be used as a control set for comparison. Table 4.3 compares the changes in the PV parameters of the UV-irradiated and the control devices over the same period (276 hours). Clearly, the control devices exhibit much smaller changes in their PV parameters in comparison, verifying that the degradation observed in the case of the UV-irradiated devices was indeed caused mainly by the UV exposure. Considering that the only difference between the three sets of devices is their EELs, the significant differences in their photostability behavior must be associated with the EELs, and more specifically, their (i.e., the EEL's) role in influencing the stability of the  $V_{oc}$  and FF over time, and, as a result, PCE.



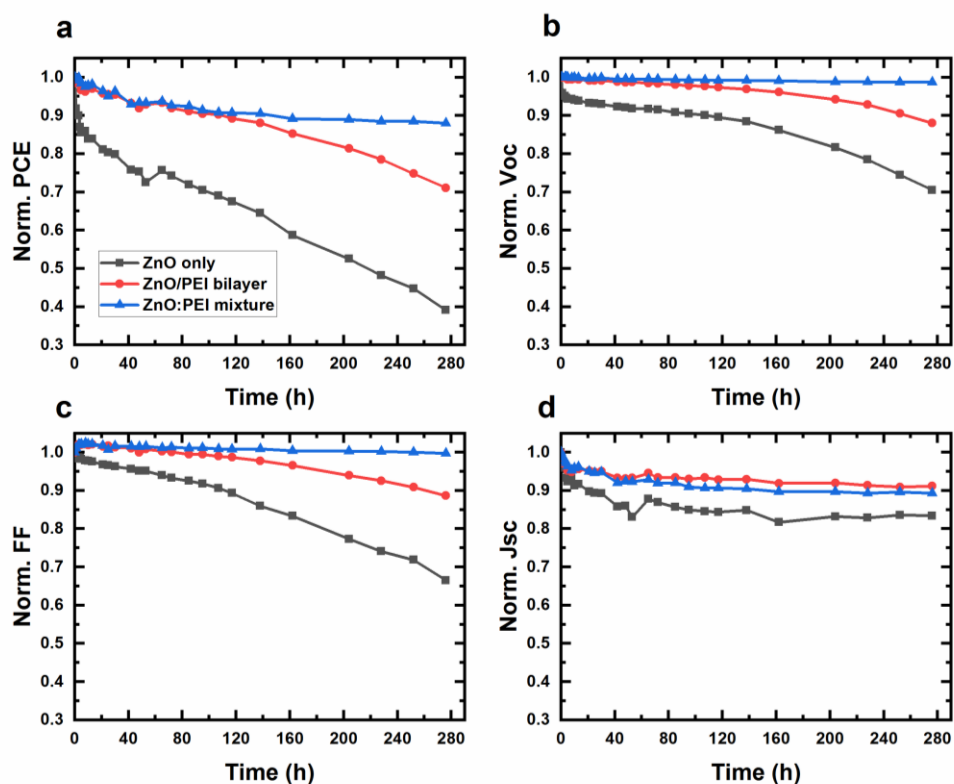


**Figure 4. 2.** Normalized PCE (a),  $V_{oc}$  (b), FF (c), and  $J_{sc}$  (d) versus time under continuous UV irradiation of OSCs with the ZnO, ZnO/PEI, and ZnO:PEI EELs.

**Table 4. 3.** % change in PV parameters of OSCs with the different EELs after 276 hours of UV irradiation and a control set of identical OSCs kept in the dark (i.e., no UV) for the same period.

Parameters	% $\Delta J_{sc}$		% $\Delta V_{oc}$		% $\Delta FF$		% $\Delta PCE$	
	Control	UV	Control	UV	Control	UV	Control	UV
<b>ZnO only</b>	-6.54	-16.6	-1.43	-29.5	+0.83	-33.5	-6.71	-60.87
<b>ZnO/PEI bilayer</b>	-4.33	-8.83	-1.08	-11.9	+0.33	-11.35	-5.06	-28.9
<b>Mixed ZnO:PEI</b>	-6	-10.69	-0.016	-1.26	+0.45	-0.25	-1.74	-12

In order to identify the role of the ZnO/PEI and ZnO:PEI EELs in enhanced photostability and to investigate whether it is associated with improving the stability of the electron collection contact and reducing its susceptibility to photo-induced degradation [44, 45, 138], we tested the EELs in EODs. First, we incorporate the EELs in EODs of the structure: ITO/ EEL/TPBi/LiF/Al. The device structure is depicted in the inset of **Figure 4.3.a**. TPBi, an electron transport material, is used because of its relatively high electron mobility and low optical absorption at 365 nm [139], making it not susceptible to UV-induced photodegradation. As such, any changes in EOD electrical characteristics due to UV irradiation will not be due to changes in the TPBi layer. Under forward bias, defined as holding the Al electrode at a more negative potential relative to the ITO electrode, electrons are efficiently injected from the LiF/Al contact and transported into the TPBi and then into the EELs before they eventually get collected at the ITO electrode. Thus, the electron flow in the EELs and their collection at the ITO/EEL contacts resembles that of the photogenerated electrons in the OSCs. In contrast, hole injection from ITO under the same bias direction is obstructed by the large energy offset between the ITO work function and the valence band of the ZnO. As such, the flow of current occurs almost exclusively via electrons.

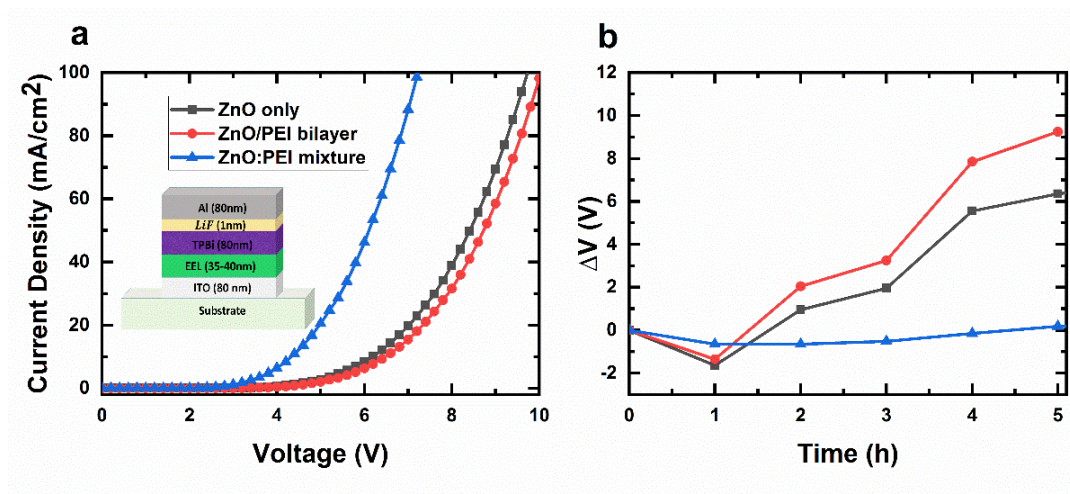


**Figure 4. 3.** a)  $J$ - $V$  characteristics collected in the dark for EODs with ZnO, ZnO/PEI, or ZnO:PEI contacts. Insets: the structure of EODs used in this work. b) Net change in the driving voltage ( $\Delta V$ ), defined as voltage needed to maintain a current density of  $20 \text{ mA}\cdot\text{cm}^{-2}$  at any time  $t$  minus the initial voltage at the same current density, under 5 h UV irradiation for the three contacts of interest.

**Figure 4.3.a** shows  $J$ - $V$  characteristics of these EODs with the different EELs, collected in the dark. As can be seen, the use of ZnO:PEI EEL leads to a higher current relative to the other devices at any given driving voltage, pointing to its higher conductivity and/or more efficient electron collection at the two EEL interfaces. As the EODs with the ZnO and ZnO/PEI EELs have different EEL/TPBi interfaces (no PEI in the first vs. PEI in the second), their similar  $J$ - $V$  characteristics suggest that the EEL/TPBi interface does not strongly influence or limit electron collection in these devices, indicating that the higher current in case of the ZnO:PEI is not due to easier electron collection at the ZnO:PEI/TPBi interface and is therefore due to the higher bulk conductivity of the ZnO:PEI and/or more efficient electron collection at the ITO/ZnO:PEI interface.

One set of EODs was then exposed to continuous UV illumination (same conditions as above) and their  $J$ - $V$  characteristics were measured (in the dark) at certain time intervals. Changes in their forward bias driving voltage, defined as the voltage needed to maintain a constant current density of  $20 \text{ mA}\cdot\text{cm}^{-2}$  and presented in the form of the net change in voltage  $\Delta V = \text{the voltage at any time } t \text{ minus the initial voltage}$ , are provided in **Figure 4. 3.b**. Clearly, the illumination causes a faster rise in the driving voltage over time in the case of the EODs with the ZnO and ZnO/PEI EELs, indicating that electron transport and collection becomes increasingly less efficient. In contrast, the driving voltage trend of the EOD with the ZnO:PEI EEL remained remarkably much more stable, pointing to the role of this EEL in reducing UV-induced deterioration in electron transport and collection, and maintaining efficient electron collection over time. It is also clear that although the EODs with the ZnO and ZnO/PEI EELs have different EEL/TPBi interfaces, they both exhibit low stability. It follows from these results that the much higher photostability of the ZnO:PEI EEL must be related to factors associated with the EEL bulk and/or the ITO/EEL interface (which, in this case, can be expected to be altered due to the presence of PEI in the mixture) in influencing the photostability behavior of OSCs. Although higher photostability of the OSCs with ZnO/PEI EEL compared to the ZnO-based cells suggests that having PEI at the BHJ interface may have some photostability benefits for the BHJ as was also reported recently [86], the fact that the EODs with the ZnO and ZnO/PEI EELs generally have similar stability trends shows that the EEL/BHJ interface plays a smaller role in comparison in influencing the photostability behavior of the OSCs. It should be pointed out that this is different from the short-term “light-soaking” behavior observed in OSCs with metal-oxide EELs, especially those processed in air, which, in contrast, is more strongly influenced by the EEL/BHJ interface [85, 140].

Finding out that the ZnO:PEI EEL leads to a significant enhancement in OSC photostability and that the effect is most likely due to maintaining a more stable electron collection efficiency across the EEL and/or ITO/EEL contact, it becomes important to investigate the root causes of this behavior. We, therefore, use AFM and KPFM to respectively study the morphological and electrical surface potential characteristics of the ZnO, ZnO/PEI, and ZnO:PEI as well as of the bare ITO, and to probe any changes in those characteristics under UV irradiation.

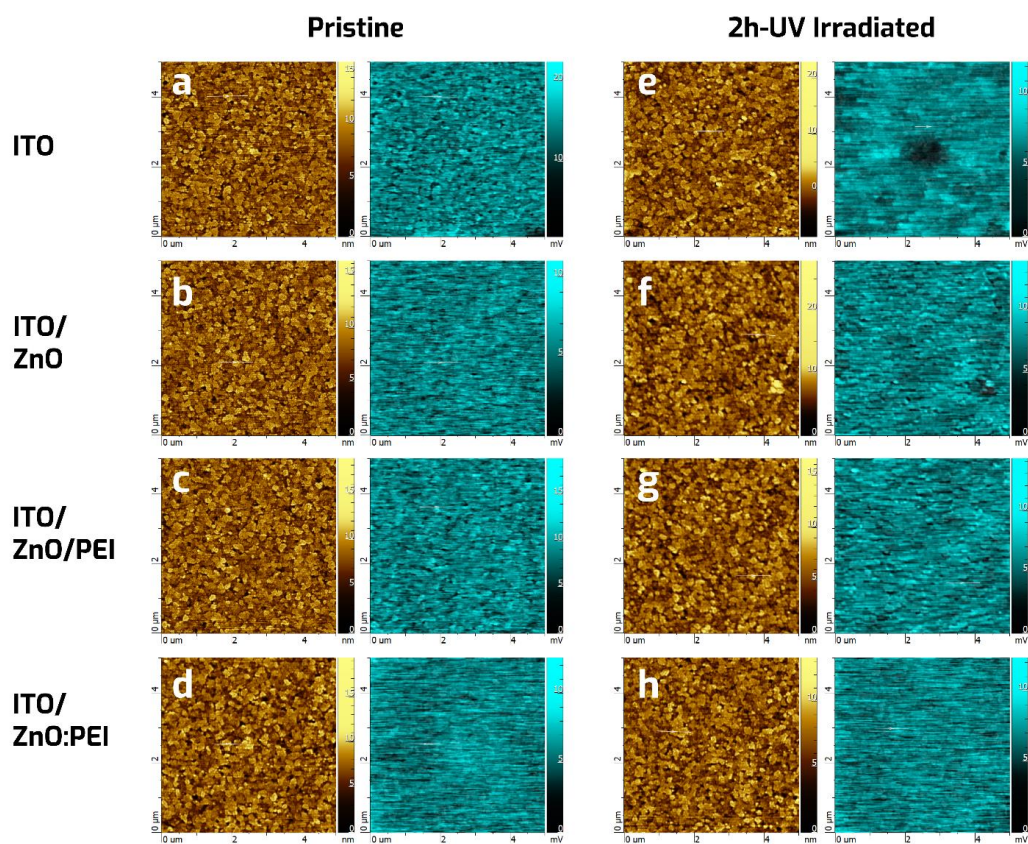


**Figure 4. 4.** AFM (golden) and KPFM (blue) images of ITO Control, ZnO, ZnO/PEI, and ZnO:PEI films; before (a, b, and c, d respectively) and after 2 hours of UV irradiation (e, f, g, and h).

AFM images (golden) and KPFM images (blue) collected from ITO, ITO/ZnO, ITO/ZnO/PEI, and ITO/ZnO:PEI films before (pristine) and after 2 h of UV irradiation are provided in **Figure 4.4**. The images were collected simultaneously from the same sample area in order to allow comparing their surface topography and electrical surface potential. For obtaining the KPFM images, the surface of the

sample is scanned with a probe tip that measures the potential difference, CPD, between the sample surface and the tip. This potential difference will generally depend on the work function of the surface and tip materials as well as on the electrical surface potential of material surfaces, as described in chapter 3. Although the absolute value of the measured CPD depends on the specific experimental setup, imaging the sample surface with the same probe can reveal differences in electrical surface potential among the samples.

Looking at the AFM images, a comparison of all the pristine films (**Figure 4.4 (a)-(d)**) shows that they all have similar surface topography with the ITO/ZnO:PEI film having a slightly smoother surface relative to ITO/ZnO, ITO/ZnO/PEI and the ITO control, with an  $R_{rms}$  of  $1.34 \text{ nm} \pm 0.01 \text{ nm}$  versus  $1.41 \text{ nm} \pm 0.08 \text{ nm}$ ,  $1.42 \text{ nm} \pm 0.10 \text{ nm}$  and  $1.40 \text{ nm} \pm 0.09 \text{ nm}$  in the other three films, respectively. After UV irradiation (**Figure 4.4.e-h**), the  $R_{rms}$  values change slightly for each film, with the ITO/ZnO film being affected the most (by about 0.4 nm instead of 0.1 nm in the other films). While the increase in roughness might suggest that ZnO is susceptible to UV-induced degradation, a phenomenon observed in other materials [141, 142], the morphological differences among the samples were too small to be expected to play a significant role in the different photostability behavior of the EELs.

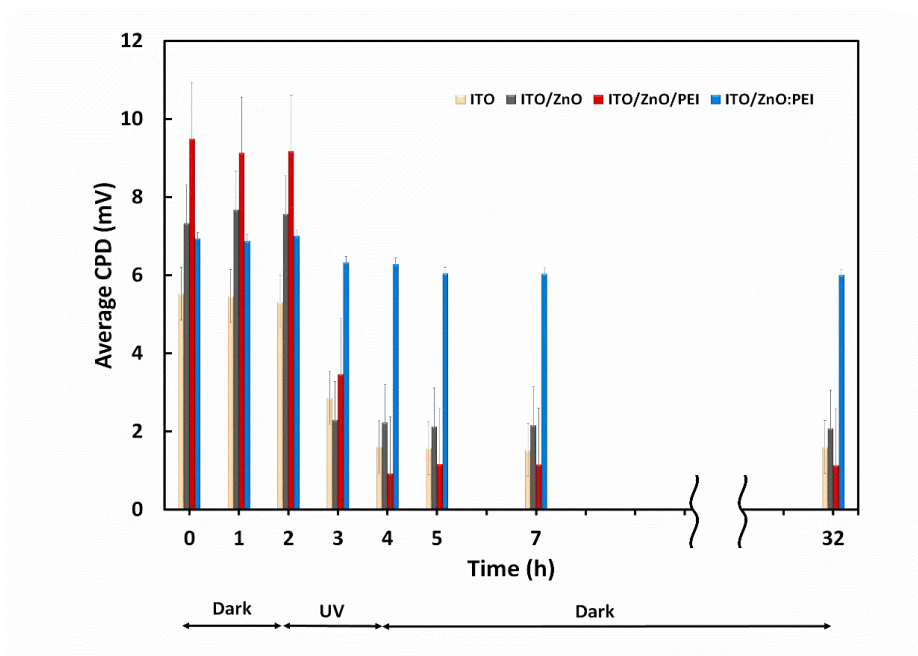


**Figure 4. 5.** Average CPD versus time for the ITO, ITO/ZnO, ITO/ZnO/PEI, and ITO/ZnO:PEI samples. The samples were kept in the dark during the first 2 hours, exposed to UV irradiation during the next 2 hours, and then kept in the dark again during the last 28 hours. The height of each column represents the average value of 100 points on the sample surface.

**Figure 4.5** gives the average CPD values obtained from KPFM scans of the sample surfaces at various times with the samples initially being kept in the dark (for 2 hours), followed by UV irradiation (for 2 hours), and then again being kept in the dark (for 28 hours). The averages are obtained from measuring CPD at 100 different points on the surface of each sample at the given times. As can be seen from the figure, CPD does not change appreciably in all samples while in the dark. Illumination, however, leads to significant changes in CPD in the ITO, ITO/ZnO, and ITO/ZnO/PEI samples, pointing to UV-induced changes in surface potential. In contrast, the changes in CPD under UV were much smaller in the ITO/ZnO:PEI sample. Notably, the photoinduced changes in CPD do not show any significant changes upon leaving the samples in the dark for 28 hours following the illumination. This shows that the photoinduced degradation is not reversible in the dark, at least when no external stimulus (a reverse bias) is applied [96, 143].

As changes in electrical surface potential of a sample mirror changes in its electrical properties, including work function [144], the results suggest that the exposure to UV brings about more significant changes in work function in the case of the ZnO and ZnO/PEI EELs than in the case of the ZnO:PEI EEL. It is for example known that although UV illumination can initially improve the performance of OSCs, prolonged illumination can induce the formation of chemical defects and the introduction of interstitial oxygen in ZnO that lead to an increase in its work function and reduce its n-type characteristics in the longer term [85, 96, 110]. The fact that a similar change in electrical surface potential is observed in ITO/ZnO/PEI, where the presence of the PEI would expectedly interfere with reactions between oxygen and ZnO surface, suggests that additional factors, including ones that may not necessarily be at the stack surface, could however be involved. It is, for example, possible that the changes arise from a shift in ITO work function which is also known to occur under illumination [97, 145]; such an effect is also evident from the changes in CPD of the bare ITO samples measured here. A change in ITO work function could lead to a change in the surface potential of subsequent layers due to a vacuum level shift at the ITO/EEL interface. In this context, the use of ZnO:PEI instead of neat ZnO may perhaps alter this behavior and thereby stabilize ITO work function. Regardless of the specific underlying factors, the results clearly show that the surface potential of the ITO/ZnO:PEI remains relatively unchanged under the UV stress, an effect that is clearly different from that observed with the other EELs or the bare ITO. This observation may explain the enhanced  $V_{oc}$  photostability of OSCs utilizing this EEL [55].

In order to investigate the origins of the different behavior of the CPD in the ITO/ZnO:PEI vs. the other samples, we use XPS measurements to study and test for any changes in the surface chemistry of the UV-irradiated versus pristine ITO, ITO/ZnO:PEI and ITO/ZnO films. The XPS scans of the binding energy of the C 1s and O 1s peaks for the ITO sample and C 1s electrons for ITO/ZnO and ITO/ZnO:PEI samples are presented in supporting information (**Figure S4.1**). **Figure 4.6** shows O 1s and Zn 2p peaks for the ITO/ZnO:PEI and ITO/ZnO samples. In order to probe the effect of UV irradiation on the ITO/EEL in the ITO/ZnO:PEI and ITO/ZnO samples, we also collect XPS scans after sputtering the sample for 300s using Ar+ in order to remove the EEL.

First, looking at results from the bare ITO samples, the surface C 1s spectrum (**Figure S4.1. a**) can be resolved into 4 bands, with peaks at 285.5, 287.2, 289, and 291.2 eV for the pristine ITO film; can be assigned to various C-C and C-O bonds. The presence of some of these bands may be attributed to contamination from the tape used for mounting the samples. The UV exposure caused the 291.2 eV band to disappear and altered the relative intensities of the other three bands. The O 1s spectrum of the ITO surface (**Figure S4.1.b**) showed two distinct peaks and can be de-convoluted to 3 bands, with maxima at 530.5, 531.9, and 534.9 eV in the case of the pristine ITO, with one of them, the 534.9 eV band, again absent in the UV-irradiated ITO. This band can be attributed to carbonyl oxygen [86], perhaps associated with reactions between chemisorbed O (from the ambient or released from the ITO surface) and C (from the sample environment) on the ITO surface. UV illumination causes the photo-oxidation of these organic contaminants and/or the dissociation of these O-C bonds, leading to their disappearance from the spectrum of the UV exposed samples. The loss of chemisorbed oxygen may play a role in lowering the WF of ITO surface under UV illumination [97, 146].

In the case of ZnO, the surface C 1s spectrum was essentially identical for the pristine and the UV – irradiated samples (**Figure S4.1.c**). The surface O 1s core-level spectrum (**Figure 4.6 (I).a**) of the pristine film included contributions from oxygen on lattice sites ( $O_l$ ) with a peak at 531.6 eV and oxygen in vacancy sites or defects ( $O_v$ ) at 533.2 eV. Exposure to UV does not alter the binding energy of these bands. The Zn 2p spectra (**Figure 4.6 (II).a**) showed bands at 1023.1 eV and 1046.2 eV, typical of crystalline ZnO [147], and were again essentially the same in the pristine and the UV-irradiated samples. XPS spectra collected after sputtering the EEL, and hence from a region closer to the ITO/EEL interface, show essentially the same bands for all C 1s, O 1s, and Zn 2p electrons (**Figures S4.1.d, 4.7 (I).b and 4.6 (II).b**, respectively) but with a slight shift, amounting to about 0.2 - 0.6eV, in both samples. Additionally, the relative intensities of  $O_l$  and  $O_v$  were different, giving a  $O_l/O_v$  intensity ratio

of  $\sim 2.7$  instead of 0.3 in the case of the surface spectra of the pristine samples. The lower ratio at the surface suggests that more defects and vacancy sites are present closer to the ZnO surface.

Turning now to the case of ZnO:PEI, the surface C 1s spectrum was again essentially identical for the pristine and the UV-irradiated samples (**Figure S4.1.e**). The surface O 1s core-level spectrum (**Figure 4.6 (I).c**) of the pristine film again included contributions from  $O_l$  and  $O_v$ , with peaks at 531.4 eV and 533 eV, respectively, plus, a third component with a peak at 534.6 eV associated with chemisorbed molecules and/or hydroxyl groups ( $O_c$ ). The  $O_l$  and  $O_v$  bands were not altered by the UV stress and only the chemisorbed oxygen band,  $O_c$  show a 0.5 eV increase in binding energy. The Zn 2p spectra (**Figure 4.6 (II).c**) show bands at 1022.8 eV and 1045.9 eV, typical of crystalline ZnO [147], and are again essentially the same in the pristine and the UV-irradiated samples. In general, a comparison of all C 1s, O 1s, and Zn 2p bands with those of the ZnO EEL discussed previously shows a  $\sim 0.2$ - $0.3$  eV shift to lower binding energies. A rigid shift in all bands suggests that it may be due to a dipole formation, perhaps arising from the presence of the PEI, which contains amine groups. Interestingly, and in marked contrast to the surface spectra and to results from the ITO/ZnO sample, XPS spectra collected after sputtering the ZnO:PEI, and thus from a region closer to the ITO/EEL interface, show new bands in the UV-irradiated samples. The O 1s spectrum of the UV-irradiated sample (**Figure 4.6 (I).d**) shows new bands at 535.3 eV and 537.6 eV which are characteristic of O in zinc acetate and carbonyl groups [147, 148], respectively. Similarly, the Zn 2p spectrum of the UV-irradiated sample (**Figure 4.6 (II).d**) shows new bands at 1026.1 eV and 1049.2 eV, usually assigned to Zn-C bonds in zinc acetate. The appearance of these new bands points to the formation of new chemical species from reactions activated by UV excitation. That these bands exist more near the ITO interface and only in the case of the ITO/ZnO:PEI sample indicates that species from both PEI and ITO are involved in those reactions. The results therefore indicate the formation of a new “chemical interface” in the case of the ITO/ZnO:PEI contact under UV. The fact that this new “chemical interface” is created by UV and that the same contact, i.e. ITO/ZnO:PEI, gives the most stable surface potential, as evident from the KPFM measurements, suggests that the two phenomena may be correlated; i.e., that this new interface allows maintaining a more stable contact potential despite the UV exposure. Knowing that oxygen and ITO surface reactions can occur under UV illumination and cause shifts in work function [144, 146], forming a chemical interface where a larger fraction of oxygen atoms are chemically bonded to other species can be expected to reduce such effects.



In addition to the abovementioned observations, comparing the C 1s, O 1s, and Zn 2p electrons binding energy of the ZnO:PEI sample (**Figure S4.1.f 6(I).d, and 6(II).d**) with that of the ZnO sample near the ITO interface (**Figure S3.d, 4.6 (I).b, and 4.6 (II).b, respectively**), a larger shift to lower binding energy, amounting to about 0.4-0.9 eV in ZnO:PEI, versus only 0.2-0.6 eV in ZnO, is observed. The shift suggests that it can be due to a stronger dipole formation near the ITO interface. This stronger dipole formation may perhaps be behind the lower CPD in the case of the pristine ZnO:PEI when compared to the pristine ZnO film, provided in **Figure 4.5** and contributes to the somewhat better initial PV properties of OSCs with ZnO:PEI (Table 4.1) in agreement with previous reports [136].

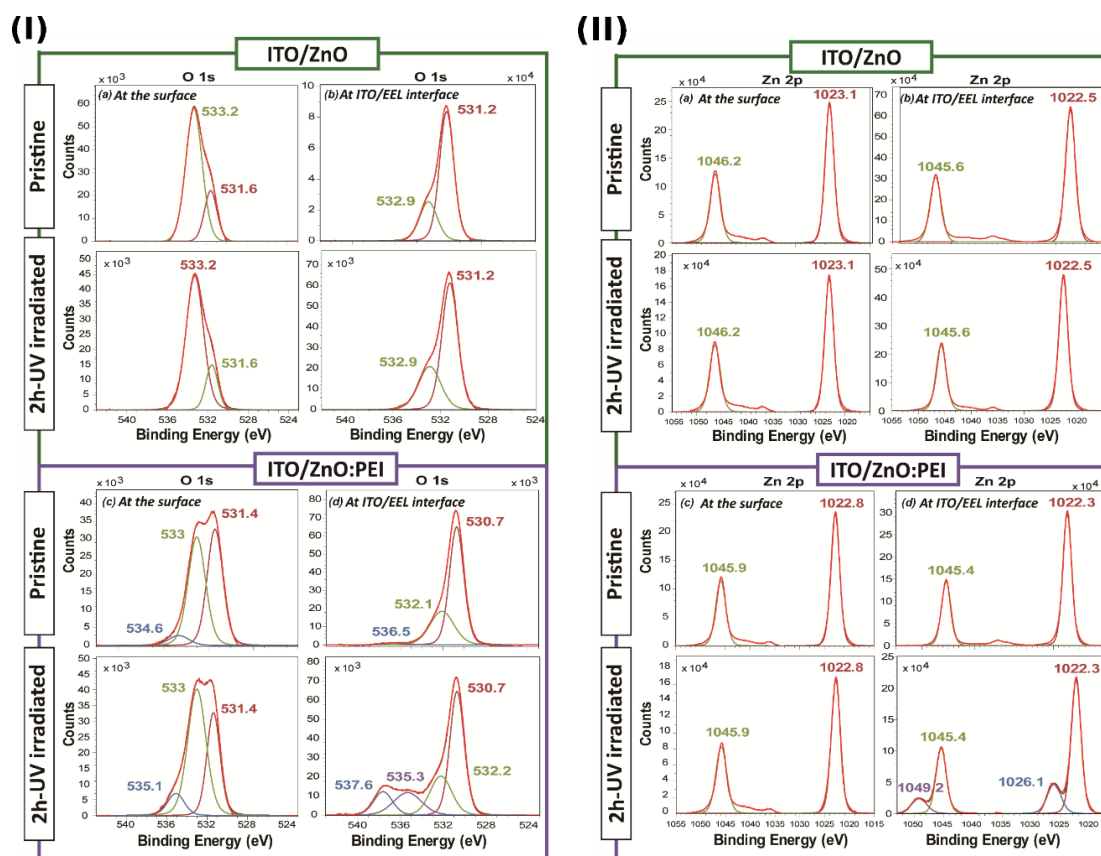


**Figure 4. 6.** XPS spectrum of (I). O 1s, and (II). Zn 2P, for pristine and UV-irradiated ZnO and ZnO:PEI films; at the surface (a and c), and at the ITO/EEL interface (b and d).

### 4.3 Conclusions

In conclusion, results show that introducing PEI in the commonly used ZnO EELs reduces the susceptibility of OSCs to photodegradation, with the ZnO:PEI mixture providing a 5x higher PCE stability under continuous UV irradiation, mainly due to a more stable  $V_{oc}$  and FF. Using a ZnO/PEI bilayer as the EEL also improves the photostability compared to the ZnO-based cells, suggesting that having PEI at the BHJ interface has some photostability benefits. However, more significant stability enhancements of the ZnO:PEI mixture and tests on electron-only devices show that the higher photostability of the ZnO:PEI mixture is mainly due to maintaining a more stable electron collection efficiency across the EEL and/or ITO/EEL contact. KPFM and XPS measurements reveal that the stability enhancement is associated with chemical interactions between PEI and ITO at the ITO/ZnO:PEI interface that produces a more electronically stable contact that is less susceptible to changes in surface potential or work function by UV illumination. The results not only reveal the potential of utilizing PEI in the EEL as an effective route to enhance OSC photostability but also address some of the origins of the limited photostability of OSCs.

## Chapter 5

### The Effect of Modifying ZnO Surface with an N-annulated Perylene Diimide (PDIN-H) on the Intrinsic Photostability of OSCs

*This work has been published in Sadeghianlemraski, M., Harding, C. R., Welch, G. C., and Aziz, H., ACS Applied Energy Materials, vol. 3(12), pp. 11655-11665, 2020. It has been reproduced with minor changes with permission from the publisher.*

#### 5.1 Introduction

As discussed earlier, OSCs with a ZnO EEL suffer from several limitations. For instance, intrinsic incompatibilities between ZnO as an inorganic metal oxide and the next organic active layer negatively affect charge transport [85, 86, 105], an effect that makes the use of surface modification or interfacial layers in between the ZnO and the active layer often beneficial [149]. Also, photoinduced shunt formation at the ZnO/active-layer interface, induced by the UV components of the solar spectrum, results in a deterioration in the efficiency of the cells over time [69, 85, 96]. Surface defects in ZnO have been found to be behind the UV-induced shunt formation [85]. Kam et al. [69] significantly reduced the UV-induced shunt formation and selectivity loss of OSCs with the ZnO EEL by utilizing an ultrathin layer of Al as a ZnO surface modifier. They, however, did not provide the exact mechanism behind this improvement.

Several reports have described modifying the surface of ZnO using different materials as surface modifiers [69, 150, 151]. Among them, PDI groups have recently attracted considerable attention since the easy functionalization of the PDI chromophore with different side chains enables the processing of water/alcohol soluble materials and modifying the interlayer WF [150, 152]. Additionally, perylene derivatives have been shown to facilitate charge transport and to have excellent thermal, chemical, and photochemical stability [153]. Amine group functionalized PDI (i.e., PDIN) has been reported to serve as a ZnO modifier that improves OSCs initial performance [154]. Harding et al. [154] have recently introduced an N-annulated PDI dye with a pyrrolic NH functional group, called PDIN-H, that can be deprotonated for facile green solvent processing into uniform thin films which have a high robustness to a wide range of solvents. They have also demonstrated the ZnO/PDIN-H EEL's applicability in

inverted OSCs, achieving reasonable initial performance. Despite these benefits of the PDI derivatives, their effects as ZnO surface modifiers on OSC photostability have not been studied to the best of our knowledge.

Knowing from the abovementioned studies that the use of interfacial layers between ZnO and active layer can influence OSC performance, and considering the high photostability of PDI derivatives, it becomes interesting to investigate the influence of using this new EEL system (ZnO/PDIN-H) on OSC photostability. Therefore, we have conducted this study to systematically investigate the photostability behavior of inverted OSCs with ZnO and ZnO/PDIN-H EELs using P3HT:PC60BM as a widely used donor-acceptor BHJ system. Results illustrate that the ZnO/PDIN-H EEL device exhibits significantly higher photostability relative to those with the ZnO EEL. We have also investigated the origins of the photostability enhancement. As verified by dark  $J$ - $V$  characteristics of the solar cells, using the ZnO/PDIN-H EEL suppresses the UV-induced increase in the reverse current observed in the cells with ZnO, boosting  $V_{oc}$  stability. Light intensity dependence of the FF along with the voltage dependence of light and dark ideality factors reveals that the higher FF stability of the cells with ZnO/PDIN-H originates from a significant hindrance of the UV-induced transition in recombination mechanisms that occurs in the cells with ZnO.

## 5.2 Results and Discussion

We investigate the effect of adding a neat layer of PDIN-H, ~10 nm thick, on top of the ZnO, to make a bilayer EEL, on OSC photostability. This thickness was selected based on our recent findings [154] that it allows for the formation of a complete layer with uniform coverage yet at the same time keeps absorption in the 350-650 nm range and any subsequent photogeneration negligible, as is also verified by optical measurements in this work (**Figure 5.1**). OSCs with the structure of ITO/EEL/P3HT:PC60BM/MoO<sub>3</sub>/Al (shown in the inset of **Figure 5.2.a**), where ZnO or ZnO/PDIN-H is used as the EEL, were therefore fabricated, and their performance was compared.

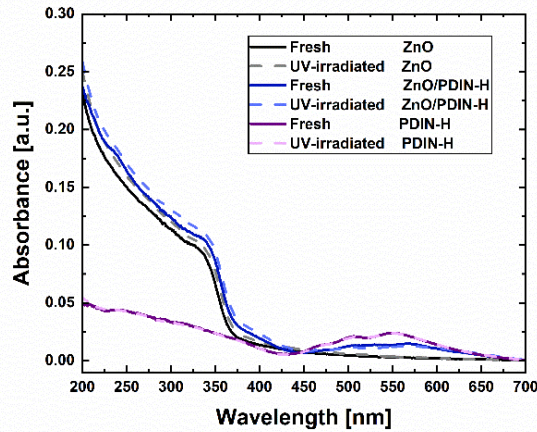


**Figure 5. 1.** UV-Vis absorption spectra of pristine (solid lines) and 200 h UV-irradiated (dotted lines) of ZnO (black), ZnO/PDIN-H (blue), and PDIN-H (purple) films.

**Table 5. 1.** PV parameters of fresh and UV-irradiated solar cells with the ZnO and ZnO/PDIN-H EELs.

EEL	ZnO		ZnO/PDIN-H	
	Fresh	UV-irradiated	Fresh	UV-irradiated
$J_{sc}$ [ $\text{mA}\cdot\text{cm}^{-2}$ ]	6.99	6.13	6.87	6.76
$V_{oc}$ [mV]	659.19	450.36	651.01	613.45
FF [%]	59.41	39.24	59.61	55.09
PCE [%]	2.74	0.99	2.67	2.28

We then probed the influence of the different EELs on the initial performance of freshly fabricated cells. The PV properties of the cells are provided in Table 5.1, where each number represents an average value of the property measured from six cells in each group. As shown in **Figure 5.2.a**, the very similar  $J$ - $V$  characteristics of devices with the ZnO to those with the ZnO/PDIN-H EEL show that adding a PDIN-H layer on top of the ZnO EEL does not have a significant impact on the initial PV parameters of the device. We also compared the EELs in EODs of the structure ITO/EEL/PC60BM/LiF/Al. **Figure 5.2.b** shows the  $J$ - $V$  characteristics of the EODs collected in the dark with the bias direction such that the Al is held at a more negative potential with respect to ITO. Under this bias direction, electrons are injected from the Al/LiF contact and are collected at the ITO electrode, and therefore are transported across the EELs in the same direction as in the studied OSCs. As can be seen, the use of the PDIN-H does not impede electron collection, consistent with the above observations from the OSCs.

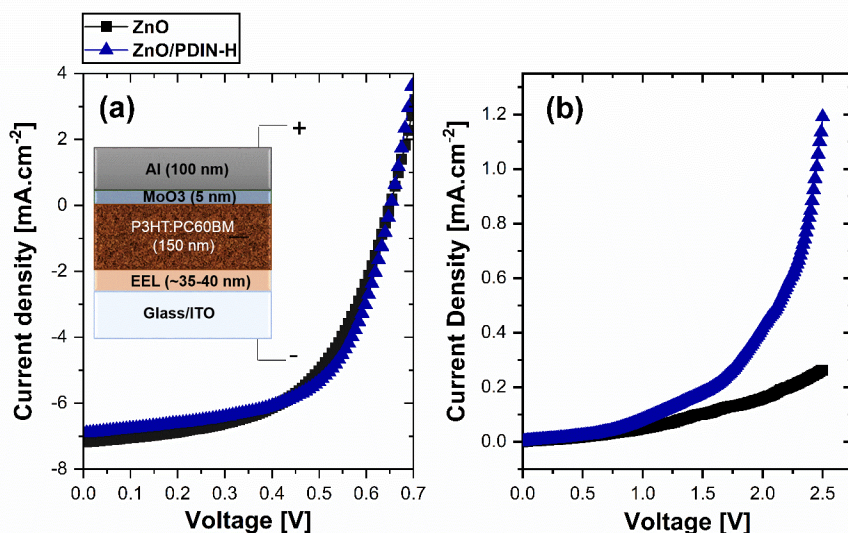


**Figure 5. 2.** (a)  $J$ - $V$  characteristics of the studied OSCs with the ZnO (black squares) and ZnO/PDIN-H (blue triangles) EELs, measured under 1-sun AM1.5G illumination. The inset shows the schematic depiction of the architecture of the studied OSCs. (b)  $J$ - $V$  characteristics of electron-only devices with the two studied EELs.

For the photostability tests, one OSC set was continuously exposed to an  $8 \text{ mW.cm}^{-2}$  illumination from a 365 nm UV lamp for 780 h. On the same substrate, another set of cells was kept in the dark to be used as a control set. The illuminated  $J$ - $V$  characteristics of all OSCs were measured at successive time intervals. The PV properties, normalized to their initial value (that of the fresh cells), for the UV-irradiated cells are provided in **Figure 5.3**. As can be seen from **Figure 5.3**, after 780 h of UV irradiation, the OSCs with the ZnO EEL exhibit a significant decrease in their  $V_{oc}$  ( $\sim 32\%$ ), FF ( $\sim 34\%$ ), and, as a result, their PCE ( $\sim 64\%$ ), whereas the cells with the ZnO/PDIN-H EEL show only a modest decrease in their  $V_{oc}$  ( $\sim 6\%$ ), FF ( $\sim 8\%$ ), and PCE ( $\sim 15\%$ ). The magnitude of  $V_{oc}$  and FF losses in the cells with ZnO is consistent with earlier reports [55, 85, 86]. Overall, using the ZnO/PDIN-H EEL instead of the ZnO EEL reduces photodegradation, leading to a respective  $T_{80}$  of more than 780 h instead of only 124 h, where  $T_{80}$  is the time taken for the PCE to decrease to 80% of its initial value. For both devices, losses in  $J_{sc}$  over time were significantly smaller than the  $V_{oc}$  and FF losses (only  $\sim 12\%$  and  $\sim 2\%$  in the cells with ZnO and ZnO/PDIN-H, respectively). It is worth noting that during the first 120 h of UV irradiation, the  $J_{sc}$  and  $V_{oc}$  decay trends of the cells with ZnO were comparable (the

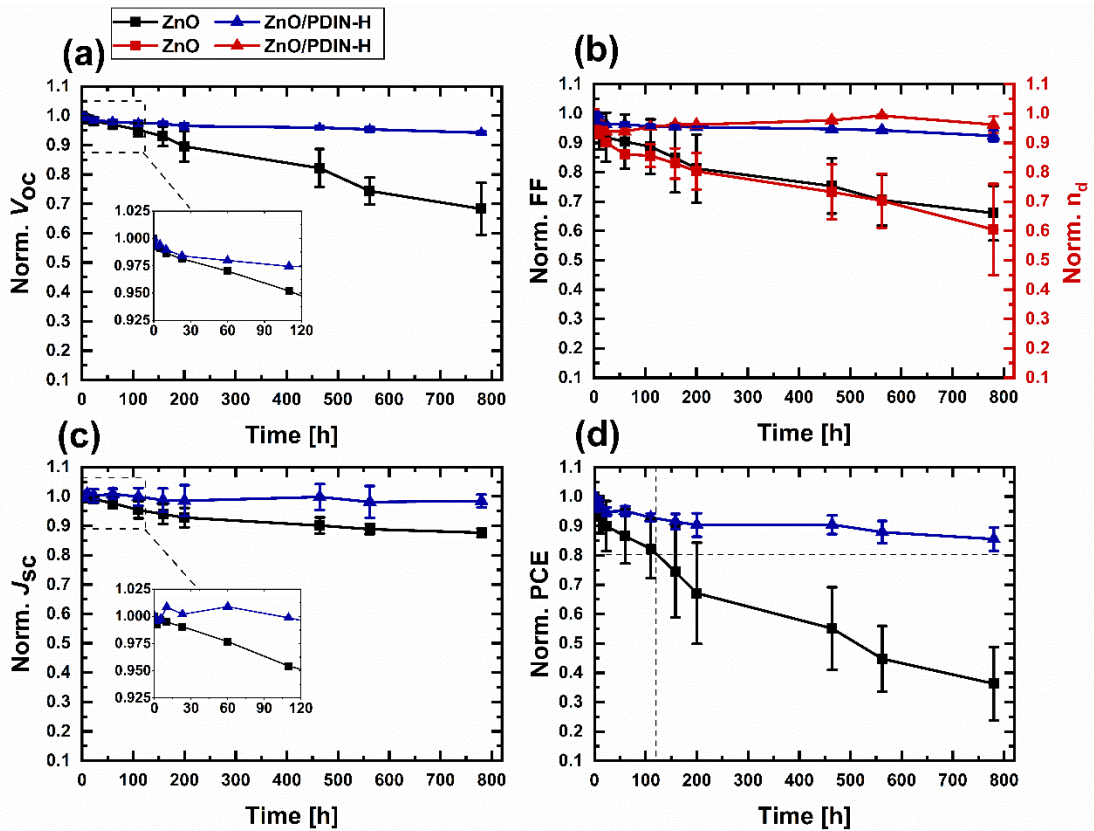


**Figure 5. 3.** Normalized  $V_{oc}$  (a), FF (b),  $J_{sc}$  (c), and PCE (d) versus different time intervals of UV irradiation of OSCs with the ZnO (black squares) and ZnO/PDIN-H (blue triangles) EELs. Insets in (a) and (c) magnifies their trends in the 0-120 h time range. The right axis in (b) represents the normalized ideality factor of the cells versus the aging time extracted from their dark  $J$ - $V$  curves, in the voltage range of 0.4-0.6 V. The sign of the ideality factors is flipped, and the curves are shifted to start from 1. The dotted lines in (d) indicate  $T_{80}$ , where the PCE decreases to 80 % of its initial value. The error bars represent the standard deviation of each measurement.

insets in **Figure 5.3.a** and **5.3.c**, respectively). However, over the 120 - 780 h irradiation timeframe, the  $V_{oc}$  trend shows a steep decay, whereas the  $J_{sc}$  decay trend slows down over time. This observation will be addressed later.

To differentiate between losses in PV performance that were caused primarily by the UV illumination from those that may have occurred simply due to changes in the materials over time without them being driven by the UV stress, we compared the changes in the PV parameters of the UV-irradiated devices to control devices, shown in **Figure 5.4.a** (for ZnO cells), and **5.4.b** (for ZnO/PDIN-H cells). Clearly, much smaller changes in the PV parameters are observed in the control cells in comparison, verifying that the UV stress is the primary source of the observed degradation in **Figure 5.3**.

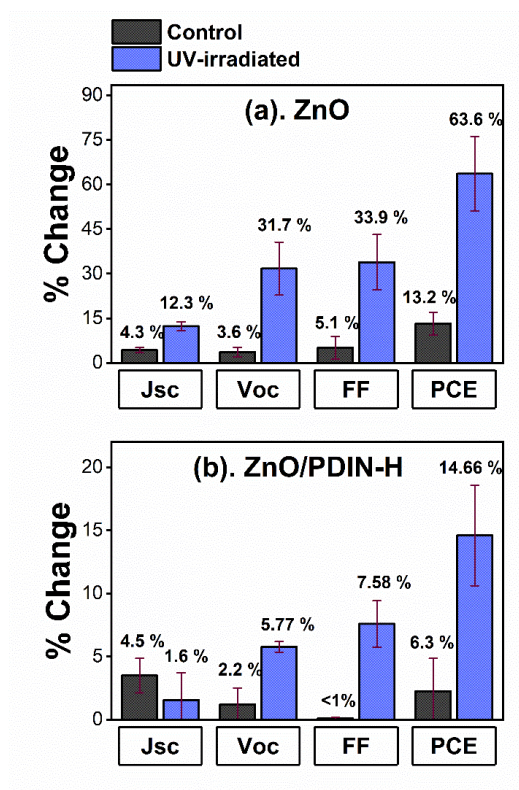


**Figure 5. 4.** % change in PV parameters of OSCs with the ZnO (a) and ZnO/PDIN-H (b) EELs after UV illumination for 780 h and of a control set of identical OSCs that was kept in the dark (i.e., no UV) for the same period. Error bars represent the standard deviation in each measurement.

To investigate the causes of the higher photostability in the devices with the PDIN-H layer, we first investigated if the phenomenon might be associated with morphological effects in the BHJ layer, imparted by the presence of the underlying PDIN-H layer. Thus, we compared their optical absorption characteristics. As shown in **Figure 5.5**, the presence of the PDIN-H layer brings about some increase in PC60BM absorption (300 nm-400 nm) along with a decrease in P3HT absorption (450 nm-650 nm). This observation suggests that the PDIN-H layer may be influencing the molecular orientation of PC60BM and P3HT molecules in BHJ (leading to molecular orientations with stronger (weaker) coupling between molecular dipole moment of PC60BM (P3HT) and the electric field of the incoming photon). More notably, however, the spectra remain almost unchanged after 200 h of UV irradiation regardless of the EEL choice. This observation indicates that while the presence of the PDIN-H may somewhat alter the initial morphology of the BHJ layer, its role in enhancing OSC photostability is not primarily due to the suppression of any UV-induced morphological changes in the BHJ over time.



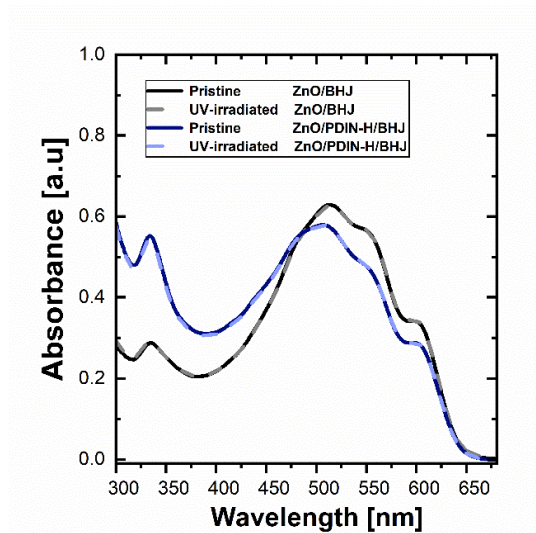


**Figure 5. 5.** UV-Vis absorption spectra of pristine (solid lines) and 200 h UV-irradiated (dotted lines) P3HT:PC60BM coated on ZnO (black) and ZnO/PDIN-H (blue).

Next, we studied and compared changes in the cells' dark  $J$ - $V$  characteristics due to UV stress. The dark  $J$ - $V$  curves of the fresh and UV-irradiated cells are presented in **Figure 5.6.a** (for the ZnO cells) and **5.6.b** (for the ZnO/PDIN-H cells) on a semilogarithmic scale. As shown, the reverse current of the cells with ZnO decreases slightly during the first 8 h of UV stress, followed by a noticeable increase thereafter. Unlike in the cells with ZnO, the reverse current does not increase in the cells with ZnO/PDIN-H during the whole UV exposure. Because under reverse voltage, the ITO is held at a more positive potential relative to the Al electrode, an increase in the current reflects an increase in either hole injection through the ITO/EEL contact or electron injection through the MoO<sub>3</sub>/Al contact. Since apart from the EELs, the OSCs are structurally identical, the difference in reverse current must be associated with the EELs and arises from increased hole injection over time in the ZnO EEL case, pointing to a deterioration in the hole-blocking nature of the ITO/EEL contact. Consequently, the findings illustrate that the ability of the ITO/ZnO contact to block hole injection diminishes upon prolonged UV illumination, whereas that of the ZnO/PDIN-H contact remains relatively unchanged. Since selectivity losses are known to cause a  $V_{oc}$  reduction [105, 155], the observed higher  $V_{oc}$  photostability in the cells with ZnO/PDIN-H may then be ascribed to the ability of this contact to suppress the UV-induced selectivity loss that occurs in the cells with ZnO.

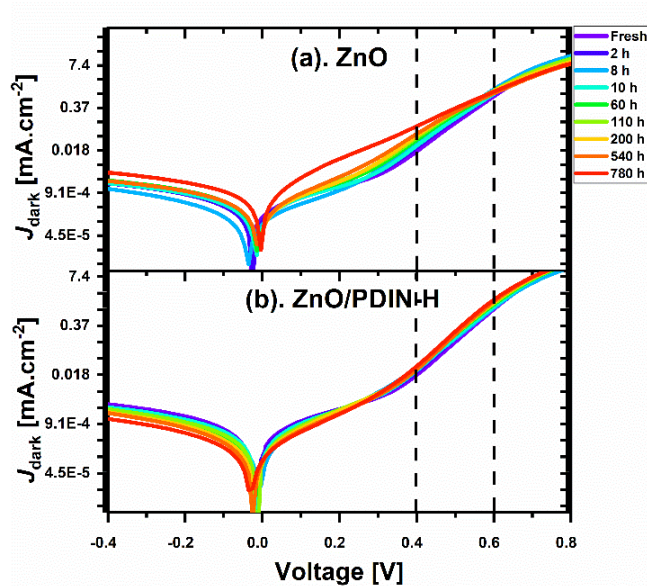


**Figure 5. 6.** Dark  $J$ - $V$  characteristics of fresh and after different time intervals of UV irradiation of OSCs with ZnO (a) and ZnO/PDIN-H (b), on a semilogarithmic scale. The dotted vertical guides point to the voltage range from which the cells' dark ideality factors were extracted.

The difference in the UV-induced FF deterioration between the cells with the two different EELs hints at differences in electron-hole recombination mechanisms/rates. To glean some insights into recombination differences, we extracted the dark ideality factors ( $n_d$ ) of the OSCs from the slope of the dark  $J$ - $V$  characteristics in the 0.4-0.60 V voltage range (shown by dotted vertical guides in **Figure 5.6**). This voltage range was selected because the ideality factor over this range is negligibly affected by the series or shunt resistance, as can be inferred from the weak voltage dependency of ideality factor characteristics (evident from the flat parts of the curves in **Figure 5.9**). Initially, the ideality factors of the fresh cells were not too dissimilar: 1.89 and 1.82 for the cells with ZnO and with ZnO/PDIN-H, respectively. However, after 780 h of UV irradiation, the ideality factor of the cells with ZnO increases, whereas that of the cells with ZnO/PDIN-H EEL remains almost unchanged. This finding suggests different recombination mechanisms/rates in the cells with the two EELs.

The evolution of normalized  $n_d$  against different aging time intervals of the OSCs is presented in **Figure 5.3.b**, on the right axis. The sign of the ideality factors is flipped, and the curves are shifted to start from 1. This modification makes the visual comparison between the degradation of ideality factors and PV properties more straightforward. As evident, the ideality factor initially exhibits a sharp change for both cells, whereas FF and  $V_{oc}$  do not change significantly during the first 120 h of UV illumination.

Then, from 120 h to 780 h of UV exposure, the changes of  $n_d$  qualitatively follow FF and  $V_{oc}$  trends for both cells. In the cells with ZnO, this qualitative match along with the increase in dark reverse current suggests that a combination of two interrelated phenomena, the reduction in the contact selectivity through shunting and changes in recombination mechanisms/rates, account for a significant part of photodegradation in these cells, consistent with a report by Trost et al. [110]. In contrast, the stable trend of the ideality factor along with the low reverse current of the OSCs with ZnO/PDIN-H demonstrates that these cells maintain their rectifying behavior and recombination mechanism/rate upon prolonged irradiation.

Selectivity loss of contacts has been reported to be interrelated with shunt formation in OSCs and thus with FF deterioration [110, 143]. To test for this phenomenon, we extracted the shunt resistance values of the fresh and UV-irradiated cells (the inverse slope of the illuminated  $J$ - $V$  curves near the  $J_{sc}$ ). Results (**Figure 5.7.a**) show that shunt resistance decreased by almost 73 % (from 829  $\Omega\cdot\text{cm}^2$  to 225  $\Omega\cdot\text{cm}^2$ ) in the ZnO cells, versus only around 30 % (from 784  $\Omega\cdot\text{cm}^2$  to 545  $\Omega\cdot\text{cm}^2$ ) in the ZnO/PDIN-H cells, after UV irradiation. Clearly, the results illustrate a substantial photoinduced shunt formation in the ZnO cells, and that the PDIN-H layer helps suppress this phenomenon to some extent. To determine whether the observed UV-induced deterioration of FF and  $n_d$  originates only from shunting and increased recombination, or if ohmic losses also play a role in this regard, we also investigated the changes in the series resistance upon UV irradiation. Series resistance values can be obtained from the slope of the linear fits of  $J \cdot dV/dJ$  against  $J$ , derived from the dark  $J$ - $V$  characteristics under forward bias [156]. **Figure 5.7.b** depicts only a slight linear increase of  $R_s$  after UV exposure, ranging from 5.9  $\Omega\cdot\text{cm}^2$  (fresh device) to 6.1  $\Omega\cdot\text{cm}^2$  (UV-irradiated device) for the cells with ZnO, and from 4.9  $\Omega\cdot\text{cm}^2$  to 5.3  $\Omega\cdot\text{cm}^2$  for the devices with ZnO/PDIN-H. Given the small differences between the two cases, one can conclude that the different ideality factor and FF photodegradation among the cells is unlikely to be ascribed to any significant ohmic losses and could therefore be attributed mainly to shunting loss.

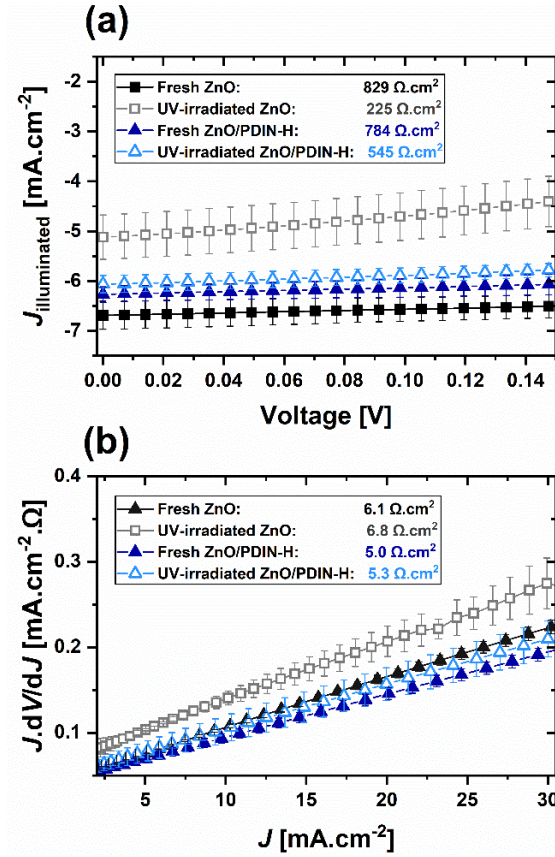


**Figure 5. 7.** Illuminated  $J$ - $V$  (a) and  $J \cdot dV/dJ$  against  $J$  of the dark  $J$ - $V$  characteristics under forward bias (b) of fresh (filled symbols) and 780 h UV-irradiated (open symbols) cells with the ZnO (black/grey squares) and ZnO/PDIN-H (blue triangles) EELs. The shunt and series resistance values extracted from the slope of the curves are written inside each figure. Error bars indicate the standard deviation of each measurement.

A dark ideality factor with a larger than unity value for BHJ solar cells is often taken as an indicator of the presence of a dominant trap-assisted recombination process [126, 157]. Wetzelaer et al. [124] however demonstrated that such values could be obtained even without trap-assisted recombination, making it difficult to make reliable conclusions about the presence or absence of specific recombination processes based on the dark ideality factor alone. An additional limitation is the limited charge carrier mobility in OSCs, which can also impact the ideality factor and, therefore, makes it difficult to attribute the changes in the dark ideality factor to the contact resistances versus recombination [126]. With these limitations in mind, we tested for UV-induced changes in charge recombination mechanisms/rates by measuring the light intensity dependence of  $J_{\text{sc}}$ , FF, and  $V_{\text{oc}}$  for both cells before and after aging. The dependence of  $J_{\text{sc}}$  on light intensity is given by  $J_{\text{sc}} \propto (\text{Light-Intensity})^\alpha$ , where alpha ( $\alpha$ ) is the slope of the  $J_{\text{sc}}$  versus light intensity curve on a log-log scale. As discussed in chapter 3,  $\alpha$  gives some insights

into dominant recombination mechanisms. Results from **Figure 5.8.a** depict that both the ZnO and ZnO/PDIN-H cells exhibit  $\alpha \sim 1$ , before and after UV irradiation, demonstrating that bimolecular recombination is negligible. This observation supports the small aging tendency of  $J_{sc}$  of both cells (**Figure 5.3.c**).

**Figure 5.8.b** provides the FF versus light intensity curves of the fresh and 780 h UV-irradiated solar cells with the two EELs. For both fresh cells, the FF slightly increases as the light intensity is increased from 20  $\text{mW}\cdot\text{cm}^{-2}$  to 40  $\text{mW}\cdot\text{cm}^{-2}$ . After that, with an increase in light intensity from 40  $\text{mW}\cdot\text{cm}^{-2}$  to 100.5  $\text{mW}\cdot\text{cm}^{-2}$ , the FF slightly decreases in the cells with ZnO, whereas it remains almost unchanged in the cells with ZnO/PDIN-H. The observed trend in the fresh cells with ZnO suggests a competition between charge accumulation at low light intensities and charge recombination at high light intensities. As the intensity of light increases, the number of photogenerated carriers increases, and consequently, the percentage of transported carriers increases, thereby increasing the FF [158, 159]. That is because with the increased light intensity, the number of photogenerated carriers will increase, and a significant percentage of the traps become filled, subsequently making transport easier hence the increase in FF. With a further increase in the light intensity, with most of the traps already filled, the number of transported carriers will continue to increase, eventually leading to increased bimolecular recombination. As a result, the percentage of transported carriers relative to the total photogenerated carriers starts to decrease, leading to the subsequent decrease in FF, in agreement with the literature [158]. It is worth noting that since bimolecular recombination is generally relatively limited in the cells (based on data from **Figure 5.8.a**), the decrease in FF in the light intensity range of 40  $\text{mW}\cdot\text{cm}^{-2}$  to 100.5  $\text{mW}\cdot\text{cm}^{-2}$  is small. Regardless of the EELs, in the fresh cells, charge accumulation in the bulk layer dominates at low light intensities ( $< 40 \text{ mW}\cdot\text{cm}^{-2}$ ), whereas charge recombination does so at high intensities ( $> 40 \text{ mW}\cdot\text{cm}^{-2}$ ). This trend is expected as the number of traps is generally limited. Therefore, charge accumulation in the bulk layer can occur only at a low light intensity. In contrast, at high intensities, the traps are quickly filled. Thus, the carriers are no longer affected by the traps [158, 160]. This fact explains the observation from **Figure 5.3.c** that the  $J_{sc}$  of the cells with ZnO decays during the first 120 h of aging and then stabilizes.

Moving to the UV-irradiated cells, one can see that the FF decreases monotonically on increasing the light intensity in the case of the ZnO devices. Earlier studies have demonstrated that such a monotonic decrease in FF is associated with charge accumulation at the electrode/active-layer interface and is different from the charge accumulation/recombination in the bulk traps [158]. The trend,

therefore, points to increased accumulation at the ZnO/active-layer interface in the UV-irradiated cells relative to the fresh cells. As discussed earlier, if the FF losses originate from charge losses in bulk, one can expect a non-monotonic FF trend as increasing the light intensity. Accordingly, the monotonic decay trend of FF after UV irradiation indicates that the FF losses resulting from charge accumulation in bulk become trivial and do not occur even at a very low light intensity of  $20 \text{ mW.cm}^{-2}$ .

In contrast to ZnO devices, the UV-irradiated devices with ZnO/PDIN-H show FF vs. light-intensity dependence comparable to that of their fresh cells. There is only a relatively small increase in the negative slope of the trend above the intensity of  $70 \text{ mW.cm}^{-2}$ . These results reveal that the OSCs with ZnO experience a UV-induced transition in the main FF loss mechanism from trap-assisted recombination in the bulk to charge accumulation at the ZnO/active-layer interface. However, the cells with ZnO/PDIN-H avoid this UV-induced transition to a large extent and therefore prevent a similar deterioration in efficiency and hence exhibit a higher photostability.

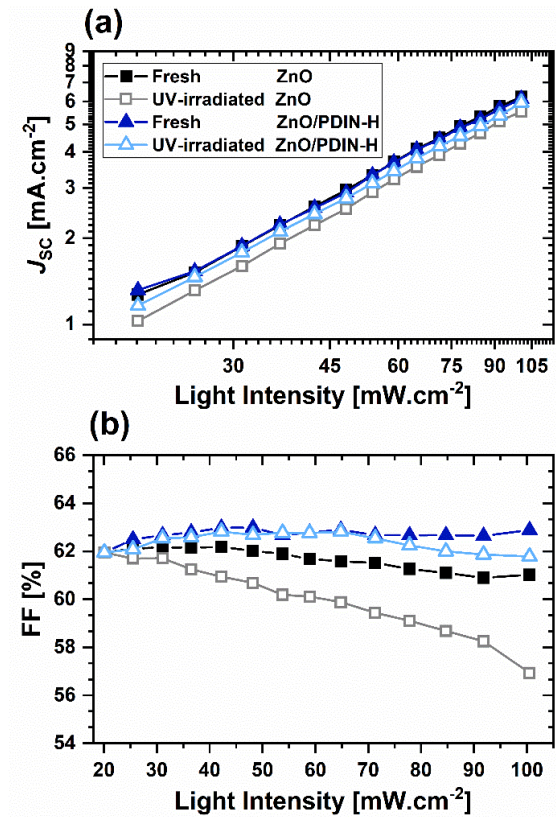


**Figure 5. 8.**  $J_{sc}$  (a) and FF (b) vs. light intensity of the fresh (filled symbols) and 780 h UV-irradiated (open symbols) cells with the ZnO (black/grey squares) and ZnO/PDIN-H (blue triangles) EELs.

So far, the results from light intensity dependence of PV properties and the dark ideality factor point to changes in recombination mechanisms in the ZnO cells. However, due to the inherent complexities mentioned earlier in the BHJ systems, more accurate interpretation of OSCs' ideality factor values can be achieved only if their voltage dependence characteristics in both light and dark conditions are considered and explained in the context of the other results [126]. Thus, to obtain further insights into the differences between the ZnO/PDIN-H and the ZnO OSCs and any changes in their charge recombination mechanism under the UV stress, we also examine the voltage dependence of both the dark and light ideality factors in the fresh and UV-irradiated cells. The light ideality factor ( $n_l$ ) is extracted from the light intensity dependence of  $V_{oc}$  using:  $n_l = q/KT * [dV_{oc}/d \ln(\phi)]$ , where  $q$  is the elementary charge,  $K$  is the Boltzmann's constant,  $T$  is temperature, and  $\phi$  is light intensity. Unlike in the case of the "dark" ideality factor, series resistance effects are eliminated in the case of the "light" ideality factor since the latter is obtained from measurements at an open-circuit voltage where no current is flowing [126]. The results are presented in **Figure 5.9**.

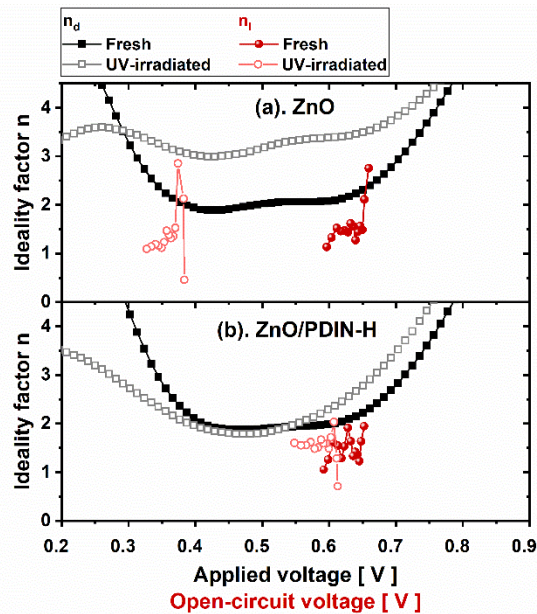


**Figure 5. 9.** Ideality factors as a function of the voltage of the fresh (filled symbols) and 780 h UV-irradiated (open symbols) cells with the (a) ZnO and (b) ZnO/PDIN-H EELs. The black/grey squares represent the dark ideality factors ( $n_d$ ) derived from the dark  $J$ - $V$  characteristics. The red circles represent the light ideality factors ( $n_l$ ) from the open-circuit voltage's light-intensity-dependent characteristics.

As was noted earlier, for the fresh OSCs in both cases,  $n_d$  remains almost constant in the voltage range of 0.4-0.6 V but increases substantially at lower and higher voltages under the impact of shunt and series resistances. Also initially, for both cells,  $n_1 > 1$  in most voltage ranges. After the UV stress, the value of  $n_d$  over the whole 0.4-0.6 V voltage range increases in the ZnO sample, and the light ideality factor is shifted downwards on the voltage axis. Additionally, in the cells with ZnO, the  $n_1$  values fall sharply to below one at voltages higher than 0.38 V. It has been reported that  $n_1$  values smaller than one at high voltages point to the occurrence of surface recombination at the electrodes [126, 161]. Considering these results and the conclusion made earlier based on the light-intensity dependence of FF (**Figure 5.8.b**), it can be concluded that the UV-induced charge accumulation at the ZnO/active-layer interface leads to surface recombination at this interface. Therefore, a transition from bulk trap-assisted recombination to surface recombination at the electrode occurs under the UV stress in the ZnO cells. In contrast, in the ZnO/PDIN-H cells,  $n_d$  remains almost unaffected in the 0.4-0.6 V voltage range,  $n_1$  shows a small shift to lower  $V_{oc}$  ranges and decreases gradually to below unity at high voltages. The voltage-dependent depiction of the  $n_1$  in the cells with ZnO/PDIN-H, however, exhibits a decaying trend with a remarkably smaller slope compared to that of the cells with ZnO, suggesting surface recombination is (and remains) insignificant. Since the two types of devices are architecturally similar except for their EELs, it can be concluded that the increased surface recombination that happens in the ZnO cells must be happening at the electron extraction contact and that adding a neat layer of PDIN-H in between the BHJ and the ZnO layers helps suppress this behavior to a significant extent.

In view of these findings, to understand the effect of PDIN-H on the ZnO surface, we performed UPS measurements to investigate the electronic characteristics of ZnO and ZnO/PDIN-H surfaces. The measurement was conducted in an ultra-high vacuum that eliminates any possible alteration of surface properties due to contamination. A bias of -5 V was applied so that the inelastic cutoff of the sample and spectrometer could be distinguished. The work functions ( $\phi$ ) of the ITO/ZnO and ITO/ZnO/PDIN-H samples were calculated from the secondary electron cutoff ( $E_{cutoff}$ ) and the Fermi energy ( $E_F$ ) of the UPS spectra, using  $\phi = \hbar\nu - (E_{cutoff} - E_F)$ , where  $\hbar\nu = 21.22$  eV is the incoming photon energy from the He I source. **Figure 5.10.a** displays the UPS spectra of the ITO/ZnO and ITO/ZnO/PDIN-H samples, whereas **Figure 5.10.b** represents the enlarged binding energy in the cutoff and Fermi regions. For the ZnO sample, the calculated work function is 4.46 eV, in accordance with the reported value [110]. Adding a neat layer of PDIN-H causes an upward shift in the secondary cutoff binding energies, inducing a decrease in the work function (3.89 eV). This 0.57 eV reduction in the ZnO work function upon adding PDIN-H points to the passivation of ZnO surface defects by PDIN-H. In addition, ZnO



exhibits a gradual slope in the cut-off region ( $E_{\text{cutoff}}$  of 17.07 to 18.5 eV), which points to an inhomogeneous or “patchy” surface [40]. In contrast, ZnO/PDIN-H exhibits a much sharper slope in the cut-off region, which indicates a more homogenous surface, further affirming the passivation effect of PDIN-H.

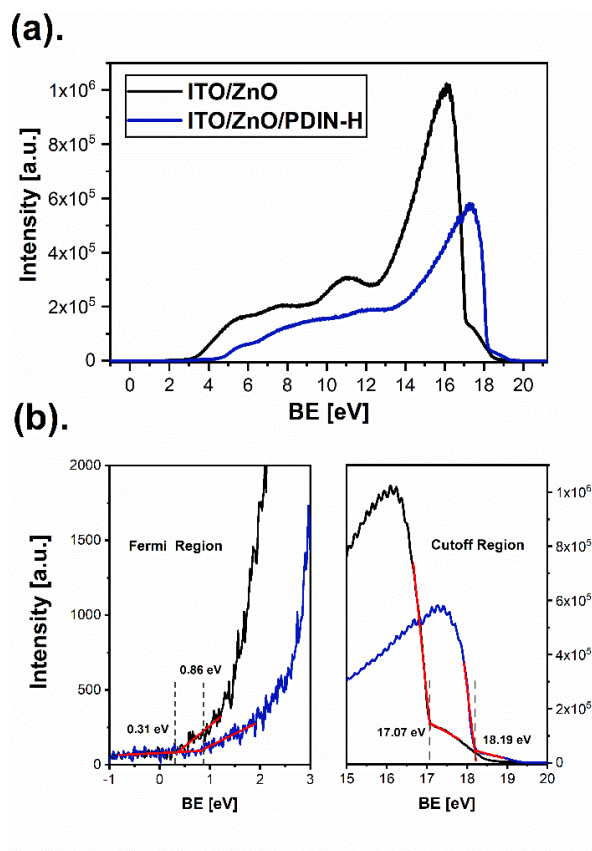


**Figure 5. 10.** (a). UPS spectra of ITO/ZnO (black) and ITO/ZnO/PDIN-H (blue). (b). Secondary-electron cutoff regions and Fermi-edge regions. Work functions of ITO/ZnO and ITO/ZnO/PDIN-H are calculated as 4.46 eV and 3.89 eV, respectively.

### 5.3 Conclusion

In summary, results reveal that adding PDIN-H atop the commonly used ZnO EEL improves OSCs' photostability, mainly by providing a more stable  $V_{\text{oc}}$  and FF. Dark  $J$ - $V$  characteristics at reverse voltages illustrate that this higher  $V_{\text{oc}}$  stability primarily originates from the potential of the ITO/ZnO/PDIN-H contact to maintain a higher degree of hole-blocking functionality under UV

illumination in comparison to the ITO/ZnO contact. Comparing the data from the voltage dependence of dark and light ideality factors and the FF dependence on light intensity indicates that the OSCs with ZnO encounter a UV-induced transition in a dominant recombination mechanism from trap-assisted recombination in bulk to the surface recombination at the ZnO/active-layer interface. On the other hand, using ZnO/PDIN-H avoids this UV-induced transition to a huge extent, thereby boosting the cell's photostability. This UPS measurements data verifies that the passivation of ZnO surface defects upon adding PDIN-H hinders this undesirable recombination. The results, therefore, provide new and vital insights into the root causes of degradation in OSCs under solar irradiation and interfacial engineering strategies to mitigate them.

## Chapter 6

### The Influence of Replacing ZnO with Polyethyleneimine as a Large Dipole Moment EEL on the Intrinsic Photostability of OSCs

*This work has been published in Sadeghianlemraski, M., and Aziz, H., Solar Energy, vol. 198, pp. 427-433, 2020. It has been reproduced with minor changes with permission from the publisher.*

#### 6.1 Introduction

As established in Chapter 4 and 5, solar cells with ZnO tend to suffer from low photostability, which appears as a rapid decrease in PCE under illumination. In previous chapters, we demonstrated that modifying ZnO with PEI (as a mixture or bilayer) and with PDIN-H (as a bilayer) can enhance OSC photostability, attributable to the formation of an electronically more stable contact. Aside from the modification of ZnO, replacing it with SnO<sub>x</sub> [110] or fullerene-based materials [106] increased photostability remarkably, but the higher toxicity or the need for halogenated solvents reduce the viability of these alternatives [107]. Therefore, there is still a need to develop EELs that can provide and maintain electron selectivity even after prolonged irradiation and that can be easily processed using green solvents [108].

In this context, using materials with large dipole moments as EELs can provide a viable alternative [39, 47, 97, 111, 112]. The large dipole moment leads to a shift in the vacuum Fermi level [114, 115] and results in a more efficient carrier-selective contact [116] as well as enables solution processability in polar green solvents [113]. In a review on interfacial dipoles utilized in organic and perovskite solar cells, Chen et al. [39] concluded that using these materials as interlayers at contacts can help realize high efficiency, nontoxicity, and thickness-insensitivity features for large-scale commercialization.

Among polymers with large dipole moments, PEI [97, 112] is now one of the most commonly used EELs [123] and is shown to provide superior initial charge selectivity. However, little is still known about their ability to maintain this selectivity over time and under UV stress. In this work, we investigate the effect of using PEI alone as the EEL, without ZnO, on the photostability of OSCs. Cells with PEI EELs are found to exhibit significantly higher photostability relative to those with ZnO EELs. We investigate the origins of the photostability enhancement. Analysis of *J-V* characteristics of the solar

cells shows that the higher  $V_{oc}$  stability attained upon using PEI instead of ZnO as an EEL is mainly due to the ability of the ITO/PEI contact to maintain a higher degree of electron selectivity and hole blocking properties under UV exposure in comparison to the ITO/ZnO contact. Hole-only devices are used to compare the hole-blocking functionality of the ITO/ZnO and ITO/PEI as electron collection contacts. Light-intensity dependence of  $V_{oc}$  and  $J_{sc}$  analysis are then used to help us distinguish between dominant recombination processes.

## 6.2 Results and Discussion

The effect of using PEI instead of ZnO as an EEL on OSC photostability is studied and compared. In order to ensure that the observations are not unique to a specific OSC material system, bulk heterojunction OSCs based on two different material systems, P3HT:PC60BM and PCDTBT:PC70BM are used in the study. **Figure 6.1** shows the structures of the OSCs used in this work: (a). ITO/ZnO (35nm) or PEI (~5nm)/P3HT:PC60BM/MoO<sub>3</sub>/Al, and (b). ITO/ZnO (35nm) or PEI (~5nm)/PCDTBT:PC70BM/MoO<sub>3</sub>/Al. All devices were fabricated and tested under the same conditions. The PV parameters of these cells under 1 sun 1.5 AM radiation are provided in Table 6.1. Generally, using PEI instead of ZnO does not significantly alter the PV parameters of the OSCs, evident from their comparable efficiencies; 3.09 %, versus 3.35 % for devices with ZnO and PEI EELs, respectively, in the P3HT:PC60BM-based OSCs, and 5.21 %, versus 5.27 %, respectively, in their PCDTBT:PC70BM-based counterparts. The cells with PEI show somewhat higher  $J_{sc}$  exhibiting  $J_{sc}$  of 9.51 mA.cm<sup>-2</sup> and 11.19 mA.cm<sup>-2</sup> compared to  $J_{sc}$  of 9.18 mA.cm<sup>-2</sup> and 11.04 mA.cm<sup>-2</sup> in cells with ZnO for P3HT:PC60BM and PCDTBT:PC70BM devices, respectively. Additionally, slightly higher  $V_{oc}$  of 0.64 V and 0.89 V is observed in cells with PEI versus  $V_{oc}$  of 0.61 V and 0.88 V in the cells with ZnO for P3HT:PC60BM and PCDTBT:PC70BM devices, respectively. This slight increase in  $V_{oc}$  upon using PEI instead of ZnO as EELs has been shown to be due to the dipole effect of PEI on ITO WF [129] and is consistent with our previous observations.

**Table 6. 1.** PV parameters of P3HT:PC60BM-based and PCDTBT:PC70BM-based OSCs with the ZnO and PEI EELs.

BHJ Material System	EEL	PV Parameters			
		$J_{sc}$ [ $\text{mA}\cdot\text{cm}^{-2}$ ]	$V_{oc}$ [V]	FF [%]	PCE [%]
P3HT:PC60BM	ZnO	9.18	0.61	55.62	3.09
	PEI	9.51	0.64	54.85	3.35
PCDTBT:PC70BM	ZnO	11.04	0.88	53.90	5.21
	PEI	11.19	0.89	52.72	5.27

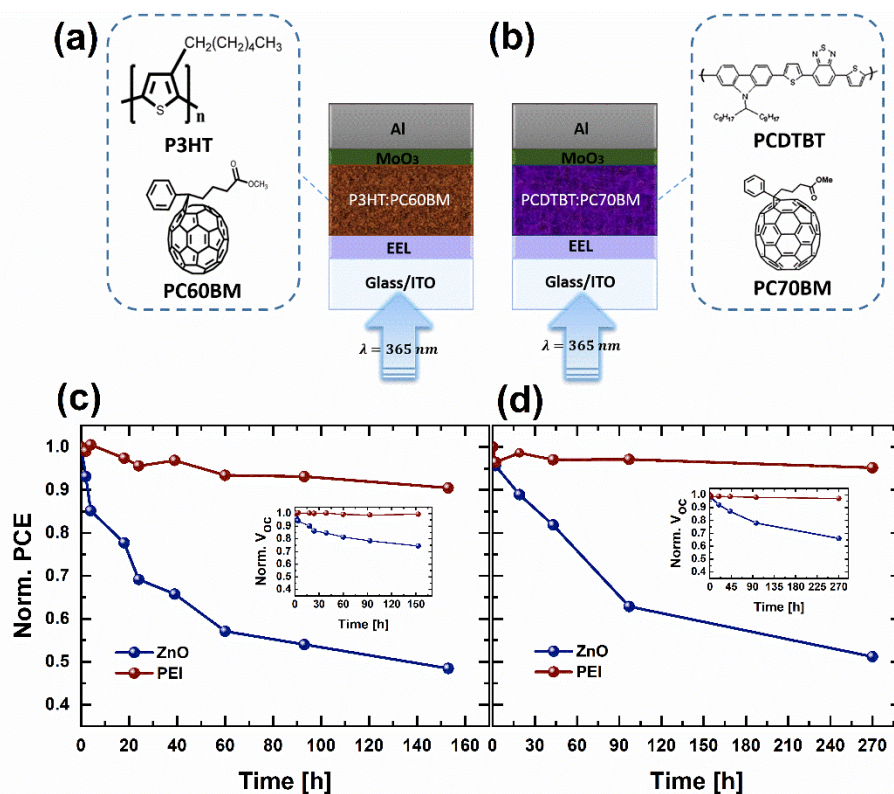


**Figure 6. 1.** Schematic depictions of the structure of the P3HT:PC60BM-based BHJ OSCs (a) and PCDTBT:PC70BM-based BHJ OSCs, with the molecular structures of the materials used in the BHJ active layer in each case. ZnO or PEI is used as EELs in each case. Normalized PCE versus time under continuous UV illumination of OSCs with the ZnO and PEI EELs: (c) P3HT:PC60BM BHJ system; (d) PCDTBT:PC70BM BHJ system. Insets show the normalized  $V_{oc}$  versus time.

Then for photostability study, the cells were exposed to continuous UV illumination at a power density of  $8 \text{ mW.cm}^{-2}$  and a wavelength of 365 nm. The  $J$ - $V$  characteristics (both dark and illuminated) of the OSCs were collected before irradiation and at different time intervals thereafter. The normalized PCEs, at these time intervals, are provided in **Figure 6.1.c** and **6.1.d** for the P3HT:PC60BM-based cells and the PCDTBT:PC70BM-based cells, respectively, with the normalized  $V_{oc}$  vs. time trends shown in the insets. Normalized  $J_{sc}$  and FF vs. time trends are provided in **Figure S6.1**. As can be seen from **Figure 6.1**, prolonged UV exposure caused a significant decrease in the PCE of OSCs with ZnO EELs, whereas the OSCs with PEI EELs were significantly more stable. The OSCs with the PEI EELs exhibited a decrease in PCE of only about 10%, and 4% after 153 h of UV irradiation in the P3HT:PC60BM and PCDTBT:PC70BM BHJ systems, respectively;  $\sim 5x$  and  $10x$  smaller than that observed in their counterparts with the ZnO EELs. Also notably, although the EEL choice significantly affected the  $V_{oc}$  loss, it had a negligible effect on  $J_{sc}$  loss. This significant photo-induced  $V_{oc}$  loss over time in solar cells with ZnO is consistent with other reports [55, 69, 85, 86].

To investigate the origins of the photostability enhancement observed upon replacing ZnO by PEI, we also studied changes in dark  $J$ - $V$  characteristics of the cells due to the UV illumination at the same time intervals. The dark  $J$ - $V$  characteristics of the fresh (filled circles) and after different time intervals of UV exposure (open circles) of the P3HT:PC60BM cells with ZnO and PEI EELs are provided in **Figure 6.2.a** and **b**, and of the PCDTBT:PC70BM cells in **Figure 6.2.c** and **d** (The characteristics are shown in linear (**Figure 6.2.a & c**) and semi-logarithmic (**Figure 6.2.b & d**) scales). From the linear plots, one can see that the current at reverse bias voltages progressively increases with UV exposure time in OSCs with ZnO EELs, whereas it remains relatively unchanged (stays close to zero) in their counterparts with the PEI EELs. Under dark conditions, any measured current will predominantly be due to the injection of carriers from the contacts into the active layers under the influence of the applied bias. Since, at reverse voltage, the ITO contact is held at a more positive potential relative to the Al electrode and ZnO and PEI are expected to block hole injection, whereas the  $\text{MoO}_3/\text{Al}$  contact effectively blocks electron injection in this device configuration, the reverse dark current is expected to be negligible. This finding explains the small reverse dark current demonstrated by the fresh cells. The observed gradual increase in reverse current in the cells with ZnO with UV illumination suggests that either hole injection from the ITO/ZnO contact or electron injection from the  $\text{MoO}_3/\text{Al}$  contact increases over time. Since no similar increase is observed in the cells with the PEI EELs whereas the electron blocking contacts are the same in both cases (always  $\text{MoO}_3/\text{Al}$ ), differences in reverse currents among the cells must then be associated with increased hole injection from ITO/ZnO contact. This

observation suggests that the ability of ZnO to block hole transport diminishes over time under the influence of UV exposure. Based on the Shockley equation [69, 105], the decrease in  $V_{oc}$  may then be due to the increase in dark reverse current.

At forward bias, ITO is held at a more negative potential relative to the Al electrode. Therefore, in this case, electrons are injected from ITO/ZnO or ITO/PEI contacts and holes from the MoO<sub>3</sub>/Al contacts into the active layer. At voltages above the injection threshold (above  $\sim + 0.5$  V), the  $J$ - $V$  characteristics of the UV-aged ZnO cells show a substantially weaker diode behavior after UV irradiation, whereas the PEI solar cells maintain their diode-like characteristics. Looking at the semi-log plots (**Figure 6.2.b & d**), one can also see that the slope of the characteristics decreases in the cells with ZnO (as shown by the blue arrows), indicating an increase in the ideality factor for the UV-exposed cells. The increase in ideality factor points to the presence of shunts, suggesting increased leakage of electrons to the hole collection contact and/or of holes to the electron collection contact. Since the hole collection contacts are the same in all OSCs (always MoO<sub>3</sub>/Al), differences in leakage currents among the cells must then be associated with the electron collection contacts. It follows that the increase in ideality factor in the cells with the ZnO EELs must be caused by increased hole leakage to the ITO contact. The observed increase in hole extraction by ITO/ZnO at forward bias and in hole injection from this contact at reverse bias indicates that ITO/ZnO contact loses its hole-blocking functionality/electron selectivity over time under the UV stress. In contrast, the ITO/PEI contact maintains its charge selectivity and thereby avoids UV-induced  $V_{oc}$  loss.

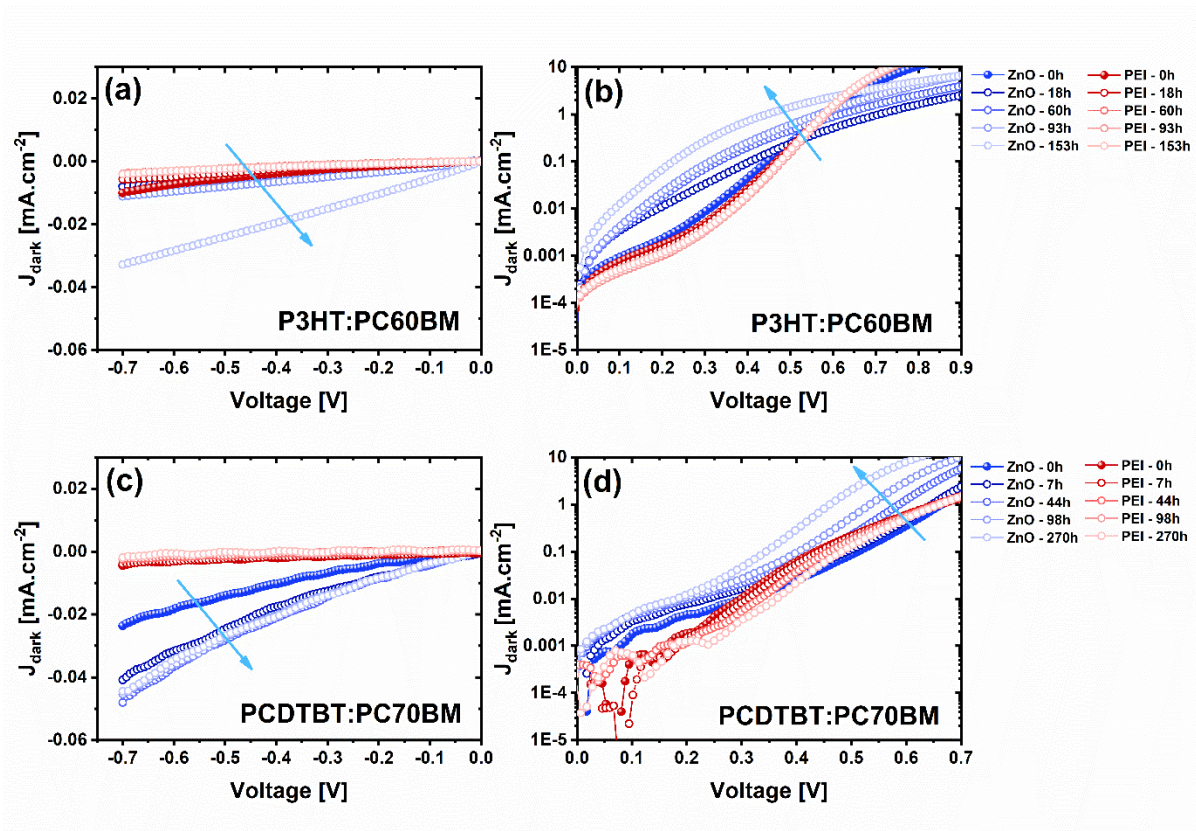


**Figure 6. 2.** Dark  $J$ - $V$  characteristics of the fresh (filled circles) and after different time intervals of UV irradiation (open circles) of OSCs with ZnO (blue circles), and PEI (red circles): (a) & (c) linear scale at reverse voltage; (b) & (d) semi-logarithmic scale at forward voltage; based on P3HT:PC60BM OSCs (top), and PCDTBT:PC70BM OSCs (bottom). The blue arrows point to the order the characteristics were collected at the time of the aging.

To further investigate the loss in electron selectivity of ITO/ZnO contacts by the UV stress and the stability benefits of the ITO/PEI in this regard, we incorporated these EELs in HODs. The HODs had the same device structure as the OSCs except that the P3HT:PC60BM and PCDTBT:PC70BM layers were replaced by neat layers of P3HT and PCDTBT, respectively. Bias is applied such that the Al electrode is held at a more positive potential relative to the ITO contact, resulting in hole injection from the MoO<sub>3</sub>/Al contact into the P3HT (or PCDTBT) and hole extraction at the ITO/ZnO or ITO/PEI contacts. Hole injection via the high-WF MoO<sub>3</sub>/Al is known to be efficient [162]. Although electron injection from ITO/ZnO and ITO/PEI into the organic layer could occur in principle, electron transport will be blocked by P3HT and PCDTBT due to their limited electron mobility [110]. Consequently, any measured current will be predominately due to either the transport of holes across the EEL or the



recombination of holes with injected electrons at the ITO/ZnO contact. Additionally, to investigate if the ITO electrode itself may be playing any role in the observed changes in hole extraction of the ITO/ZnO vs. ITO/PEI contacts under UV exposure, we also tested a HOD in which only ITO (without ZnO or PEI) is used as the collection contact in a P3HT-based HOD. As expected, before UV exposure, all devices show only small current densities, indicating that hole extraction from the organic layer to the collection contact is not efficient initially (**Figure 6.3**). However, after UV illumination, a significant increase in hole current is observed in the devices with ITO (**Figure 6.3.a**) and ZnO (**Figure 6.3.b**, and **6.3.d**), whereas the  $J$ - $V$  characteristics of the devices with PEI remain almost unchanged (**Figure 6.3.c**, and **3.e**). This significant increase in hole currents in the ZnO devices clearly indicates that holes can be increasingly extracted by the ITO/ZnO contact, suggesting a reduction in the selectivity/or hole blocking properties after the UV aging. Interestingly, the devices with ITO alone showed an even larger increase in hole currents after UV aging. The loss of hole blocking characteristics of ZnO under illumination was illustrated previously [69, 96, 110, 163]. However, here, we show that this selectivity loss is also associated with the ITO/ZnO interface and not only the ZnO/organic-layer interface. These results are in agreement with the origins of the shunting behavior concluded by Trost et al. [110], and suggest that apart from ZnO/organic interface, the ITO/ZnO interface also plays a role in this behavior.

Due to the higher Fermi energy level of ITO relative to the HOMO level of the donor material, hole extraction from the organic layer to the ITO contact, without any interfacial layers, will generally be efficient. ITO typically has adsorbed oxygen molecules on its surface due to substrate cleaning and handling in air. Exposing ITO to UV causes a gradual desorption of this pre-adsorbed oxygen, resulting in charge rearrangement on ITO surface. This redistribution of surface charges forms a surface dipole and consequently causes a downward shift of vacuum energy level above ITO, reducing its WF [97, 164]. As a result, hole extraction by ITO becomes even more favorable. This effect is illustrated schematically in **Figure 6.4.a**. ZnO, with its deep valance band, can act as a hole blocking layer that prevents hole extraction from the organic layer by ITO. The increase in hole currents after UV aging suggests that the hole-blocking effect of ZnO decreases, hence allowing for more holes to be extracted by the ITO contact. Although the exact mechanism for the increased hole extraction is unclear, the effect may be due to a high density of defect states in the fresh ZnO [165], which, under prolonged UV illumination, become increasingly filled with holes and, as a result, allow the transport of holes across the ZnO layer via hopping between these defect sites to become non-negligible [69]. That allows the transport of holes from the organic layer (P3HT or PCDTBT) into the ZnO layer to become efficient,

facilitated by the reduction in the ITO WF. This effect is illustrated schematically in **Figure 6.4.b**. In contrast, PEI being an insulating wide band-gap material, will not be able to provide a sufficient number of carriers or accessible defect states that can be used to support the transport of holes across it under UV exposure. **Figure 6.4.c** depicts this scenario. Alternatively, it has been shown that materials with large dipole moments (like PEI) have a preferential molecular alignment such that their positive ends are directed towards the OSC active layer, resulting in electron accumulation and hole depletion in the vicinity of the interface of organic layer and the next electron contact [123]. Such hole depletion region will expectedly hinder the transport of holes from the organic layer into the PEI, and will therefore maintain the hole blocking functionality of PEI, independent of any changes in ITO WF. **Figure 6.4.c** depicts this scenario. As a result, ITO/PEI contact can maintain its high degree of charge selectivity even after prolonged UV irradiation, causing hole leakage and the resultant  $V_{oc}$  loss to be minimized.

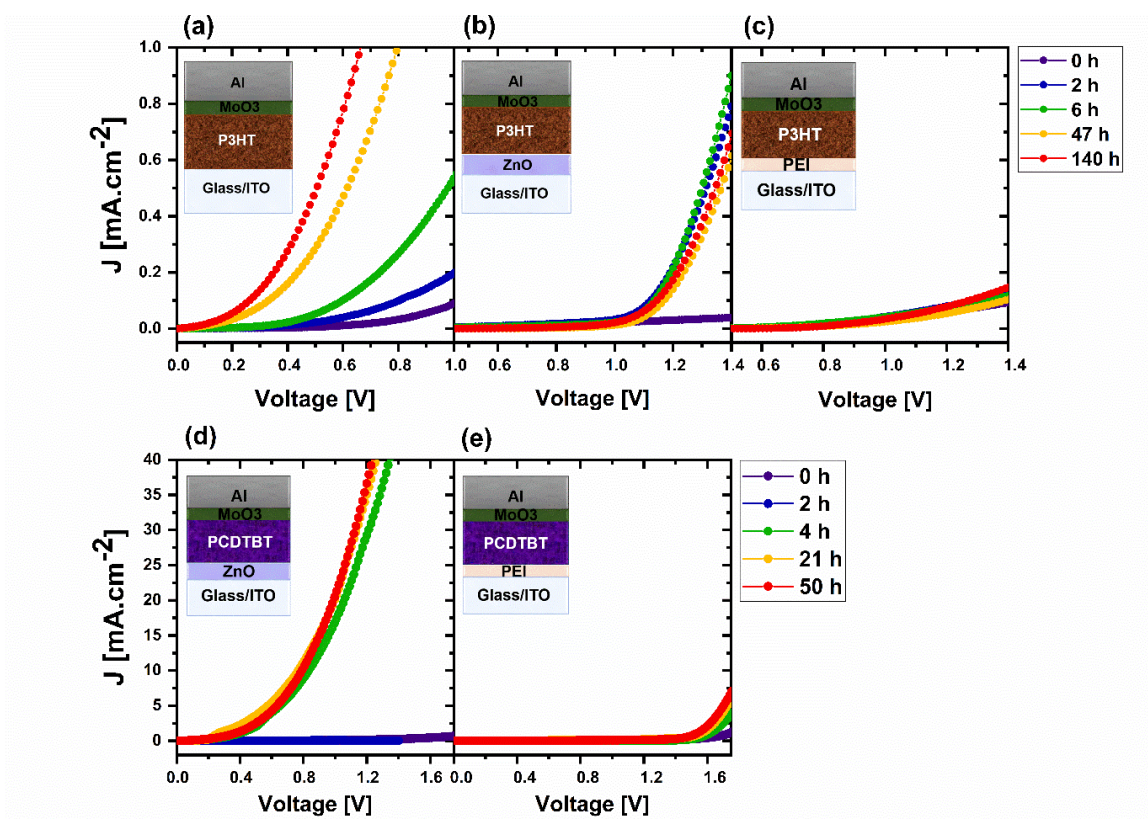


**Figure 6. 3.**  $J$ - $V$  characteristics of the fresh (filled circles) HODs and the same devices after different time intervals of UV aging (open circles) with ITO (a ), ZnO (b & d), and PEI (c & e), where only P3HT and PCDTBT is used as an organic layer without the addition of acceptor. Schematic depictions of the HODs are provided within each figure.

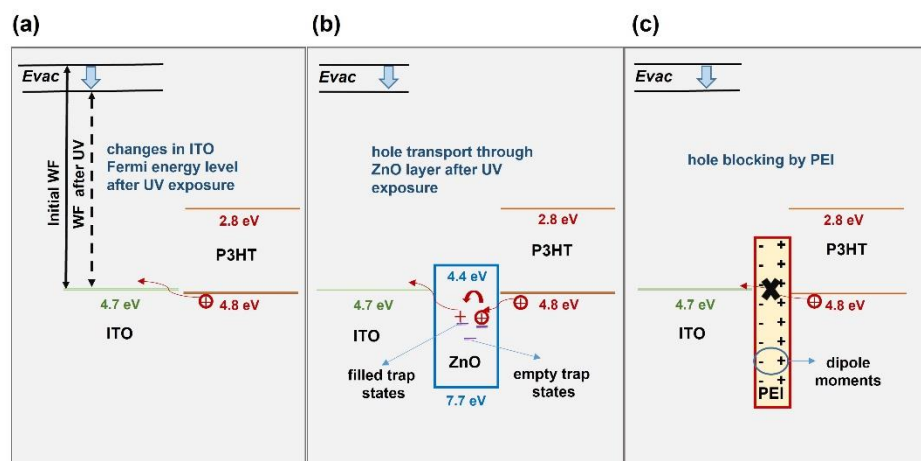


**Figure 6. 4.** Illustration of the mechanism by which the UV-induced hole leakage through ITO (a) and ITO/ZnO (b) contacts occur; Blue arrows show the vacuum energy level variation after UV exposure. The hole-blocking functionality of ITO/PEI contact is also shown (c).

To investigate if morphological changes in the BHJ, possibly induced by the UV-irradiation, may also be involved in the observed photostability behavior, we use AFM measurements to study the morphological characteristics of fresh and UV-aged ZnO/P3HT:PC60BM, and PEI/P3HT:PC60BM film stacks. AFM images from these measurements are provided in **Figure S6.2**. Results show that the fresh films have similar surface topography with ZnO/P3HT:PC60BM film exhibiting only a slightly higher surface roughness relative to the PEI/P3HT:PC60BM film, with an  $R_{\text{rms}}$  of 1.8 nm versus 1.5 nm, respectively. Furthermore, the  $R_{\text{rms}}$  values are found to change only modestly (less than 10%) after the UV exposure in both cases, with no appreciable extent of differences between the PEI vs. the ZnO stacks. The close similarity between the surface topography of P3HT:PC60BM films when coated on PEI vs. ZnO even after the UV stress suggests that morphological effects do not play a significant role in the OSC photostability enhancement observed when using PEI.

The correlation between the decrease in the charge selectivity of contacts and increased surface recombination in OSCs has been discussed by Reinhardt et al. [166]. To analyze the direct impact of selectivity changes with UV aging on charge recombination mechanisms, we measured the dependence of both  $V_{\text{oc}}$  and  $J_{\text{sc}}$  on the illumination light intensity for OSCs with PCDTBT:PC70BM. The results are presented in **Figure 6.5**.

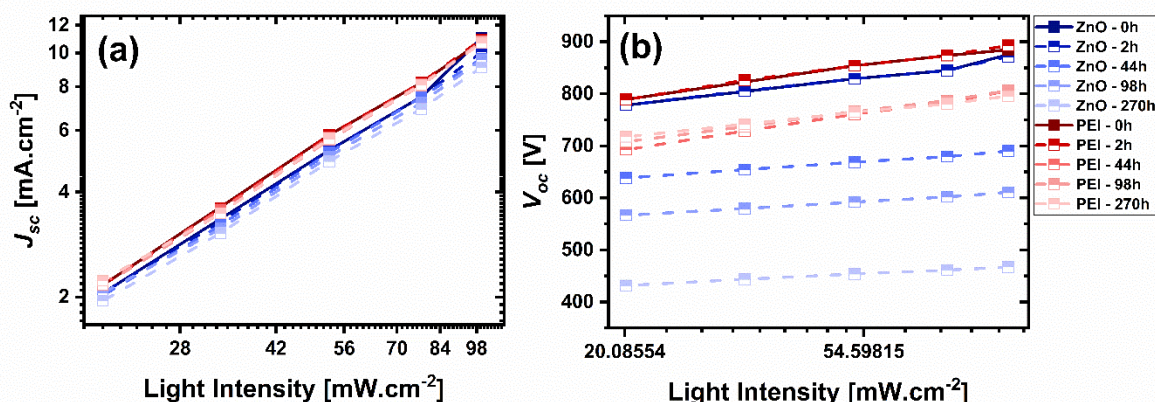


**Figure 6. 5.**  $J_{sc}$  (a) and  $V_{oc}$  (b) vs. light intensity of PCDTBT:PC70BM-based OSCs with ZnO (blue squares) and PEI (red squares) EELs.

Results show that both the ZnO and PEI cells exhibit  $\alpha \sim 1$ , before and after UV aging, indicating that bimolecular recombination can be neglected. The slope of the  $V_{oc}$  versus the natural logarithm of the light intensity (**Figure 6.5.b**) in the fresh cells, with both the ZnO and PEI EELs, is close to  $2KT/q$ , suggestive of significant trap-assisted bulk recombination and negligible surface recombination at the contacts. However, after the UV stress, only the slope of the cells with the ZnO EEL decreases significantly (from 2.13 to 0.85  $KT/q$ ), indicating a significant increase in surface recombination. The slope of the cells with the PEI EEL shows a smaller decrease after the UV exposure in comparison (from 2.44 to 1.86  $KT/q$ ). The increased surface recombination in the cells with the ZnO EEL is consistent with the increase in hole leakage in these cells after the UV aging (**Figure 6.2.d**). Therefore, the results show that the main cause of  $V_{oc}$  loss in the OSCs with ZnO EELs with UV aging is increased surface recombination due to the deterioration in the electron selectivity of the electron extraction contact and an increase of hole leakage. They also reveal that the origin of the photostability enhancement upon using PEI as an EEL is its ability to maintain electron selectivity even after UV irradiation and thus to avoid an increase in surface recombination at the contact and subsequent  $V_{oc}$  losses.

We have to note that, although surface recombination is known to primarily affect  $V_{oc}$  [161], it may also lead to a decrease in  $J_{sc}$  since some of the photo-generated charge carriers will be lost due to surface recombination [166]. That may explain the smaller  $J_{sc}$  loss in OSCs with PEI compared to those with

ZnO as shown in **Figure S6.1**. This effect is however only secondary relative to the  $V_{oc}$  stability improvement.

### 6.3 Conclusion

In summary, results show that replacing the commonly used ZnO EEL with PEI can eliminate UV-induced  $V_{oc}$  loss in OSCs and enhance their photostability. This enhancement is observed in two different BHJ material systems (P3HT:PC60BM and PCDTBT:PC70BM). As verified by dark  $J$ - $V$  characteristics of OSCs and hole-only devices, the higher  $V_{oc}$  stability attained upon using PEI instead of ZnO is mainly due to the ability of the ITO/PEI contact to maintain a higher degree of electron selectivity and hole blocking functionality under UV irradiation in comparison to the ITO/ZnO contact. Using  $V_{oc}$  vs. light intensity analysis demonstrates that an enhanced rate of surface recombination occurs in the cells with ZnO under UV exposure as a consequence of the UV-induced selectivity loss of ITO/ZnO contact. These findings suggest that apart from ZnO/BHJ interface, the ITO/ZnO interface also plays a role in this selectivity loss. In contrast, the  $V_{oc}$  vs. light intensity results from the OSCs with PEI confirm that surface recombination remains negligible, indicating that the hole blocking functionality of the contact is maintained. Therefore, in order to enhance the photostability of organic solar cells to a significant extent, it is essential to maintain the selectivity of the contact and thus minimize the surface recombination at both ITO/EEL and EEL/BHJ interfaces, as in the case of the ITO/PEI contact.

## Chapter 7

# The Effect of Replacing ZnO EELs with Green-Solvent Processable Molecules with Large Dipole Moments as a Universal Route for Enhancing Stability

*This work has been published in Sadeghianlemraski, M., Nouri, M., Wong, W. S., and Aziz, H., Wiley Adv. Sustainable Systems, pp. 2100078, 2021. It has been reproduced with permission from the publisher.*

### 7.1 Introduction

Establishing the promising benefits of the dipole moment of PEI as an EEL that can provide and maintain electron selectivity even after prolonged irradiation and be easily processed using green solvents, we then test the universality of the approach.

In a study of a group of water/alcohol-soluble organic materials with large dipole moments including Histidine, Phenylalanine, Sarcosine, 2-pyridone, and 5-ethyl-thiophene-2-carboxylic acid as EELs, Würfel et al. found that the high dipole moments alter the electric potential distribution at the electrode/active-layer interface, providing a high degree of charge selectivity [123]. Among the studied dipole interlayers, Histidine and Sarcosine showed the best compatibility with several donor-acceptor BHJ systems [123]. Given the potential benefits of these materials as EELs, investigating their effect on OSC stability also becomes essential.

Therefore, in this work, we systematically study the stability behavior of OSCs with Histidine and Sarcosine and investigate their influence on UV-induced electron-selectivity reduction. The latter is a primary failure mechanism in OSCs with a ZnO EEL, as illustrated in previous chapters. The DM-EELs are studied in inverted OSCs with P3HT:PC60BM or PM6:Y6 BHJ donor-acceptor systems. The first is selected as the most archetypical fullerene-based BHJ system, whereas the second represents a non-fullerene high-efficiency system that has recently attracted significant attention and popularity. Ideality factor studies reveal that the interfacial dipole layers stabilize the contact's electron-selectivity and prevent increased surface recombination after UV stress. The results highlight the viability and

benefits of using DM-EELs over ZnO as green-solvent processable EELs for improved stability in OSCs.

## 7.2 Results and Discussion

Inverted OSCs with the structure of ITO/EEL/BHJ/MoO<sub>3</sub>/Al, comprising P3HT:PC60BM or PM6:Y6 for the BHJ donor-acceptor system were fabricated. Histidine or Sarcosine was used as DM-EELs, whereas ZnO was used as a reference EEL for comparison. **Figure 7.1** depicts the chemical structures of these DM-EELs and of the donor-acceptor materials.

First, we examined the influence of the different DM-EELs on the PV performance of the OSCs. The PV parameters of freshly made cells are provided in Table 7.1, where each number represents the average value of the PV parameters of four cells from each case. The small variations in the PCE among cells with the same active layer but different EELs can be attributed to the familiar device-to-device variations among OSCs. The comparable parameters of the cells also show that replacing ZnO with DM-EELs does not significantly affect initial performance.

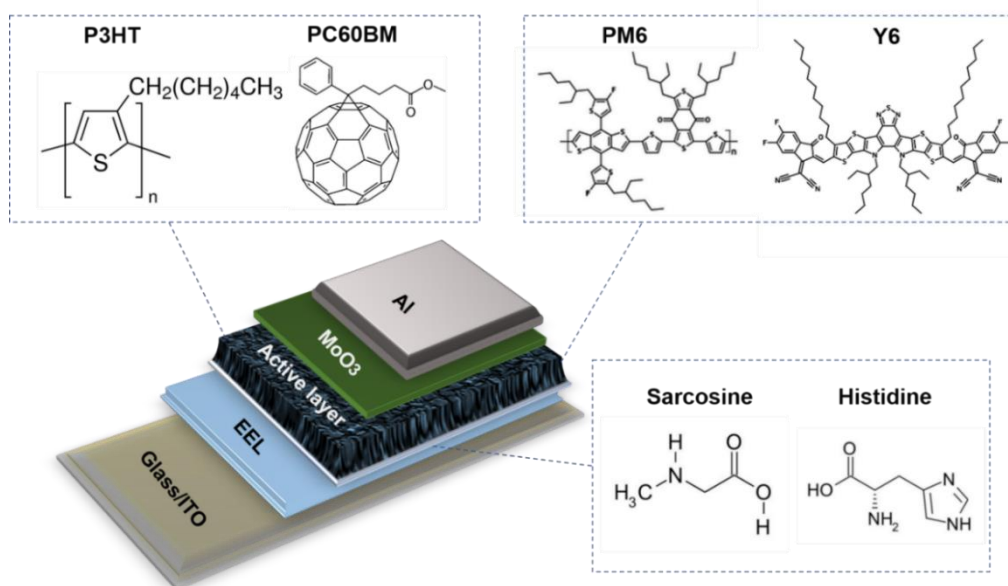


**Figure 7. 1.** Architecture of the studied OSCs with the chemical structures of the Histidine and Sarcosine DM-EELs and of the P3HT:PC60BM and PM6:Y6 active layers.

**Table 7. 1.** PV parameters of P3HT:PC60BM-based and PM6:Y6-based organic solar cells with the Histidine, Sarcosine, and ZnO EELs.

		$J_{sc}$ [mA.cm <sup>-2</sup> ]	$V_{oc}$ [mV]	FF [%]	PCE [%]
<b>P3HT:PC60BM</b>	<b>ZnO</b>	6.64	650.46	60.54	2.61
	<b>Histidine</b>	6.87	640.68	58.36	2.57
	<b>Sarcosine</b>	8.81	639.59	47.55	2.68
<b>PM6:Y6</b>	<b>ZnO</b>	26.71	772.04	59.31	12.21
	<b>Histidine</b>	25.46	758.73	58.53	12.06
	<b>Sarcosine</b>	27.38	767.44	58.22	12.12

We wish to point out that for both active layer systems, the OSCs with ZnO do not require photoactivation as indicated from the S-shape-free  $J$ - $V$  characteristics of the fresh cells depicted in **Figure S7.1**. Additionally, the PCE of our PM6:Y6 cells with ZnO EEL is  $\sim 12.2\%$ , almost 22% smaller than the PCE of 15.7% for the similar device structure reported by Yuan et al.[33]. This lower PCE, mainly originated from a lower FF, is due to our substrate's design, which does not allow us to achieve optimum resistance.

Then, we investigated the influence of the DM-EELs on the stability of OSCs over time and under UV irradiation. **Figure 7.2** illustrates the PV properties of continuously UV-irradiated cells, where the parameters are normalized to their initial value. The OSCs with DM-EELs exhibit remarkably higher photostability for both donor-acceptor systems, reflected in a much slower decay rate in their PCE than their counterparts with the ZnO EELs. For the P3HT:PC60BM OSCs, the cells with DM-EELs (Histidine and Sarcosine) showed a decrease of only  $\leq 5\%$  in PCE after 350 h of UV irradiation versus  $\sim 30\%$  in their ZnO EEL counterpart. For the PM6:Y6 OSCs, the decrease in PCE was  $\leq 25\%$  in the case of the DM-EELs, versus  $\sim 60\%$  in the case of ZnO after 138 h of UV irradiation. We also tested the temporal stability of these devices under maximum power-point current density (by applying a constant current equal to the maximum power point current density extracted from the illuminated  $J$ - $V$  measurements) and found the trends to be comparable to those obtained from the open-circuit conditions that are shown in **Figure 7.2.b**.



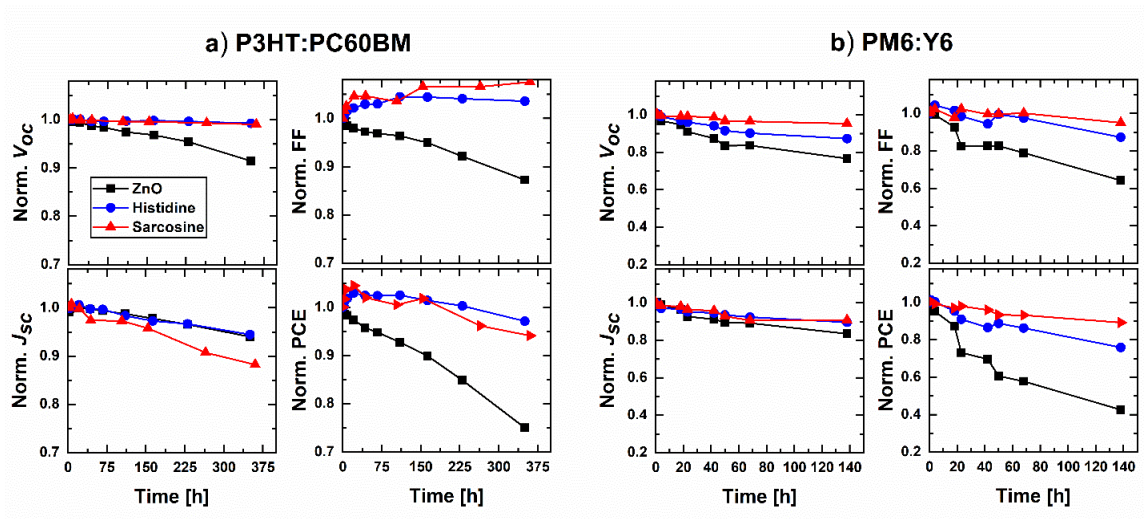


**Figure 7. 2.** Normalized  $V_{oc}$ , FF,  $J_{sc}$ , and PCE versus different time intervals of UV irradiation of (a) P3HT:PC60BM and (b) PM6:Y6 OSCs, with the ZnO, Histidine, and Sarcosine EELs.

Another identical set of OSCs was kept in the dark as a control set for comparison. Comparing changes in PV parameters of the UV-irradiated and control devices helps us distinguish between losses introduced by the UV irradiation from those arising simply due to temporal changes caused by the passing of time. For the P3HT:PC60BM OSCs, we observed insignificant changes in the control (**Figure S.7.2. a**) but noticeable degradation under UV irradiation. For the PM6:Y6 OSCs, in contrast, the most significant part of the degradation appears to be temporal in nature, with the UV irradiation playing only a minor role (**Figure S7.2.b**). Considering these observations, we focus our investigation on photodegradation (under UV irradiation) for the P3HT:PC60BM cells and on temporal degradation (under the dark condition) for the PM6:Y6 cells. Interestingly, despite the different degradation behavior in the two active-layer systems (i.e., UV-induced or only temporal in nature), using the DM-EELs clearly enhances the stability in both cases.

In Chapter 5, we showed that UV irradiation does not appreciably alter the morphology or the UV-Vis absorption characteristics of P3HT:PC60BM films coated on ZnO, indicating that morphological changes or photocatalytic effects [102] are not primary root causes in the observed low photostability of P3HT:PC60BM-based OSCs with ZnO EEL. Knowing from the literature that low morphological stability might be a factor in the case of non-fullerene-based devices [167] (discussed in Chapter 2), we conducted AFM and UV-Vis measurements on the PM6:Y6 OSCs. The results are presented in **Figure**

**S7.3** and **S7.4**, respectively. The AFM measurements give surface roughness values of 0.94, 1.17, and 1.05 nm for PM6:Y6 coated on ZnO, Histidine, and Sarcosine EELs on ITO substrates, respectively. The UV-Vis absorption spectra of the EEL/PM6:Y6 stacks (coated on quartz substrates) are all similar in the PM6 region. The Y6 band exhibits a small red-shift (~5nm) in the DM-EEL/PM6:Y6 stacks (suggestive of somewhat higher crystallinity), but the spectra are otherwise essentially identical. More notably, however, there are no detectable changes in all spectra after two months of dark storage or even after one week of UV irradiation in an inert atmosphere, regardless of the EEL choice, except for a small increase in the absorption region of ZnO and PM6 in the case of the ZnO/PM6:Y6 sample. To further verify whether this difference might be associated with increased crystallinity and, more importantly, whether it would affect the morphological stability of PM6:Y6, we repeated the UV-Vis measurements after one week of UV irradiation in the air. As explained in Chapter 2, the initial crystallinity of a polymer governs its photo-oxidation rate [72, 94]. Thus, if there is a significant difference in the initial crystallinity of PM6:Y6, influenced by the underlying layer, we would expect to see a noticeable difference in the photo-oxidation rate. As shown in **Figure S7.4** (red curves), all spectra show a similar 0.8 nm blue-shift and decreased absorption after UV irradiation in the air, suggesting insignificant differences in the PM6:Y6 film crystallinity regardless of the underlying EEL. The findings show that the higher stability of the OSCs with DM-EELs is not primarily due to suppressing any morphological changes in the PM6:Y6 over time. We also measured the TRPL of PM6 films coated on different EELs (**Figure S7.5**). The luminescence decay rate remains unchanged after storage in an inert atmosphere, suggesting that the underlying layer does not affect the exciton lifetime of the polymer, further affirming the negligible effect of the EELs on morphology.

To understand the root causes of the stability enhancement achieved upon replacing ZnO with DM-EELs, we investigated the charge recombination mechanisms in the OSCs. For this purpose, we measured  $J_{sc}$  and  $V_{oc}$  at different light intensities (**Figure 7.3** and **Figure S7.6**, respectively). An analysis of the data in **Figure 7.3** produces  $\alpha$  values between 0.96 and 1.06 in the P3HT:PC60BM cells and between 0.94 and 0.99 in the PM6:Y6 cells (Table S7.1 presents the  $\alpha$  values of each case). The data therefore indicates that all OSCs – regardless of the donor-acceptor system - exhibit insignificant bimolecular recombination before and after aging (under UV irradiation or dark condition) as inferred from the close to unity  $\alpha$  values in all of them.

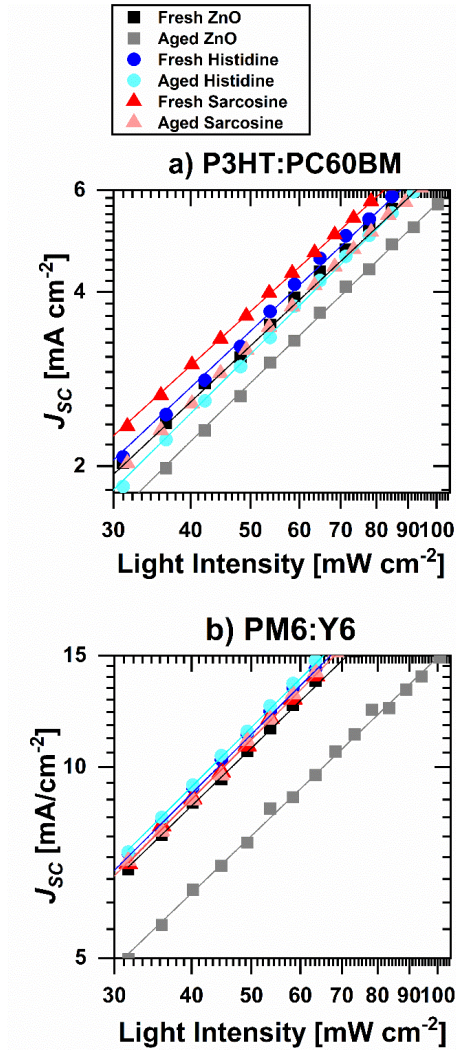


**Figure 7. 3.**  $J_{sc}$  versus light intensity on a log-log scale of fresh vs. aged (a) P3HT:PC60BM and (b) PM6:Y6 cells with the ZnO, Histidine, and Sarcosine EELs. Aged means after UV-irradiation in case of (a) and after dark storage in case of (b). The lines represent the linear fits in each case.

To further investigate the recombination mechanisms, we studied and compared the voltage-dependent characteristics of both light and dark ideality factors before and after aging [126]. The dark ideality factor ( $n_d$ ) was derived from the slope of the dark  $J$ - $V$  characteristics, according to  $n_d = \frac{q}{KT} \frac{dV}{d \ln(J)}$ , where  $q$ ,  $K$ ,  $T$ ,  $V$  and  $J$  represent the elementary charge, Boltzmann's constant, temperature, the applied voltage, and the dark current density whereas the light ideality factor  $n_l$  was obtained from the  $V_{oc}$  versus light intensity ( $\phi$ ) characteristics (**Figure S7.6**) using the equation:  $n_l = \frac{q}{KT} \frac{dV_{oc}}{d \ln(\phi)}$ .

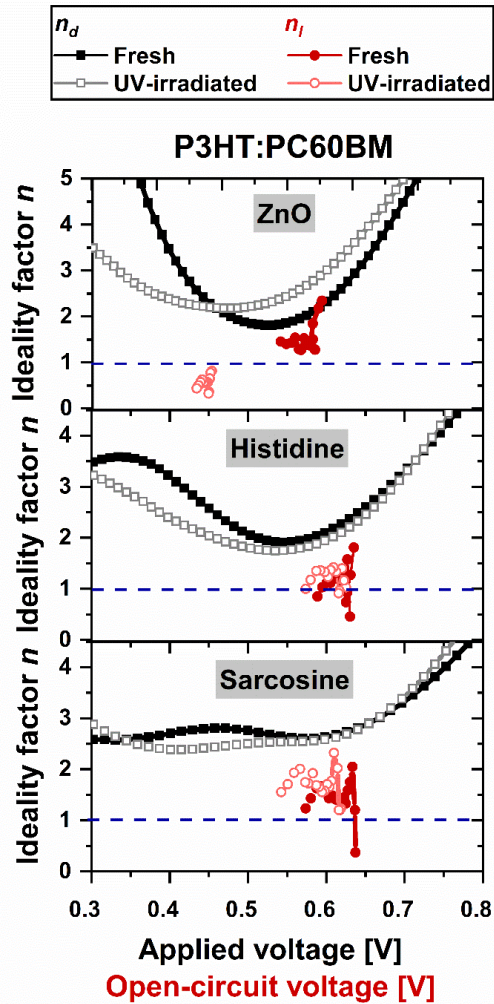


**Figure 7. 4.** Dark and light ideality factor values versus voltage of the fresh (filled symbols) and UV-irradiated (open symbols) P3HT:PC60BM OSCs with the ZnO, Histidine, and Sarcosine EELs. The black/grey squares represent the dark ideality factors ( $n_d$ ) derived from the dark  $J$ - $V$  characteristics. The red circles represent the light ideality factors ( $n_l$ ) obtained from the  $V_{oc}$ -light intensity characteristics.

We first look at the ideality factor versus voltage trends of the P3HT:PC60BM cells. As can be seen from **Figure 7.4**, all cells exhibit relatively constant  $n_d$  values over the voltage range of 0.5-0.6 V and  $n_l > 1$  for most voltages over the entire  $V_{oc}$ 's range. After UV stress, the  $n_d$  and  $n_l$  remain relatively unchanged for OSCs with the DM-EELs, with only a slight shift in  $n_l$  to lower  $V_{oc}$  values. In contrast, the ZnO EEL cell shows an overall increase in  $n_d$  values, a notable shift in  $n_l$  towards lower  $V_{oc}$  values, and a drop in the  $n_l$  values to  $< 1$  at all voltages. The latter points to substantial surface recombination

at the electrodes [126, 161]. Such surface recombination can decrease carrier density, negatively affecting quasi-Fermi level splitting. Thus, further increasing light intensity will not bring about additional changes in  $V_{oc}$ , causing  $V_{oc}$  to saturate and hence an  $n_l$  below unity. The results of the ZnO cells are consistent with our recent findings that increased surface recombination is the primary cause of degradation in P3HT:PC60BM-based cells with ZnO under prolonged irradiation [168]. The observations also show that the higher photostability of the cells with DM-EELs originates primarily from an unchanged recombination mechanism in these cells. Since all devices are structurally identical, apart from the EELs, differences in recombination mechanisms among them after the UV-irradiation must be associated with the electron collection contacts. Therefore, the use of DM-EELs instead of ZnO must be preventing the UV-induced increase in surface recombination.

Looking at the ideality factor versus voltage trends of the PM6:Y6 cells (**Figure 7.5**), one can see that using DM-EELs once again leads to smaller changes in  $n_d$  and  $n_l$  with voltages, with the Histidine and Sarcosine cells showing an almost constant  $n_d$  over the 0.4-0.65 V and 0.3-0.65 V voltage ranges, respectively. After dark storage for 138 h, the Histidine cells exhibit a small increase in  $n_l$  and  $n_d$  values and a slight shift in the  $n_l$  towards lower  $V_{oc}$  values, whereas the characteristics of the Sarcosine cells remain almost unchanged. In contrast, while the fresh ZnO cell exhibits a relatively constant  $n_d$  over the 0.5-0.65 V voltage range, the  $n_d$  exhibits a strong voltage dependency after the 138 hours of storage. The  $n_l$  characteristics also shift to much lower  $V_{oc}$  values.

From the observations, it can also be seen that while replacing ZnO with either DM-EEL (Histidine or Sarcosine) leads to significant stability enhancement in both donor-acceptor systems, Histidine gives slightly higher stability than Sarcosine in the P3HT:PC60BM OSCs, whereas the opposite is true for the PM6:Y6 OSCs. We, therefore, focus on the Histidine/P3HT:PC60BM and Sarcosine/PM6:Y6 material combinations for additional investigations.

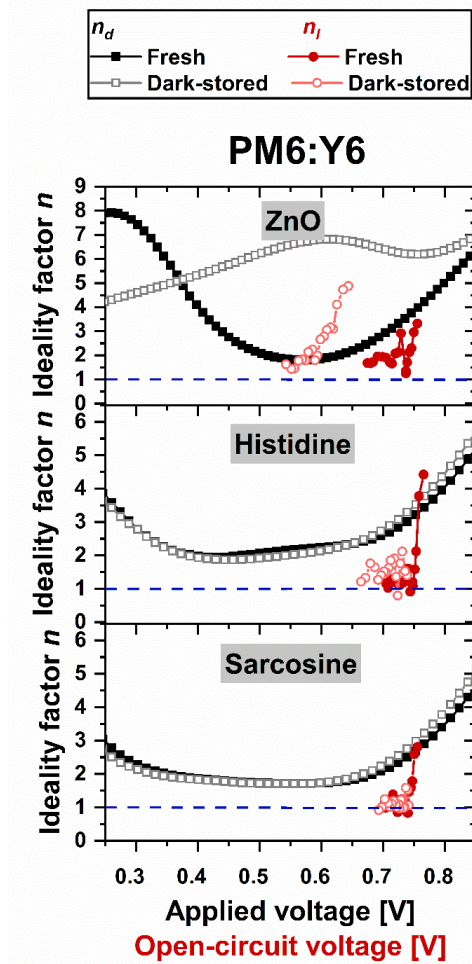


**Figure 7. 5.** Dark and light ideality factor values versus voltage of the fresh (filled symbols) and dark-stored (open symbols) of PM6:Y6 OSCs with the ZnO, Histidine, and Sarcosine EELs. The black/grey squares represent the dark ideality factors ( $n_d$ ) derived from the dark  $J$ - $V$  characteristics. The red circles represent the light ideality factors ( $n_l$ ) obtained from the  $V_{oc}$  vs. light intensity characteristics.

**Table 7. 2.** Shunt resistance obtained at voltages around 0 V and series resistance obtained at voltages above 0.9 V, both extracted from dark  $J$ - $V$  characteristics of the PM6:Y6 OSCs with the different EELs. The data is obtained from the fresh cells and after storage in the dark.

	$R_{sh}$ [ $K\Omega.cm^2$ ]		$R_s$ [ $\Omega.cm^2$ ]	
	Fresh	Dark-stored	Fresh	Dark-stored
ZnO	428	35.2	6.2	6.3
Histidine	360	775	8.4	9.3
Sarcosine	550	808	6.1	7.2

Since the findings suggest that the suppression of recombination at the ITO/DM-EEL electron collecting contact plays a leading role in the OSC stability enhancement, we compared electron collection of the DM-EELs and ZnO EEL in EODs. **Figure 7.6** displays the  $J$ - $V$  characteristics of EODs with the structure of ITO/EEL/(PC60BM or Y6)/LiF/Al. In these devices, the ITO electrode is biased with a more positive potential relative to the Al electrode, leading to the injection of electrons from the Al/LiF contact and their collection at the ITO electrode. Therefore, in these devices, the electrons traverse the EELs in the same direction as in the OSCs. From **Figure 7.6**, it can be seen that the EODs with the DM-EELs have higher current at any given voltage relative to their ZnO counterparts, indicating that the DM-EELs allow for easier electron transport and collection from the acceptor materials (PCBM and Y6) to the ITO in comparison to ZnO. The fact that the DM-EELs have a higher electron collection efficiency than ZnO but do not appreciably alter the initial PCE of the OSCs indicates that electron collection from the active layer is not a limiting factor in the OSCs. Changes in the EOD characteristics over time and/or after UV irradiation is almost similar regardless of the EELs. The similar trends further verify that the significant difference in the PCE loss in the ZnO OSCs versus DM-EELs OSCs (after the UV irradiation or storage in the dark) is unlikely due to a deterioration in electron collection efficiency. The strong stability dependence of the studied OSCs on EELs instead might be primarily due to the EELs' role in preventing hole leakage; a phenomenon - we demonstrated in Chapter 5 and 6- plays a major role in the deterioration in the performance of OSCs with ITO/ZnO contacts under UV irradiation.

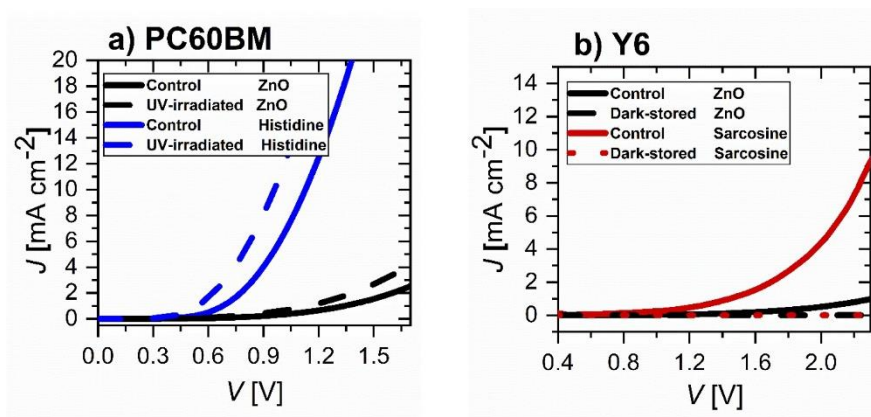


**Figure 7. 6.**  $J$ - $V$  characteristics of the electron-only devices with the structure of ITO/ZnO or Histidine/PC60BM/LiF/Al and (b) ITO/ZnO or Sarcosine/Y6/LiF/Al.

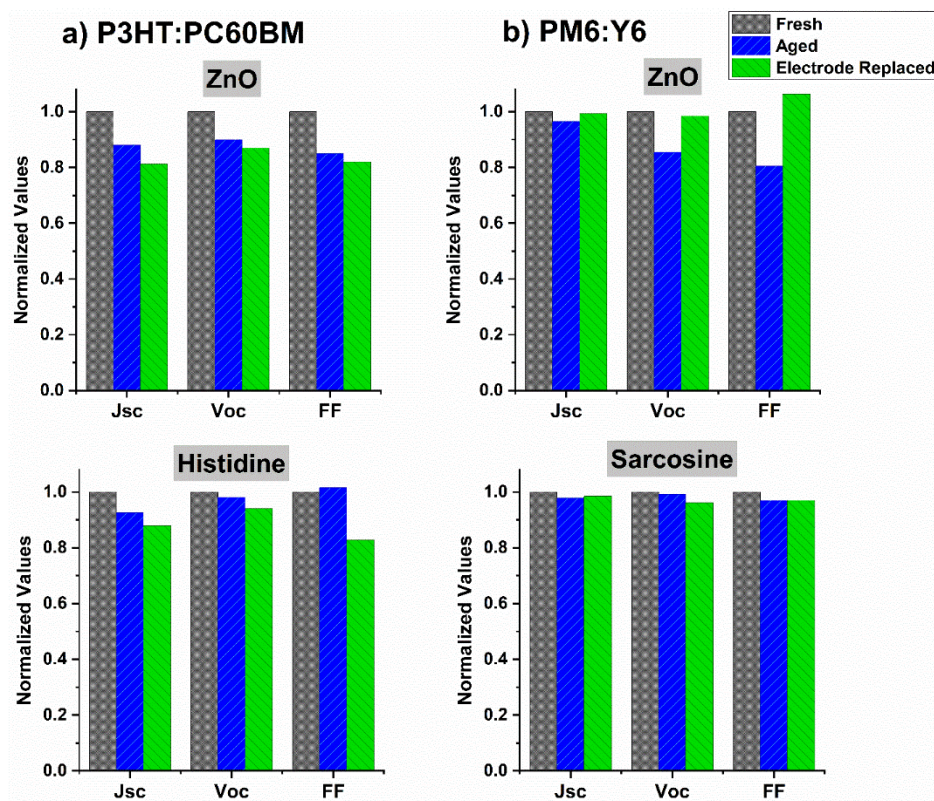


**Figure 7. 7.** Normalized values of  $J_{sc}$ ,  $V_{oc}$ , and FF of a) P3HT:PC60BM with the ZnO and Histidine EELs and PM6:Y6 OSCs with the ZnO and Sarcosine EELs. Values are extracted from fresh cells (as a reference) and from aged cells before and after replacing the electrodes ( $\text{MoO}_3/\text{Al}$ ).

A study by Lee et al. [169] demonstrated a strong dependence of the top-electrode/active-layer adhesion, and thus OSC stability, on the strength of the molecular interaction between the EEL and the organic active layer. Poor adhesion between the top electrode and the organic layer can accelerate degradation due to increased ambient oxygen and moisture diffusion [170]. We also previously showed that incompatibilities between the electron and hole extraction layers could sometimes result in degradation [43]. Therefore, to investigate if some of the observed degradations might be the result of changes at the top contact influenced by the EEL, we tested the effect of peeling off the top electrode [94] from the aged cells and replacing it with a new one [94]. **Figure 7.7** depicts normalized  $J_{sc}$ ,  $V_{oc}$ , and FF values of the pristine and of the aged OSCs before and after replacing the top electrode. For the P3HT:PC60BM cells, regardless of the EEL, replacing the electrodes does not lead to any performance recovery in the aged cells and even slightly worsens it. This finding supports the earlier conclusion that the observed photodegradation in these cells primarily arises from the EEL/BHJ interface. In contrast,



replacing the electrode in case of the aged PM6:Y6 cell with the ZnO EEL results in a significant performance recovery, indicating that the top contact plays a major role in the poor stability behavior. These findings suggest that any contributions from BHJ morphological changes to the efficiency loss are not the leading cause of degradation in these devices. More notably, however, different from the ZnO device, replacing the electrode does not lead to any appreciable changes in the small losses in the Sarcosine cell. The fact that replacing the electrode leads to a recovery in the performance in only the PM6:Y6 OSCs and only when ZnO EEL is used suggests that the use of ZnO has a negative effect on the top contact in these devices. Although the exact mechanism is not clear, this phenomenon clearly depends on the BHJ system.

To further investigate differences between the DM-EEL and ZnO-EEL in the P3HT:PC60BM devices and the effect of the UV irradiation on them, we performed dark  $J$ - $V$  measurements on the UV-irradiated cells with ZnO and Histidine over the 100-300 K temperature range and compared them with characteristics of the dark control devices. **Figure 7.8 (a-d)** presents the  $J$ - $V$  characteristics, where the bias value represents the potential of the Al electrode relative to ITO. The OSCs exhibit overall similarities, all displaying similar  $J$ - $V$  characteristics at 300 K and a decrease in current at any given voltage as the temperature decreases. This decrease in current was however more significant in the ZnO-EEL OSCs. Since all OSCs have the same hole injection contact (MoO<sub>3</sub>/Al) and donor-acceptor layer, the larger reduction in current in the ZnO EEL OSCs must be associated with reduced electron injection at the ITO/EEL contact. Notably also, all characteristics exhibit some well-defined “ripple-like” features in the 0.3-0.6 V range, the range of the diode exponential current regime, at higher temperatures. These ripples appear at the same voltages regardless of the EEL, suggesting that they are associated with bulk transport in the donor-acceptor system rather than charge injection at the ITO/EEL, and become less defined and eventually disappear as the temperature decreases. (similar tests on PM6:Y6 OSCs revealed similar ripples but at different voltages verifying their origins and dependence on the donor-acceptor system). As, at the lower temperatures, current flow across the device becomes more limited by charge injection at the contacts than by transport across the donor-acceptor layer, these ripples disappear. The larger decrease in current in the ZnO-EEL OSC vs. the Histidine-EEL OSC as the temperature decreases from 140 K to 100 K therefore points to a stronger temperature-dependent electron injection behavior at the ITO/ZnO contact relative to the Histidine/ITO contact. This limitation can be attributed to ZnO surface states [171], which can act as charge traps. Because charge de-trapping will necessarily be more difficult at the lower temperatures, the current flow drops precipitously in these devices. For easier comparison, the dark  $J$ - $V$  characteristics of the control and UV-irradiated

OSCs at  $T = 140$  K and  $T = 300$  K are presented together in **Figure 7.8.e**. It can be seen that the UV-irradiated and dark control Histidine-EEL OSCs have almost similar characteristics for both temperatures, which is not surprising given their high photostability and minimal changes after the UV irradiation observed above. In contrast, the UV-irradiated ZnO-EEL OSC shows a significantly lower current relative to its dark control at 140K (where the characteristics are governed by charge injection at the contacts). The current was however similar in both devices at 300 K (where the characteristics are not dominated by charge injection at the contacts). The lower current at 140 K in the UV-irradiated cells suggests a possible increase in ZnO surface states and charge trapping after the UV irradiation. Under the normal operating conditions of OSCs, the increased charge trapping may reduce the hole-blocking functionality of the ITO/ZnO contact and thereby increase surface recombination due to one of two mechanisms: i) a shift in contact WF allowing undesired extraction of photogenerated holes across the ITO/ZnO contact, or ii) increased recombination with photogenerated holes. In this context, using the DM-EELs helps avoid this issue not only because they allow eliminating the ZnO layer but also because they provide a directional dipole moment that helps maintain charge selectivity independent of any UV-induced contact WF shifts. As a result, using DM-EELs prevents UV-mediated increase in surface recombination (as concluded earlier from **Figure 7.4**) and helps maintain PCE stability.

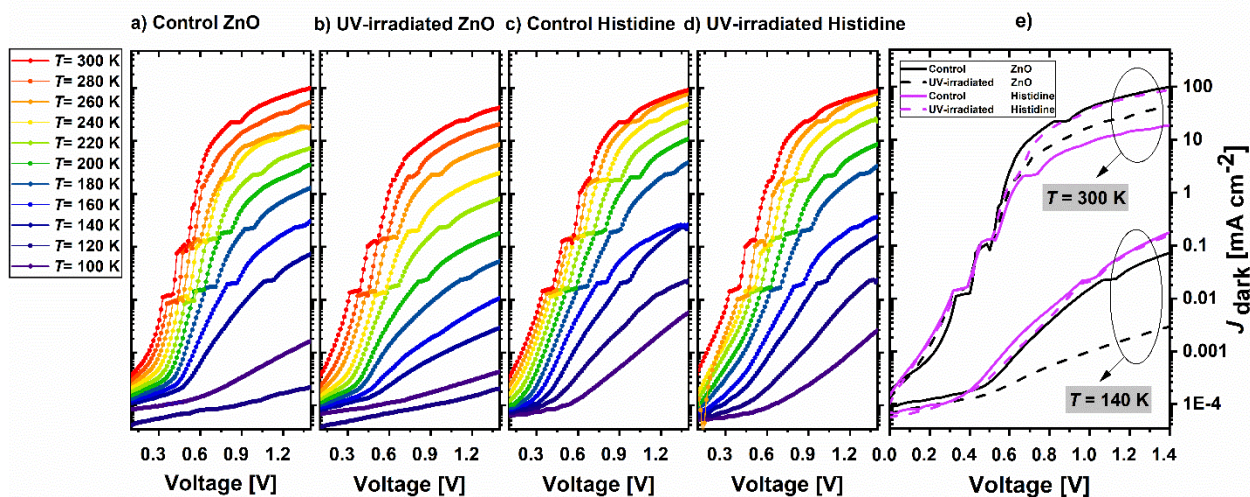


**Figure 7. 8.** Dark  $J$ - $V$  characteristics of the UV-irradiated and dark control P3HT:PC60BM OSCs with ZnO (a & b) and Histidine (c & d) EELs, measured at different temperatures. The  $T = 140$  K and  $T = 300$  K characteristics are presented together in (e) to facilitate comparison.

The Schottky thermionic-emission model for semiconductor-metal junctions,  $j_0 = j_{00} \exp(-E_{ac}/n_d k_B T)$ , where  $j_0$  represents the dark saturation current density, and  $j_{00}$  coefficient depends on the material system, allows extracting activation energy ( $E_{ac}$ ) from the dark  $J$ - $V$  characteristics. [172, 173]. **Figure 7.9** displays the  $n_d \ln(j_0)$  versus  $1/k_B T$  plots over the 200-300 K range based on the data in **Figure 7.8**. Lower temperatures were excluded due to the detrimental effect of the higher resistances on data reliability. From the slope of the fits, the  $E_{ac}$  in the dark control Histidine-EEL OSC and its UV-irradiated counterpart is estimated at 0.75 eV and 0.87 eV, respectively. The ZnO-EEL OSCs exhibit activation energy of 0.76 eV (for the dark control cells), consistent with reported values [174], versus 1.68 eV (for UV-irradiated cells). The higher activation energy in these cells is consistent with increased charge trapping and/or WF shifts due to the UV irradiation.

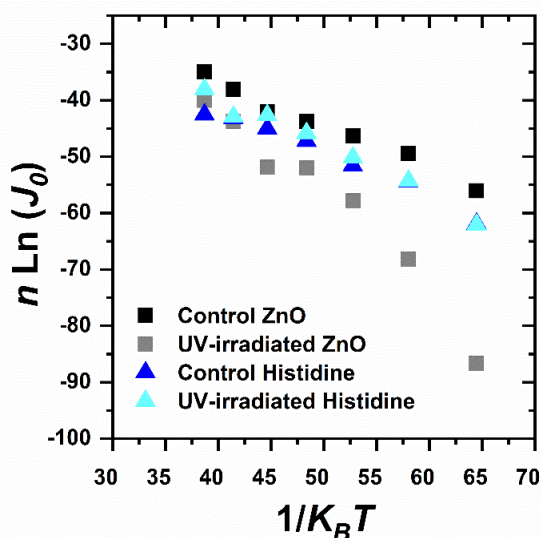


**Figure 7. 9.**  $n_d \ln (J_0)$  versus  $1/K_B T$  plots, extracted from the dark  $J$ - $V$  characteristics in Figure 7.8.

### 7.3 Conclusion

In summary, results illustrate that using molecules with large dipole moments like Histidine or Sarcosine instead of the commonly used ZnO EEL can significantly enhance the stability of inverted OSCs. Tests on OSCs with P3HT:PC60BM and PM6:Y6 as donor-acceptor systems show that while the dominant degradation mechanism is different in each case (photoinduced degradation in the first

versus temporal degradation in the second), using DM-EELs substantially suppresses degradation and enhances stability in both cases. The voltage-dependent ideality factor characteristics and low-temperature electrical measurements show that using DM-EELs not only allows eliminating the ZnO layer and circumventing the charge trapping and increased surface recombination issue but also provides a directional dipole moment that helps maintain charge selectivity independent of any UV-induced contact WF shifts. The results show that using green-solvent processable materials with large dipole moments as EELs can provide a universal route for enhancing the stability of inverted organic solar cells.

## Chapter 8

### Summary of Main Conclusions and Suggestions for Future Work

#### 8.1 Summary of Main Conclusions

The research described in this thesis has investigated the effect of EELs in inverted OSCs' intrinsic photostability by (i) studying ZnO, the most commonly used EEL (as a reference cell), (ii) modifying ZnO EELs, and (iii) replacing ZnO EELs with alternatives.

The investigations on ZnO show that the ITO/ZnO and ZnO/BHJ interfaces both adversely influence photostability. Results reveal that the contact photodegradation is primarily due to UV-induced changes in the ITO and ITO/ZnO surface potential while they are morphologically stable. Finding from XPS measurements point to the UV-induced losses of the chemisorbed oxygen on the ITO surface, causing its WF reduction and thus contact selectivity loss. Regarding the ZnO/BHJ interface, surface defects of ZnO and UV-induced increased charge trapping at these defects reduce the electron selectivity of the ITO/ZnO contact and thereby increase surface recombination. Subsequently, OSCs with ZnO EELs exhibit a UV-induced transition in a dominant recombination mechanism, from trap-assisted recombination in the active-layer bulk to surface recombination at the ZnO/BHJ interface, resulting in low device photostability.

The work on modifying ZnO EELs investigates the effects of adding amine-containing materials (PEI or PDIN-H) in them either mixed with the ZnO or in a separate layer on photostability. Results show that mixing ZnO with PEI yields a 5x higher PCE stability under continuous UV irradiation. As verified by XPS measurements, the stability enhancement is associated with chemical interactions between PEI and ITO at the ITO/ZnO:PEI interface. The new chemical interface forms a more electronically stable contact that is less susceptible to UV-induced changes in surface potential (or WF). Using PDIN-H in a separate layer substantially increases photostability compared to the reference cells with ZnO, leading to a respective  $T_{80}$  of  $\geq 780$  h versus only  $\sim 124$  h. Results from HODs and UPS reveal that the passivation of ZnO surface defects by PDIN-H suppresses the increased surface recombination under UV and thereby enhances photostability.

The studies on replacing the ZnO EEL with alternatives involve pursuing large dipole moment materials, both polymeric (PEI) or small molecular (Histidine and Sarcosine) as single layer EELs

(DM-EELs). Results show that using PEI EELs maintains the hole-blocking properties of the contact even after UV stress and, as a result, suppresses the UV-induced increase in surface recombination observed in the ZnO cells. The findings provide direct evidence that maintaining the charge selectivity of contacts upon UV irradiation is critical for preventing surface recombination and improving device photostability. Using Histidine and Sarcosine EELs helps avoid the issue of UV-induced trap states at the ZnO and resultant charge trapping at these states by eliminating the ZnO layer and by maintaining charge selectivity. Stability results illustrate that while the dominant degradation mechanism depends on the donor-acceptor system (photoinduced degradation in P3HT:PC60BM versus temporal degradation in PM6:Y6), using DM-EELs substantially suppresses degradation and enhances stability in both cases. Overall, this thesis not only sheds light on specific root causes of the limited photostability of OSCs but also investigates approaches to mitigating their effects.

## 8.2 Suggestions for Future Work

The results here indicate the benefits of dipole interlayers for OSC stability. Investigating materials with different magnitudes of dipole moments may be a further promising pathway to improving device stability.

The low-temperature study in this thesis provides insights into almost unaffected defect states (if they exist) of DM-EELs before and after UV irradiation. Further investigations are encouraged to achieve a complete picture of DM-EELs. Employing various characterization techniques that study the physical and chemical aspects of interfacial dipole layers, their chemical structure, defects, and dynamic evolution at interfaces can yield more quantitative information.

Knowing that molecules with large dipole moments enhance intrinsic stability, it would be useful to explore alternative ways to induce surface polarity on the ITO surface and investigate its possible influences on contact selectivity. Since the ITO electrode suffers from hole leakage and its increase upon UV irradiation (as discussed in Chapter 2 and 6), an appropriate polarity of the ITO surface may help to form a depletion layer of holes in the vicinity of the ITO. As a result, hole leakage can be suppressed, and contact selectivity can be maintained, even after UV irradiation. This approach may eliminate the need for EEL and result in EEL-free OSCs, lowering manufacturing complexity.

As discussed in Chapter 7, incompatibilities between the electron and hole extraction layers sometimes result in degradation. If, indeed, this is one limiting factor in OSC stability, then it may be valuable to explore a variety of DM-EEL and HEL combinations as the next step.

It is known that many air-born molecules can find their ways toward the air-processed EELs; these molecules can be activated during photostability tests and affect photodegradation, as illustrated by the loss of chemisorbed oxygen on the ITO surface in Chapter 4. Therefore, it would be valuable to further investigate the possible effect of pre-absorbed air-born molecules on ITO and ITO/EELs by annealing them at high temperatures or by passivating them using fluorine or H<sub>2</sub> plasma.

## Bibliography

- [1] T. Heumueller, "Impact of Microstructure on the Photostability of Organic Bulk Heterojunction Solar Cells," 2016.
- [2] M. Victoria, N. Haegel, I. M. Peters, R. Sinton, A. Jäger-Waldau, C. del Cañizo, *et al.*, "Solar photovoltaics is ready to power a sustainable future," *Joule*, 2021.
- [3] F. C. Krebs, *Stability and degradation of organic and polymer solar cells*: John Wiley & Sons, 2012.
- [4] D. M. Chapin, C. S. Fuller, and G. L. Pearson, "A new silicon p-n junction photocell for converting solar radiation into electrical power," *Journal of applied physics*, vol. 25, pp. 676-677, 1954.
- [5] S. Battersby, "News Feature: The solar cell of the future," *Proceedings of the National Academy of Sciences*, vol. 116, pp. 7-10, 2019.
- [6] NREL. Best Research-Cell Efficiency Chart [Online]. Available: <https://www.nrel.gov/pv/cell-efficiency.html> [Accessed: Jun 15, 2021]
- [7] F. C. Krebs, "Fabrication and processing of polymer solar cells: A review of printing and coating techniques," *Solar energy materials and solar cells*, vol. 93, pp. 394-412, 2009.
- [8] G. Li, R. Zhu, and Y. Yang, "Polymer solar cells," *Nature photonics*, vol. 6, pp. 153-161, 2012.
- [9] S. Venkatesan, Q. Chen, E. C. Ngo, N. Adhikari, K. Nelson, A. Dubey, *et al.*, "Polymer solar cells processed using anisole as a relatively nontoxic solvent," *Energy Technology*, vol. 2, pp. 269-274, 2014.
- [10] T. Aernouts, T. Aleksandrov, C. Girotto, J. Genoe, and J. Poortmans, "Polymer based organic solar cells using ink-jet printed active layers," *Applied Physics Letters*, vol. 92, p. 22, 2008.
- [11] E. Ngo, S. Venkatesan, and Q. Qiao, "Polymer photovoltaics with top metal electrode deposited by solution-processing," *IEEE Transactions on Electron Devices*, vol. 61, pp. 2957-2962, 2014.
- [12] G. Chamberlain, "Organic solar cells: A review," *Solar cells*, vol. 8, pp. 47-83, 1983.
- [13] C. W. Tang, "Two-layer organic photovoltaic cell," *Applied physics letters*, vol. 48, pp. 183-185, 1986.
- [14] Y. Lin, B. Adilbekova, Y. Firdaus, E. Yengel, H. Faber, M. Sajjad, *et al.*, "17% Efficient organic solar cells based on liquid exfoliated WS<sub>2</sub> as a replacement for PEDOT: PSS," *Advanced materials*, vol. 31, p. 1902965, 2019.
- [15] C. K. Chiang, C. Fincher Jr, Y. W. Park, A. J. Heeger, H. Shirakawa, E. J. Louis, *et al.*, "Electrical conductivity in doped polyacetylene," *Physical review letters*, vol. 39, p. 1098, 1977.
- [16] J. D. Myers and J. Xue, "Organic semiconductors and their applications in photovoltaic devices," *Polymer Reviews*, vol. 52, pp. 1-37, 2012.
- [17] J.-P. Sun, "ORGANIC PHOTOVOLTAICS: INTEGRATING NON-FULLERENE ACCEPTORS INTO SOLUTION-PROCESSED DEVICES," 2017.
- [18] M. L. P. Junior, R. T. de Sousa Júnior, G. M. e Silva, and L. A. R. Júnior, "Stationary polaron properties in organic crystalline semiconductors," *Physical Chemistry Chemical Physics*, vol. 21, pp. 2727-2733, 2019.
- [19] P. Berger and M. Kim, "Polymer solar cells: P3HT: PCBM and beyond," *Journal of Renewable and Sustainable Energy*, vol. 10, p. 013508, 2018.
- [20] C. Zhang, Y. S. Zhao, and J. Yao, "Organic composite nanomaterials: energy transfers and tunable luminescent behaviors," *New Journal of Chemistry*, vol. 35, pp. 973-978, 2011.



- [21] O. Mikhnenko, F. Cordella, A. Sieval, J. Hummelen, P. Blom, and M. Loi, "Temperature dependence of exciton diffusion in conjugated polymers," *The Journal of Physical Chemistry B*, vol. 112, pp. 11601-11604, 2008.
- [22] M. Rita Narayan and J. Singh, "Study of the mechanism and rate of exciton dissociation at the donor-acceptor interface in bulk-heterojunction organic solar cells," *Journal of Applied Physics*, vol. 114, p. 073510, 2013.
- [23] C. Deibel and V. Dyakonov, "Polymer–fullerene bulk heterojunction solar cells," *Reports on Progress in Physics*, vol. 73, p. 096401, 2010.
- [24] O. V. Mikhnenko, P. W. Blom, and T.-Q. Nguyen, "Exciton diffusion in organic semiconductors," *Energy & Environmental Science*, vol. 8, pp. 1867-1888, 2015.
- [25] G. Yu, J. Gao, J. C. Hummelen, F. Wudl, and A. J. Heeger, "Polymer photovoltaic cells: enhanced efficiencies via a network of internal donor-acceptor heterojunctions," *Science*, vol. 270, pp. 1789-1791, 1995.
- [26] S. Mohd-Nasir, M. Sulaiman, N. Ahmad-Ludin, M. Ibrahim, K. Sopian, and M. Mat-Teridi, "Review of polymer, dye-sensitized, and hybrid solar cells," *International Journal of Photoenergy*, vol. 2014, 2014.
- [27] M. T. Dang, L. Hirsch, and G. Wantz, "P3HT: PCBM, best seller in polymer photovoltaic research," ed: Wiley Online Library, 2011.
- [28] Y. Q. Wong, H. Y. Wong, C. S. Tan, and H.-F. Meng, "Performance optimization of organic solar cells," *IEEE Photonics Journal*, vol. 6, pp. 1-26, 2014.
- [29] Y. Tong, Z. Xiao, X. Du, C. Zuo, Y. Li, M. Lv, *et al.*, "Progress of the key materials for organic solar cells," *Science China Chemistry*, vol. 63, pp. 758-765, 2020.
- [30] Y. Qin, M. A. Uddin, Y. Chen, B. Jang, K. Zhao, Z. Zheng, *et al.*, "Highly Efficient Fullerene-Free Polymer Solar Cells Fabricated with Polythiophene Derivative," *Advanced Materials*, vol. 28, pp. 9416-9422, 2016.
- [31] M. Zhang, X. Guo, W. Ma, H. Ade, and J. Hou, "A large-bandgap conjugated polymer for versatile photovoltaic applications with high performance," *Advanced Materials*, vol. 27, pp. 4655-4660, 2015.
- [32] Y. Han, H. Dong, W. Pan, B. Liu, X. Chen, R. Huang, *et al.*, "An Efficiency of 16.46% and a T 80 Lifetime of Over 4000 h for the PM6: Y6 Inverted Organic Solar Cells Enabled by Surface Acid Treatment of the Zinc Oxide Electron Transporting Layer," *ACS Applied Materials & Interfaces*, 2021.
- [33] J. Yuan, Y. Zhang, L. Zhou, G. Zhang, H.-L. Yip, T.-K. Lau, *et al.*, "Single-junction organic solar cell with over 15% efficiency using fused-ring acceptor with electron-deficient core," *Joule*, vol. 3, pp. 1140-1151, 2019.
- [34] Q. Guo, Q. Guo, Y. Geng, A. Tang, M. Zhang, M. Du, *et al.*, "Recent advances in PM6: Y6-based organic solar cells," *Materials Chemistry Frontiers*, 2021.
- [35] S. Chen, J. R. Manders, S.-W. Tsang, and F. So, "Metal oxides for interface engineering in polymer solar cells," *Journal of Materials Chemistry*, vol. 22, pp. 24202-24212, 2012.
- [36] W. Chen, M. P. Nikiforov, and S. B. Darling, "Morphology characterization in organic and hybrid solar cells," *Energy & Environmental Science*, vol. 5, pp. 8045-8074, 2012.
- [37] E. L. Ratcliff, B. Zacher, and N. R. Armstrong, "Selective interlayers and contacts in organic photovoltaic cells," *The Journal of Physical Chemistry Letters*, vol. 2, pp. 1337-1350, 2011.
- [38] H.-L. Yip and A. K.-Y. Jen, "Recent advances in solution-processed interfacial materials for efficient and stable polymer solar cells," *Energy & Environmental Science*, vol. 5, pp. 5994-6011, 2012.
- [39] Q. Chen, C. Wang, Y. Li, and L. Chen, "Interfacial Dipole in Organic and Perovskite Solar Cells," *Journal of the American Chemical Society*, vol. 142, pp. 18281-18292, 2020.

- [40] M. T. Greiner, L. Chai, M. G. Helander, W. M. Tang, and Z. H. Lu, "Transition metal oxide work functions: the influence of cation oxidation state and oxygen vacancies," *Advanced Functional Materials*, vol. 22, pp. 4557-4568, 2012.
- [41] X. Xu, J. Xiao, G. Zhang, L. Wei, X. Jiao, H.-L. Yip, *et al.*, "Interface-enhanced organic solar cells with extrapolated T80 lifetimes of over 20 years," *Science Bulletin*, vol. 65, pp. 208-216, 2020.
- [42] J. F. Butscher, S. Intorp, J. Kress, Q. An, Y. J. Hofstetter, N. Hippchen, *et al.*, "Enhancing the open-circuit voltage of perovskite solar cells by embedding molecular dipoles within their hole-blocking layer," *ACS applied materials & interfaces*, vol. 12, pp. 3572-3579, 2019.
- [43] G. Williams and H. Aziz, "The effect of charge extraction layers on the photo-stability of vacuum-deposited versus solution-coated organic solar cells," *Organic Electronics*, vol. 15, pp. 47-56, 2014.
- [44] Q. Wang, G. Williams, T. Tsui, and H. Aziz, "Photochemical deterioration of the organic/metal contacts in organic optoelectronic devices," *Journal of Applied Physics*, vol. 112, p. 064502, 2012.
- [45] G. Williams, Q. Wang, and H. Aziz, "The photo-stability of polymer solar cells: Contact photo-degradation and the benefits of interfacial layers," *Advanced Functional Materials*, vol. 23, pp. 2239-2247, 2013.
- [46] J.-H. Lee, S. Kwon, S. Y. Jeong, B. Park, S. Hong, J. Kim, *et al.*, "Enhanced p-Type Work Function Tunability Induced by Electrostatic Molecular Alignment and Surface Coverage in Conjugated Small-Molecule Electrolyte," *ACS Applied Electronic Materials*, vol. 1, pp. 2566-2573, 2019.
- [47] Z. Yin, J. Wei, and Q. Zheng, "Interfacial materials for organic solar cells: recent advances and perspectives," *Advanced Science*, vol. 3, p. 1500362, 2016.
- [48] Z. He, C. Zhong, S. Su, M. Xu, H. Wu, and Y. Cao, "Enhanced power-conversion efficiency in polymer solar cells using an inverted device structure," *Nature photonics*, vol. 6, pp. 591-595, 2012.
- [49] Y. Zhou, C. Fuentes-Hernandez, J. Shim, J. Meyer, A. J. Giordano, H. Li, *et al.*, "A universal method to produce low-work function electrodes for organic electronics," *Science*, vol. 336, pp. 327-332, 2012.
- [50] X. Guo, Q. Fan, J. Wu, G. Li, Z. Peng, W. Su, *et al.*, "Optimized active layer morphologies via ternary copolymerization of polymer donors for 17.6% efficiency organic solar cells with enhanced fill factor," *Angewandte Chemie International Edition*, vol. 60, pp. 2322-2329, 2021.
- [51] B. Qi and J. Wang, "Fill factor in organic solar cells," *Physical Chemistry Chemical Physics*, vol. 15, pp. 8972-8982, 2013.
- [52] S. Rafique, S. M. Abdullah, K. Sulaiman, and M. Iwamoto, "Fundamentals of bulk heterojunction organic solar cells: an overview of stability/degradation issues and strategies for improvement," *Renewable and Sustainable Energy Reviews*, vol. 84, pp. 43-53, 2018.
- [53] G. Wang, F. S. Melkonyan, A. Facchetti, and T. J. Marks, "All-Polymer Solar Cells: Recent Progress, Challenges, and Prospects," *Angewandte Chemie International Edition*, vol. 58, pp. 4129-4142, 2019.
- [54] P. Cheng and X. Zhan, "Stability of organic solar cells: challenges and strategies," *Chemical Society Reviews*, vol. 45, pp. 2544-2582, 2016.
- [55] S. Venkatesan, E. Ngo, D. Khatiwada, C. Zhang, and Q. Qiao, "Enhanced lifetime of polymer solar cells by surface passivation of metal oxide buffer layers," *ACS applied materials & interfaces*, vol. 7, pp. 16093-16100, 2015.

- [56] S. B. Sapkota, M. Fischer, B. Zimmermann, and U. Würfel, "Analysis of the degradation mechanism of ITO-free organic solar cells under UV radiation," *Solar energy materials and solar cells*, vol. 121, pp. 43-48, 2014.
- [57] J. Jeong, J. Seo, S. Nam, H. Han, H. Kim, T. D. Anthopoulos, *et al.*, "Significant stability enhancement in high-efficiency polymer: fullerene bulk heterojunction solar cells by blocking ultraviolet photons from solar light," *Advanced Science*, vol. 3, p. 1500269, 2016.
- [58] W. R. Mateker and M. D. McGehee, "Progress in understanding degradation mechanisms and improving stability in organic photovoltaics," *Advanced materials*, vol. 29, p. 1603940, 2017.
- [59] X. Xu, D. Li, J. Yuan, Y. Zhou, and Y. Zou, "Recent Advances in Stability of Organic Solar Cells," *EnergyChem*, p. 100046, 2020.
- [60] L. Duan and A. Uddin, "Progress in stability of organic solar cells," *Advanced Science*, vol. 7, p. 1903259, 2020.
- [61] F. Deschler, A. De Sio, E. Von Hauff, P. Kutka, T. Sauermaun, H. J. Egelhaaf, *et al.*, "The effect of ageing on exciton dynamics, charge separation, and recombination in P3HT/PCBM photovoltaic blends," *Advanced Functional Materials*, vol. 22, pp. 1461-1469, 2012.
- [62] C. H. Peters, I. Sachs-Quintana, W. R. Mateker, T. Heumueller, J. Rivnay, R. Noriega, *et al.*, "The mechanism of burn-in loss in a high efficiency polymer solar cell," *Advanced Materials*, vol. 24, pp. 663-668, 2012.
- [63] T. M. Clarke, C. Lungenschmied, J. Peet, N. Drolet, K. Sunahara, A. Furube, *et al.*, "Photodegradation in encapsulated silole-based polymer: PCBM solar cells investigated using transient absorption spectroscopy and charge extraction measurements," *Advanced Energy Materials*, vol. 3, pp. 1473-1483, 2013.
- [64] C. Wang, S. Ni, S. Braun, M. Fahlman, and X. Liu, "Effects of water vapor and oxygen on non-fullerene small molecule acceptors," *Journal of Materials Chemistry C*, vol. 7, pp. 879-886, 2019.
- [65] U. Aygül, H. Hintz, H.-J. Egelhaaf, A. Distler, S. Abb, H. Peisert, *et al.*, "Energy level alignment of a P3HT/fullerene blend during the initial steps of degradation," *The Journal of Physical Chemistry C*, vol. 117, pp. 4992-4998, 2013.
- [66] A. Kumar, R. Devine, C. Mayberry, B. Lei, G. Li, and Y. Yang, "Origin of radiation-induced degradation in polymer solar cells," *Advanced Functional Materials*, vol. 20, pp. 2729-2736, 2010.
- [67] K. Kawano and C. Adachi, "Evaluating carrier accumulation in degraded bulk heterojunction organic solar cells by a thermally stimulated current technique," *Advanced Functional Materials*, vol. 19, pp. 3934-3940, 2009.
- [68] S. Rafique, S. M. Abdullah, N. Badiei, J. McGettrick, K. T. Lai, N. A. Roslan, *et al.*, "An insight into the air stability of the benchmark polymer: fullerene photovoltaic films and devices: A comparative study," *Organic Electronics*, vol. 76, p. 105456, 2020.
- [69] Z. Kam, X. Wang, J. Zhang, and J. Wu, "Elimination of burn-in open-circuit voltage degradation by ZnO surface modification in organic solar cells," *ACS applied materials & interfaces*, vol. 7, pp. 1608-1615, 2015.
- [70] S. K. Hau, H.-L. Yip, N. S. Baek, J. Zou, K. O'Malley, and A. K.-Y. Jen, "Air-stable inverted flexible polymer solar cells using zinc oxide nanoparticles as an electron selective layer," *Applied Physics Letters*, vol. 92, p. 225, 2008.
- [71] C. Waldauf, M. Morana, P. Denk, P. Schilinsky, K. Coakley, S. Choulis, *et al.*, "Highly efficient inverted organic photovoltaics using solution based titanium oxide as electron selective contact," *Applied physics letters*, vol. 89, p. 233517, 2006.

- [72] W. R. Mateker, T. Heumueller, R. Cheacharoen, I. Sachs-Quintana, M. D. McGehee, J. Warnan, *et al.*, "Molecular packing and arrangement govern the photo-oxidative stability of organic photovoltaic materials," *Chemistry of Materials*, vol. 27, pp. 6345-6353, 2015.
- [73] Y. W. Soon, S. Shoaee, R. S. Ashraf, H. Bronstein, B. C. Schroeder, W. Zhang, *et al.*, "Material crystallinity as a determinant of triplet dynamics and oxygen quenching in donor polymers for organic photovoltaic devices," *Advanced Functional Materials*, vol. 24, pp. 1474-1482, 2014.
- [74] H. Hintz, H.-J. Egelhaaf, L. Lüer, J. Hauch, H. Peisert, and T. Chassé, "Photodegradation of P3HT– a systematic study of environmental factors," *Chemistry of Materials*, vol. 23, pp. 145-154, 2011.
- [75] Y. Wang, J. Lee, X. Hou, C. Labanti, J. Yan, E. Mazzolini, *et al.*, "Recent Progress and Challenges toward Highly Stable Nonfullerene Acceptor-Based Organic Solar Cells," *Advanced Energy Materials*, vol. 11, p. 2003002, 2021.
- [76] J. Guo, Y. Wu, R. Sun, W. Wang, J. Guo, Q. Wu, *et al.*, "Suppressing photo-oxidation of non-fullerene acceptors and their blends in organic solar cells by exploring material design and employing friendly stabilizers," *Journal of Materials Chemistry A*, vol. 7, pp. 25088-25101, 2019.
- [77] J. Wang, J. Peng, X. Liu, and Z. Liang, "Efficient and stable ternary organic solar cells based on two planar nonfullerene acceptors with tunable crystallinity and phase miscibility," *ACS applied materials & interfaces*, vol. 9, pp. 20704-20710, 2017.
- [78] M. Xiao, K. Zhang, S. Dong, Q. Yin, Z. Liu, L. Liu, *et al.*, "High-performance ternary nonfullerene polymer solar cells with both improved photon harvesting and device stability," *ACS applied materials & interfaces*, vol. 10, pp. 25594-25603, 2018.
- [79] N. Y. Doumon, F. V. Houard, J. Dong, P. Christodoulis, M. V. Dryzhov, G. Portale, *et al.*, "Improved photostability in ternary blend organic solar cells: the role of [70] PCBM," *Journal of Materials Chemistry C*, vol. 7, pp. 5104-5111, 2019.
- [80] T. Nguyen, J. Ip, P. Jolinat, and P. Destruel, "XPS and sputtering study of the Alq3/electrode interfaces in organic light emitting diodes," *Applied surface science*, vol. 172, pp. 75-83, 2001.
- [81] I. Cardinaletti, J. Kesters, S. Bertho, B. Conings, F. Piersimoni, J. D'Haen, *et al.*, "Toward bulk heterojunction polymer solar cells with thermally stable active layer morphology," *Journal of Photonics for Energy*, vol. 4, p. 040997, 2014.
- [82] C. H. Peters, I. Sachs-Quintana, J. P. Kastrop, S. Beaupre, M. Leclerc, and M. D. McGehee, "High efficiency polymer solar cells with long operating lifetimes," *Advanced Energy Materials*, vol. 1, pp. 491-494, 2011.
- [83] R. Roesch, K.-R. Eberhardt, S. Engmann, G. Gobsch, and H. Hoppe, "Polymer solar cells with enhanced lifetime by improved electrode stability and sealing," *Solar energy materials and solar cells*, vol. 117, pp. 59-66, 2013.
- [84] Q. Liu, J. Toudert, F. Liu, P. Mantilla-Perez, M. M. Bajo, T. P. Russell, *et al.*, "Circumventing UV Light Induced Nanomorphology Disorder to Achieve Long Lifetime PTB7-Th: PCBM Based Solar Cells," *Advanced Energy Materials*, vol. 7, p. 1701201, 2017.
- [85] M. Prosa, M. Tessarolo, M. Bolognesi, O. Margeat, D. Gedefaw, M. Gaceur, *et al.*, "Enhanced ultraviolet stability of air-processed polymer solar cells by Al doping of the ZnO interlayer," *ACS applied materials & interfaces*, vol. 8, pp. 1635-1643, 2016.
- [86] A. Tournebize, G. Mattana, T. r. s. Gorisse, A. Bousquet, G. Wantz, L. Hirsch, *et al.*, "Crucial role of the electron transport layer and UV light on the open-circuit voltage loss in inverted organic solar cells," *ACS applied materials & interfaces*, vol. 9, pp. 34131-34138, 2017.

- [87] M. Reese, A. Sigdel, J. Berry, D. Ginley, and S. Shaheen, "A simple miniature controlled-atmosphere chamber for optoelectronic characterizations," *Solar Energy Materials and Solar Cells*, vol. 94, pp. 1254-1258, 2010.
- [88] S. A. Gevorgyan, M. Jørgensen, F. C. Krebs, and K. O. Sylvester-Hvid, "A compact multi-chamber setup for degradation and lifetime studies of organic solar cells," *Solar energy materials and solar cells*, vol. 95, pp. 1389-1397, 2011.
- [89] Q. Burlingame, X. Tong, J. Hankett, M. Slocus, Z. Chen, and S. R. Forrest, "Photochemical origins of burn-in degradation in small molecular weight organic photovoltaic cells," *Energy & Environmental Science*, vol. 8, pp. 1005-1010, 2015.
- [90] N. Wang, X. Tong, Q. Burlingame, J. Yu, and S. R. Forrest, "Photodegradation of small-molecule organic photovoltaics," *Solar energy materials and solar cells*, vol. 125, pp. 170-175, 2014.
- [91] A. Distler, T. Sauermann, H. J. Egelhaaf, S. Rodman, D. Waller, K. S. Cheon, *et al.*, "The effect of PCBM dimerization on the performance of bulk heterojunction solar cells," *Advanced Energy Materials*, vol. 4, p. 1300693, 2014.
- [92] T. Heumueller, W. R. Mateker, A. Distler, U. F. Fritze, R. Cheacharoen, W. H. Nguyen, *et al.*, "Morphological and electrical control of fullerene dimerization determines organic photovoltaic stability," *Energy & Environmental Science*, vol. 9, pp. 247-256, 2016.
- [93] N. Y. Doumon, M. V. Dryzhov, F. I. V. Houard, V. M. Le Corre, A. Rahimi Chatri, P. Christodoulis, *et al.*, "Photostability of fullerene and non-fullerene polymer solar cells: the role of the acceptor," *ACS applied materials & interfaces*, vol. 11, pp. 8310-8318, 2019.
- [94] T. Heumueller, W. R. Mateker, I. Sachs-Quintana, K. Vandewal, J. A. Bartelt, T. M. Burke, *et al.*, "Reducing burn-in voltage loss in polymer solar cells by increasing the polymer crystallinity," *Energy & Environmental Science*, vol. 7, pp. 2974-2980, 2014.
- [95] G. Williams and H. Aziz, "Insights into electron and hole extraction layers for upright and inverted vacuum-deposited small molecule organic solar cells," in *Organic Photovoltaics XIV*, 2013, p. 88301V.
- [96] A. Manor, E. A. Katz, T. Tromholt, and F. C. Krebs, "Electrical and Photo-Induced Degradation of ZnO Layers in Organic Photovoltaics," *Advanced Energy Materials*, vol. 1, pp. 836-843, 2011.
- [97] Y. Zhou, J. W. Shim, C. Fuentes-Hernandez, A. Sharma, K. A. Knauer, A. J. Giordano, *et al.*, "Direct correlation between work function of indium-tin-oxide electrodes and solar cell performance influenced by ultraviolet irradiation and air exposure," *Physical Chemistry Chemical Physics*, vol. 14, pp. 12014-12021, 2012.
- [98] N. Gasparini, M. Salvador, S. Strohm, T. Heumueller, I. Levchuk, A. Wadsworth, *et al.*, "Burn-in Free Nonfullerene-Based Organic Solar Cells," *Advanced Energy Materials*, vol. 7, p. 1700770, 2017.
- [99] S. Park and H. J. Son, "Intrinsic photo-degradation and mechanism of polymer solar cells: the crucial role of non-fullerene acceptors," *Journal of Materials Chemistry A*, vol. 7, pp. 25830-25837, 2019.
- [100] J. Xiao, M. Ren, G. Zhang, J. Wang, D. Zhang, L. Liu, *et al.*, "An operando study on the photostability of nonfullerene organic solar cells," *Solar Rrl*, vol. 3, p. 1900077, 2019.
- [101] X. Du, T. Heumueller, W. Gruber, A. Classen, T. Unruh, N. Li, *et al.*, "Efficient polymer solar cells based on non-fullerene acceptors with potential device lifetime approaching 10 years," *Joule*, vol. 3, pp. 215-226, 2019.
- [102] Y. Jiang, L. Sun, F. Jiang, C. Xie, L. Hu, X. Dong, *et al.*, "Photocatalytic effect of ZnO on the stability of nonfullerene acceptors and its mitigation by SnO<sub>2</sub> for nonfullerene organic solar cells," *Materials Horizons*, vol. 6, pp. 1438-1443, 2019.

- [103] N. Y. Doumon, F. V. Houard, J. Dong, H. Yao, G. Portale, J. Hou, *et al.*, "Energy level modulation of ITIC derivatives: Effects on the photodegradation of conventional and inverted organic solar cells," *Organic Electronics*, vol. 69, pp. 255-262, 2019.
- [104] Q. Liu, P. Mantilla-Perez, M. Montes Bajo, P. Romero-Gomez, and J. Martorell, "UV-induced oxygen removal for photostable, high-efficiency PTB7-th: PC71bm photovoltaic cells," *ACS applied materials & interfaces*, vol. 8, pp. 28750-28756, 2016.
- [105] E. Polydorou, I. Sakellis, A. Soultati, A. Kaltzoglou, T. A. Papadopoulos, J. Briscoe, *et al.*, "Avoiding ambient air and light induced degradation in high-efficiency polymer solar cells by the use of hydrogen-doped zinc oxide as electron extraction material," *Nano Energy*, vol. 34, pp. 500-514, 2017.
- [106] J. Li, F. Qin, W. Zeng, L. Sun, W. Wang, and Y. Zhou, "N-doping of fullerene using 1, 3, 5-trimethylhexahydro-1, 3, 5-triazine as an electron transport layer for nonfullerene organic solar cells," *Sustainable Energy & Fuels*, vol. 4, pp. 1984-1990, 2020.
- [107] S. Zappia, G. Scavia, A. M. Ferretti, U. Giovanella, V. Vohra, and S. Destri, "Water-Processable Amphiphilic Low Band Gap Block Copolymer: Fullerene Blend Nanoparticles as Alternative Sustainable Approach for Organic Solar Cells," *Advanced Sustainable Systems*, vol. 2, p. 1700155, 2018.
- [108] Y. Huang and C. K. Luscombe, "Towards green synthesis and processing of organic solar cells," *The Chemical Record*, vol. 19, pp. 1039-1049, 2019.
- [109] H. Liu, Z. X. Liu, S. Wang, J. Huang, H. Ju, Q. Chen, *et al.*, "Boosting organic-metal oxide heterojunction via conjugated small molecules for efficient and stable nonfullerene polymer solar cells," *Advanced Energy Materials*, vol. 9, p. 1900887, 2019.
- [110] S. Trost, T. Becker, A. Polywka, P. Görrn, M. F. Oszajca, N. A. Luechinger, *et al.*, "Avoiding Photoinduced Shunts in Organic Solar Cells by the Use of Tin Oxide (SnO<sub>x</sub>) as Electron Extraction Material Instead of ZnO," *Advanced Energy Materials*, vol. 6, p. 1600347, 2016.
- [111] X. Crispin, "Interface dipole at organic/metal interfaces and organic solar cells," *Solar Energy Materials and Solar Cells*, vol. 83, pp. 147-168, 2004.
- [112] S. Ohisa, D. Takashima, T. Chiba, and J. Kido, "Low-temperature cross-linking of polyethyleneimine ethoxylated using silane coupling agents to obtain stable electron injection layers in solution-processed organic light-emitting devices," *Journal of Materials Chemistry C*, vol. 7, pp. 6759-6766, 2019.
- [113] S. Zhang, L. Ye, H. Zhang, and J. Hou, "Green-solvent-processable organic solar cells," *Materials Today*, vol. 19, pp. 533-543, 2016.
- [114] E. Zojer, T. C. Taucher, and O. T. Hofmann, "The impact of dipolar layers on the electronic properties of organic/inorganic hybrid interfaces," *Advanced Materials Interfaces*, vol. 6, p. 1900581, 2019.
- [115] J.-H. Lee, J. Kim, G. Kim, D. Shin, S. Y. Jeong, J. Lee, *et al.*, "Introducing paired electric dipole layers for efficient and reproducible perovskite solar cells," *Energy & Environmental Science*, vol. 11, pp. 1742-1751, 2018.
- [116] F. A. Nüesch, "Interface Dipoles for Tuning Energy Level Alignment in Organic Thin Film Devices," *CHIMIA International Journal for Chemistry*, vol. 67, pp. 796-803, 2013.
- [117] S. Kundu, S. R. Gollu, R. Sharma, G. Srinivas, A. Ashok, A. Kulkarni, *et al.*, "Device stability of inverted and conventional bulk heterojunction solar cells with MoO<sub>3</sub> and ZnO nanoparticles as charge transport layers," *Organic Electronics*, vol. 14, pp. 3083-3088, 2013.
- [118] A. Mumyatov, F. Prudnov, L. Inasaridze, O. Mukhacheva, and P. Troshin, "High LUMO energy pyrrolidinofullerenes as promising electron-acceptor materials for organic solar cells," *Journal of Materials Chemistry C*, vol. 3, pp. 11612-11617, 2015.

- [119] S. Zhang, Y. Qin, J. Zhu, and J. Hou, "Over 14% efficiency in polymer solar cells enabled by a chlorinated polymer donor," *Advanced Materials*, vol. 30, p. 1800868, 2018.
- [120] E. Kymakis, N. Kornilios, and E. Koudoumas, "Carbon nanotube doping of P3HT: PCBM photovoltaic devices," *Journal of Physics D: Applied Physics*, vol. 41, p. 165110, 2008.
- [121] Y. Sun, J. H. Seo, C. J. Takacs, J. Seifert, and A. J. Heeger, "Inverted polymer solar cells integrated with a low-temperature-annealed sol-gel-derived ZnO film as an electron transport layer," *Advanced Materials*, vol. 23, pp. 1679-1683, 2011.
- [122] A. D. Hendsbee, J.-P. Sun, W. K. Law, H. Yan, I. G. Hill, D. M. Spasyuk, *et al.*, "Synthesis, self-assembly, and solar cell performance of N-annulated perylene diimide non-fullerene acceptors," *Chemistry of Materials*, vol. 28, pp. 7098-7109, 2016.
- [123] U. Würfel, M. Seßler, M. Unmüssig, N. Hofmann, M. List, E. Mankel, *et al.*, "How Molecules with Dipole Moments Enhance the Selectivity of Electrodes in Organic Solar Cells - A Combined Experimental and Theoretical Approach," *Advanced Energy Materials*, vol. 6, p. 1600594, 2016.
- [124] G. J. A. Wetzelaer, M. Kuik, and P. W. Blom, "Identifying the nature of charge recombination in organic solar cells from charge-transfer state electroluminescence," *Advanced Energy Materials*, vol. 2, pp. 1232-1237, 2012.
- [125] A. Kyaw, X. Sun, C. Jiang, G. Lo, D. Zhao, and D. Kwong, "An inverted organic solar cell employing a sol-gel derived ZnO electron selective layer and thermal evaporated MoO<sub>3</sub> hole selective layer," *Applied Physics Letters*, vol. 93, p. 221107, 2008.
- [126] T. Kirchartz, B. E. Pieters, K. Taretto, and U. Rau, "Mobility dependent efficiencies of organic bulk heterojunction solar cells: Surface recombination and charge transfer state distribution," *Physical Review B*, vol. 80, 2009.
- [127] W. Melitz, J. Shen, A. C. Kummel, and S. Lee, "Kelvin probe force microscopy and its application," *Surface science reports*, vol. 66, pp. 1-27, 2011.
- [128] P. Faßl, "Exploration of Properties, Stability and Reproducibility of Perovskite Solar Cells," 2019.
- [129] B. A. Courtright and S. A. Jenekhe, "Polyethylenimine interfacial layers in inverted organic photovoltaic devices: Effects of ethoxylation and molecular weight on efficiency and temporal stability," *ACS applied materials & interfaces*, vol. 7, pp. 26167-26175, 2015.
- [130] S. Woo, W. Hyun Kim, H. Kim, Y. Yi, H. K. Lyu, and Y. Kim, "8.9% single-stack inverted polymer solar cells with electron-rich polymer nanolayer-modified inorganic electron-collecting buffer layers," *Advanced Energy Materials*, vol. 4, p. 1301692, 2014.
- [131] C. Wang, C. J. Mueller, E. Gann, A. C. Liu, M. Thelakkat, and C. R. McNeill, "Influence of fluorination on the microstructure and performance of diketopyrrolopyrrole-based polymer solar cells," *Journal of Polymer Science Part B: Polymer Physics*, vol. 55, pp. 49-59, 2017.
- [132] P. Ye, Y. Chen, J. Wu, X. Wu, S. Yu, W. Xing, *et al.*, "Wide bandgap small molecular acceptors for low energy loss organic solar cells," *Journal of Materials Chemistry C*, vol. 5, pp. 12591-12596, 2017.
- [133] M. Park and J. W. Jung, "Anthracene-based perylene diimide electron-acceptor for fullerene-free organic solar cells," *Dyes and Pigments*, vol. 143, pp. 301-307, 2017.
- [134] X. Jia, N. Wu, J. Wei, L. Zhang, Q. Luo, Z. Bao, *et al.*, "A low-cost and low-temperature processable zinc oxide-polyethylenimine (ZnO: PEI) nano-composite as cathode buffer layer for organic and perovskite solar cells," *Organic Electronics*, vol. 38, pp. 150-157, 2016.
- [135] H.-C. Chen, S.-W. Lin, J.-M. Jiang, Y.-W. Su, and K.-H. Wei, "Solution-processed zinc oxide/polyethylenimine nanocomposites as tunable electron transport layers for highly efficient bulk heterojunction polymer solar cells," *ACS applied materials & interfaces*, vol. 7, pp. 6273-6281, 2015.

- [136] C. Liu, Z. Li, X. Zhang, W. Guo, L. Zhang, and S. Ruan, "Annealing-free ZnO: PEI composite cathode interfacial layer for efficient organic solar cells," *ACS Photonics*, vol. 4, pp. 2952-2958, 2017.
- [137] S. Rasool, V. Van Doan, H. K. Lee, S. K. Lee, J.-C. Lee, S.-J. Moon, *et al.*, "Enhanced photostability in polymer solar cells achieved with modified electron transport layer," *Thin Solid Films*, vol. 669, pp. 42-48, 2019.
- [138] B. A. MacLeod, B. J. T. De Villiers, P. Schulz, P. F. Ndione, H. Kim, A. J. Giordano, *et al.*, "Stability of inverted organic solar cells with ZnO contact layers deposited from precursor solutions," *Energy & Environmental Science*, vol. 8, pp. 592-601, 2015.
- [139] C. C. Wu, Y. T. Lin, K. T. Wong, R. T. Chen, and Y. Y. Chien, "Efficient organic blue-light-emitting devices with double confinement on terfluorenes with ambipolar carrier transport properties," *Advanced Materials*, vol. 16, pp. 61-65, 2004.
- [140] S. Trost, K. Zilberberg, A. Behrendt, A. Polywka, P. Görrn, P. Reckers, *et al.*, "Overcoming the "light-soaking" issue in inverted organic solar cells by the use of Al: ZnO electron extraction layers," *Advanced Energy Materials*, vol. 3, pp. 1437-1444, 2013.
- [141] Y. J. Cho and H. Aziz, "Root causes of the limited electroluminescence stability of organic light-emitting devices made by solution-coating," *ACS applied materials & interfaces*, vol. 10, pp. 18113-18122, 2018.
- [142] Q. Wang, B. Sun, and H. Aziz, "Exciton-Polaron-induced aggregation of wide-bandgap materials and its implication on the electroluminescence stability of phosphorescent organic light-emitting devices," *Advanced Functional Materials*, vol. 24, pp. 2975-2985, 2014.
- [143] A. Manor, E. A. Katz, T. Tromholt, and F. C. Krebs, "Enhancing functionality of ZnO hole blocking layer in organic photovoltaics," *Solar Energy Materials and Solar Cells*, vol. 98, pp. 491-493, 2012.
- [144] J. Olivier, B. Servet, M. Vergnolle, M. Mosca, and G. Garry, "Stability/instability of conductivity and work function changes of ITO thin films, UV-irradiated in air or vacuum: Measurements by the four-probe method and by Kelvin force microscopy," *Synthetic Metals*, vol. 122, pp. 87-89, 2001.
- [145] A. Turak, "Interfacial degradation in organic optoelectronics," *RSC advances*, vol. 3, pp. 6188-6225, 2013.
- [146] M. Girtan and M. Rusu, "Role of ITO and PEDOT: PSS in stability/degradation of polymer: fullerene bulk heterojunctions solar cells," *Solar Energy Materials and Solar Cells*, vol. 94, pp. 446-450, 2010.
- [147] L. G. Mar, P. Y. Timbrell, and R. N. Lamb, "An XPS study of zinc oxide thin film growth on copper using zinc acetate as a precursor," *Thin Solid Films*, vol. 223, pp. 341-347, 1993.
- [148] H. Tillborg, A. Nilsson, B. Hernnäs, N. Mårtensson, and R. Palmer, "X-ray and UV photoemission studies of mono-, bi- and multilayers of physisorbed molecules: O<sub>2</sub> and N<sub>2</sub> on graphite," *Surface science*, vol. 295, pp. 1-12, 1993.
- [149] S. Bai, Y. Jin, X. Liang, Z. Ye, Z. Wu, B. Sun, *et al.*, "Ethanedithiol treatment of solution-processed ZnO thin films: controlling the intragap states of electron transporting interlayers for efficient and stable inverted organic photovoltaics," *Advanced energy materials*, vol. 5, p. 1401606, 2015.
- [150] D. Di Carlo Rasi and R. A. Janssen, "Advances in solution-processed multijunction organic solar cells," *Advanced Materials*, vol. 31, p. 1806499, 2019.
- [151] J. Yu, Y. Xi, C. C. Chueh, D. Zhao, F. Lin, L. D. Pozzo, *et al.*, "A Room-Temperature Processable PDI-Based Electron-Transporting Layer for Enhanced Performance in PDI-Based Non-Fullerene Solar Cells," *Advanced Materials Interfaces*, vol. 3, p. 1600476, 2016.



- [152] Z. Zhao, J. He, J. Wang, W. Chen, N. Wang, Y. Zhang, *et al.*, "A water/alcohol-soluble copolymer based on fluorene and perylene diimide as a cathode interlayer for inverted polymer solar cells," *Journal of Materials Chemistry C*, vol. 3, pp. 4515-4521, 2015.
- [153] L. Chen, C. Li, and K. Müllen, "Beyond perylene diimides: synthesis, assembly and function of higher rylene chromophores," *Journal of Materials Chemistry C*, vol. 2, pp. 1938-1956, 2014.
- [154] C. R. Harding, J. Cann, A. Laventure, M. Sadeghianlemraski, M. Abd-Ellah, K. R. Rao, *et al.*, "Acid dyeing for green solvent processing of solvent resistant semiconducting organic thin films," *Materials Horizons*, vol. 7, pp. 2959-2969, 2020.
- [155] A. Spies, M. List, T. Sarkar, and U. Würfel, "On the Impact of Contact Selectivity and Charge Transport on the Open-Circuit Voltage of Organic Solar Cells," *Advanced Energy Materials*, vol. 7, p. 1601750, 2017.
- [156] S. Wilken, J. r. Parisi, and H. Borchert, "Role of oxygen adsorption in nanocrystalline ZnO interfacial layers for polymer–fullerene bulk heterojunction solar cells," *The Journal of Physical Chemistry C*, vol. 118, pp. 19672-19682, 2014.
- [157] R. Street, M. Schoendorf, A. Roy, and J. Lee, "Interface state recombination in organic solar cells," *Physical Review B*, vol. 81, p. 205307, 2010.
- [158] B. Chen, X. Qiao, C.-M. Liu, C. Zhao, H.-C. Chen, K.-H. Wei, *et al.*, "Effects of bulk and interfacial charge accumulation on fill factor in organic solar cells," *Applied Physics Letters*, vol. 102, p. 86\_1, 2013.
- [159] Z. Wu, "Impact of metal oxide/bulk-heterojunction interface on performance of organic solar cells," 2016.
- [160] J. C. Blakesley and D. Neher, "Relationship between energetic disorder and open-circuit voltage in bulk heterojunction organic solar cells," *Physical Review B*, vol. 84, p. 075210, 2011.
- [161] V. V. Brus, "Light dependent open-circuit voltage of organic bulk heterojunction solar cells in the presence of surface recombination," *Organic Electronics*, vol. 29, pp. 1-6, 2016.
- [162] M. Kröger, S. Hamwi, J. Meyer, T. Riedl, W. Kowalsky, and A. Kahn, "Role of the deep-lying electronic states of MoO<sub>3</sub> in the enhancement of hole-injection in organic thin films," *Applied physics letters*, vol. 95, p. 251, 2009.
- [163] T. Kuwabara, C. Tamai, Y. Omura, T. Yamaguchi, T. Taima, and K. Takahashi, "Effect of UV light irradiation on photovoltaic characteristics of inverted polymer solar cells containing sol–gel zinc oxide electron collection layer," *Organic Electronics*, vol. 14, pp. 649-656, 2013.
- [164] P.-R. Huang, Y. He, C. Cao, and Z.-H. Lu, "The origin of the high work function of chlorinated indium tin oxide," *NPG Asia Materials*, vol. 5, pp. e57-e57, 2013.
- [165] S. Zhang, S.-H. Wei, and A. Zunger, "Intrinsic n-type versus p-type doping asymmetry and the defect physics of ZnO," *Physical Review B*, vol. 63, p. 075205, 2001.
- [166] J. Reinhardt, M. Grein, C. Bühler, M. Schubert, and U. Würfel, "Identifying the Impact of Surface Recombination at Electrodes in Organic Solar Cells by Means of Electroluminescence and Modeling," *Advanced Energy Materials*, vol. 4, p. 1400081, 2014.
- [167] X. Du, T. Heumueller, W. Gruber, O. Almora, A. Classen, J. Qu, *et al.*, "Unraveling the microstructure-related device stability for polymer solar cells based on nonfullerene small-molecular acceptors," *Advanced Materials*, vol. 32, p. 1908305, 2020.
- [168] M. Sadeghianlemraski, C. R. Harding, G. C. Welch, and H. Aziz, "Significant Photostability Enhancement of Inverted Organic Solar Cells by Inserting an N-Annulated Perylene Diimide (PDIN-H) between the ZnO Electron Extraction Layer and the Organic Active Layer," *ACS Applied Energy Materials*, vol. 3, pp. 11655-11665, 2020.

- [169] I. Lee, J. Noh, J.-Y. Lee, and T.-S. Kim, "Cooptimization of Adhesion and Power Conversion Efficiency of Organic Solar Cells by Controlling Surface Energy of Buffer Layers," *ACS applied materials & interfaces*, vol. 9, pp. 37395-37401, 2017.
- [170] R. Phatak, T. Tsui, and H. Aziz, "Dependence of dark spot growth on cathode/organic interfacial adhesion in organic light emitting devices," *Journal of Applied Physics*, vol. 111, p. 054512, 2012.
- [171] K. P. Musselman, S. Albert-Seifried, R. L. Hoyer, A. Sadhanala, D. Muñoz-Rojas, J. L. MacManus-Driscoll, *et al.*, "Improved exciton dissociation at semiconducting polymer: ZnO donor: Acceptor interfaces via nitrogen doping of ZnO," *Advanced functional materials*, vol. 24, pp. 3562-3570, 2014.
- [172] S. Marchant and P. Foot, "Poly (3-hexylthiophene)-zinc oxide rectifying junctions," *Journal of materials science: materials in electronics*, vol. 6, pp. 144-148, 1995.
- [173] U. Hörmann, J. Kraus, M. Gruber, C. Schuhmair, T. Linderl, S. Grob, *et al.*, "Quantification of energy losses in organic solar cells from temperature-dependent device characteristics," *Physical Review B*, vol. 88, p. 235307, 2013.
- [174] N. Khare, M. Z. Ansari, R. L. Hoyer, D. C. Iza, and J. L. MacManus-Driscoll, "Elucidation of barrier homogeneity in ZnO/P3HT: PCBM junctions through temperature dependent I-V characteristics," *Journal of Physics D: Applied Physics*, vol. 49, p. 275302, 2016.
- [175] J. Wei, C. Zhang, G. Ji, Y. Han, I. Ismail, H. Li, *et al.*, "Roll-to-roll printed stable and thickness-independent ZnO: PEI composite electron transport layer for inverted organic solar cells," *Solar Energy*, vol. 193, pp. 102-110, 2019.
- [176] Z. Liang, Q. Zhang, O. Wiranwetchayan, J. Xi, Z. Yang, K. Park, *et al.*, "Effects of the morphology of a ZnO buffer layer on the photovoltaic performance of inverted polymer solar cells," *Advanced Functional Materials*, vol. 22, pp. 2194-2201, 2012.
- [177] H.-J. Park, K.-H. Lee, B. Kumar, K.-S. Shin, S.-W. Jeong, and S.-W. Kim, "Inverted organic solar cells with ZnO thin films prepared by sol-gel method," *Journal of Nanoelectronics and Optoelectronics*, vol. 5, pp. 135-138, 2010.
- [178] Z. Lin, J. Chang, J. Zhang, C. Jiang, J. Wu, and C. Zhu, "A work-function tunable polyelectrolyte complex (PEI: PSS) as a cathode interfacial layer for inverted organic solar cells," *Journal of Materials Chemistry A*, vol. 2, pp. 7788-7794, 2014.
- [179] K. Zhang, K. Gao, R. Xia, Z. Wu, C. Sun, J. Cao, *et al.*, "High-performance polymer tandem solar cells employing a new n-type conjugated polymer as an interconnecting layer," *Advanced Materials*, vol. 28, pp. 4817-4823, 2016.
- [180] A. Martínez-Otero, Q. Liu, P. Mantilla-Perez, M. M. Bajo, and J. Martorell, "An extremely thin and robust interconnecting layer providing 76% fill factor in a tandem polymer solar cell architecture," *Journal of Materials Chemistry A*, vol. 3, pp. 10681-10686, 2015.
- [181] A. R. bin Mohd Yusoff, D. Kim, H. P. Kim, F. K. Shneider, W. J. da Silva, and J. Jang, "A high efficiency solution processed polymer inverted triple-junction solar cell exhibiting a power conversion efficiency of 11.83%," *Energy & Environmental Science*, vol. 8, pp. 303-316, 2015.

## Appendix A

### Supplementary Information for Chapter 4

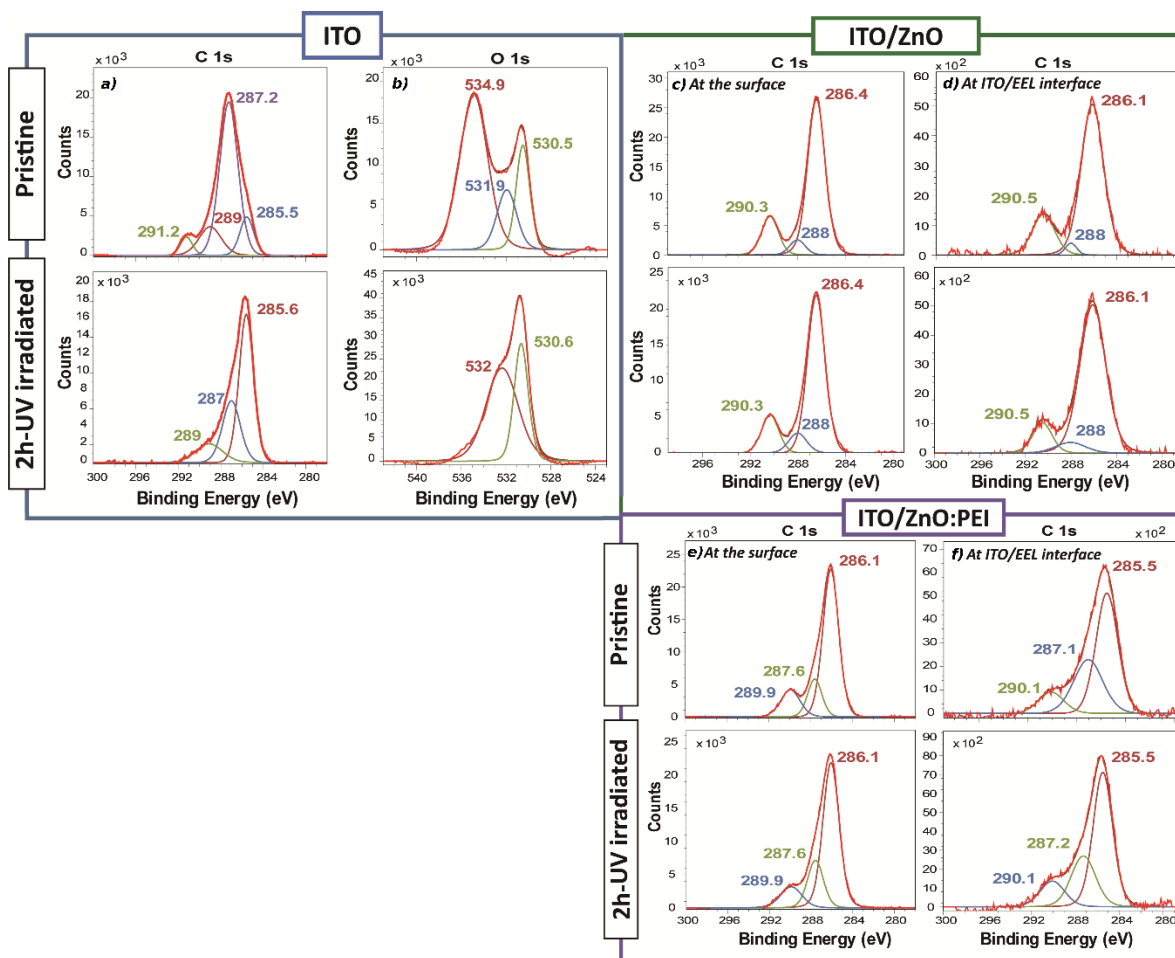


**Figure S4. 1.** C 1s and O 1s peaks of pristine and 2h-UV-irradiated ITO (left), and C 1s peaks of pristine and 2h-UV-irradiated ITO/ZnO and ITO/ZnO:PEI (right), at the surface versus at the ITO/EEL interface.

## Appendix B

### Supplementary Information for Chapter 6

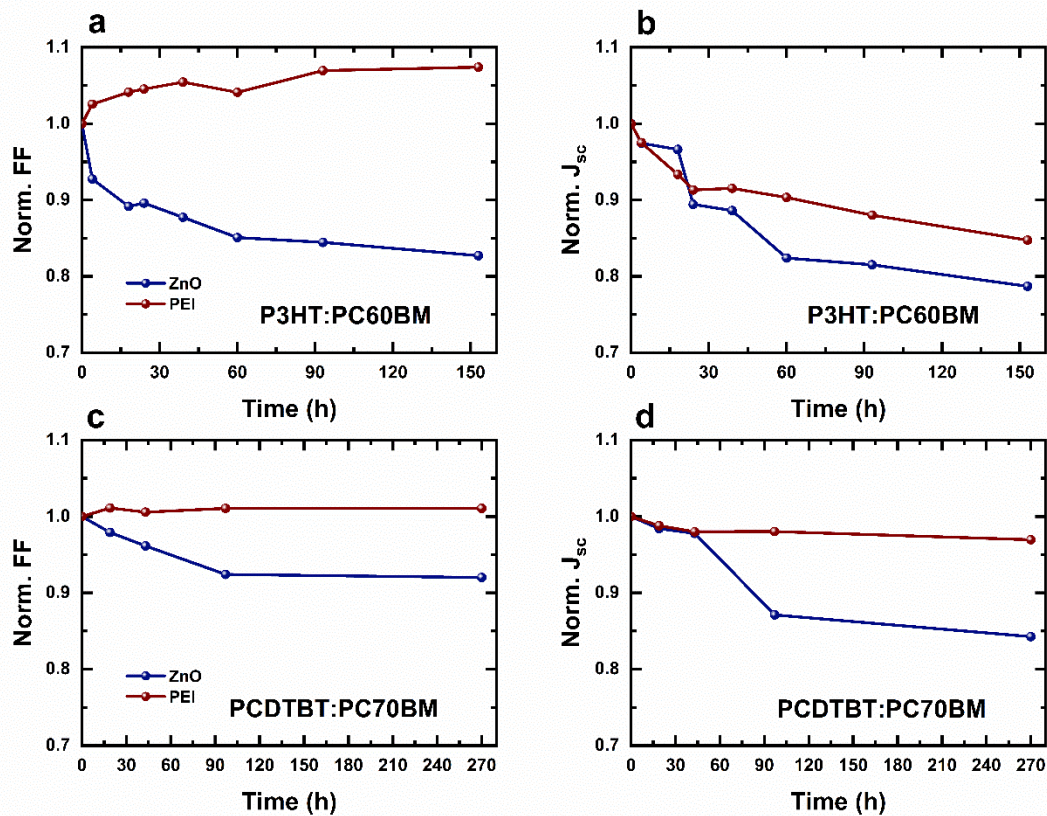


**Figure S6. 1.** (a) & (c): Normalized FF, and (b) & (d) Normalized  $J_{sc}$ , versus time under continuous UV illumination of OSCs with the ZnO (blue circles), and PEI (red circles) EELs; P3HT:PC60BM BHJ system (top), and PCDTBT:PC70BM BHJ system (bottom).

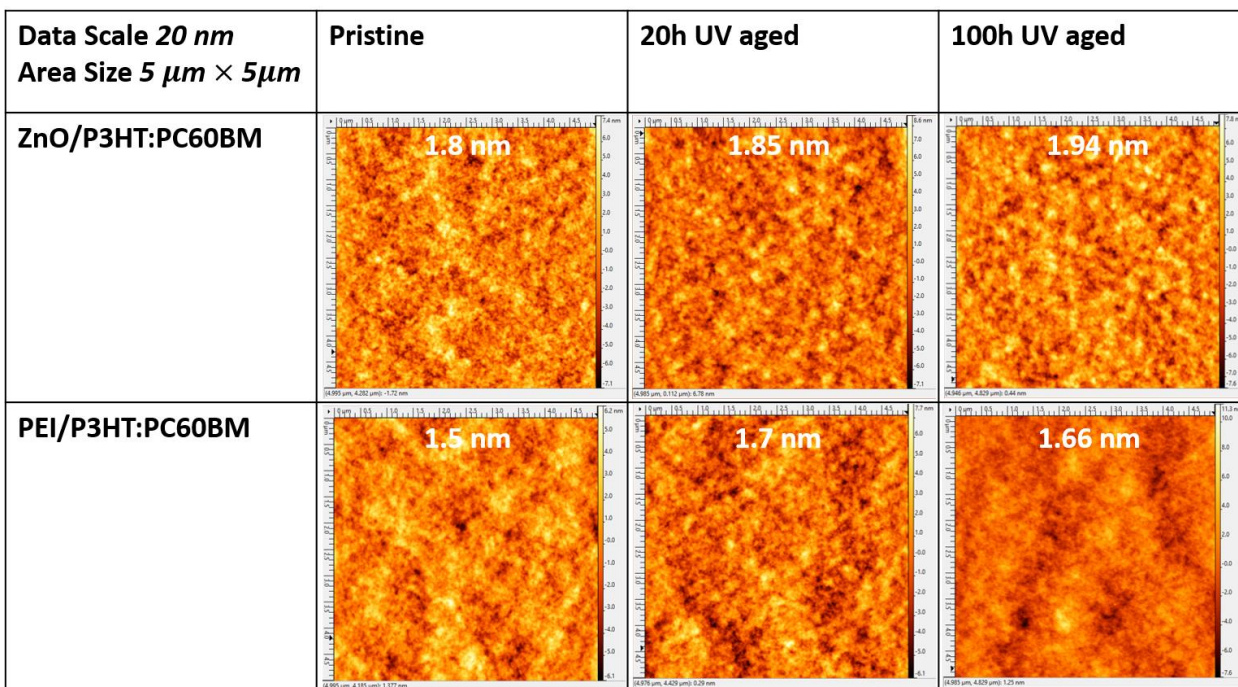


**Figure S6. 2.** AFM images of the fresh and after different time intervals of UV aging of ZnO/P3HT:PC60BM (first row) and PEI/P3HT:PC60BM (second row). Roughness values are provided within each image.

## Appendix C

### Supplementary Information for Chapter 7

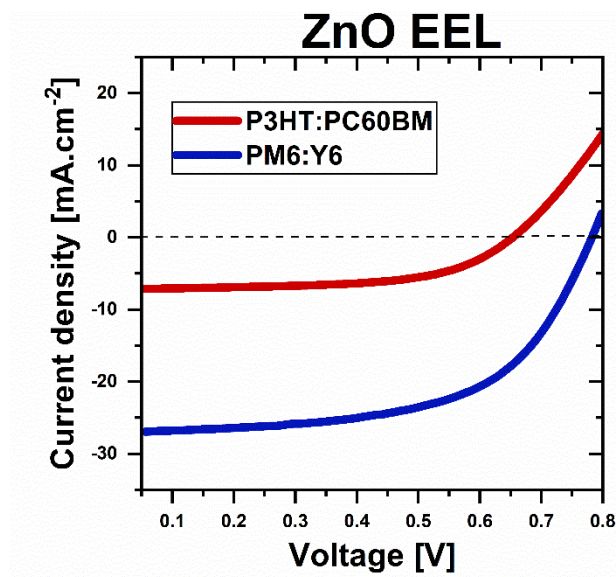


**Figure S7. 1.** Illuminated  $J$ - $V$  characteristics of P3HT:PC60BM (red curve) and PM6:Y6 (blue curve) OSCs with the ZnO EEL. The cells were measured under 1-sun AM1.5G illumination.

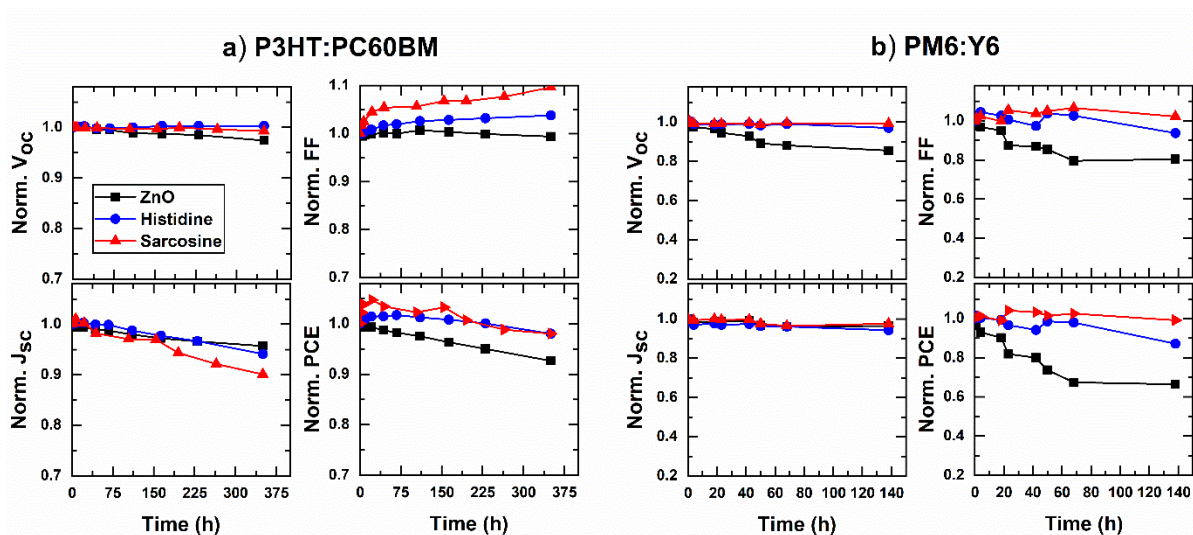


**Figure S7. 2.** Normalized  $V_{oc}$ , FF,  $J_{sc}$ , and PCE versus time of (a) P3HT:PC60BM and (b) PM6:Y6 OSCs with ZnO (blue squares), Histidine (green circles), and Sarcosine (red triangles) EELs. The cells were stored in a  $N_2$ -filled atmosphere in the dark to serve as a control.

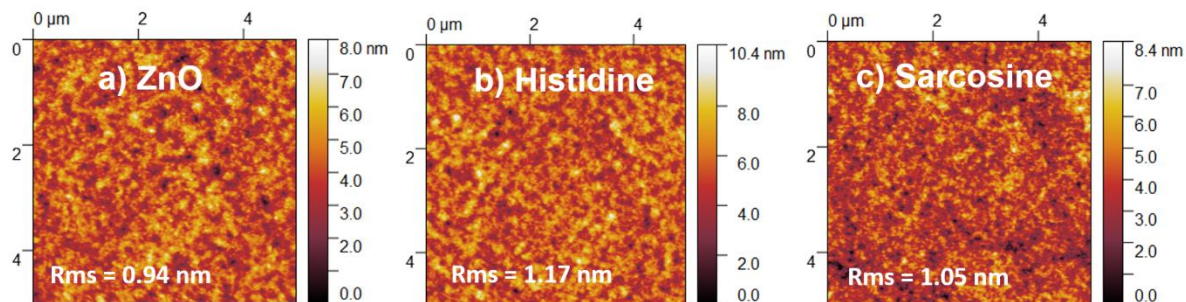


**Figure S7. 3.** AFM images of PM6:Y6 on a) ZnO, b) Histidine, and c) Sarcosine. Roughness values are shown in each image.

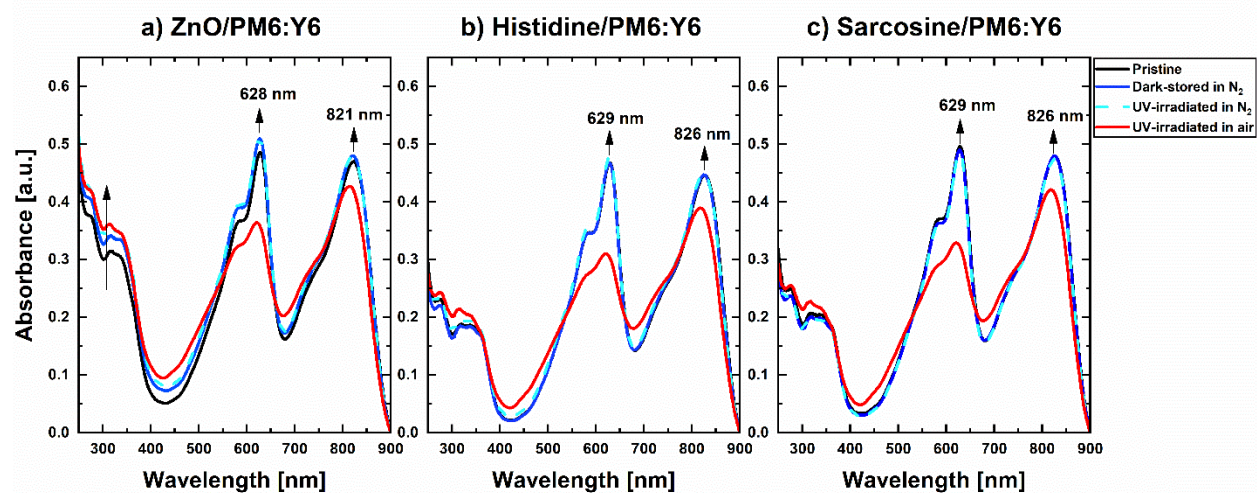


**Figure S7. 4.** UV-Vis absorption spectra of PM6:Y6 films coated on a) ZnO, b) Histidine, and c) Sarcosine; collected from pristine samples, after storage in  $N_2$  (solid blue line), after UV irradiation in  $N_2$  (dotted blue lines) and air (red lines).

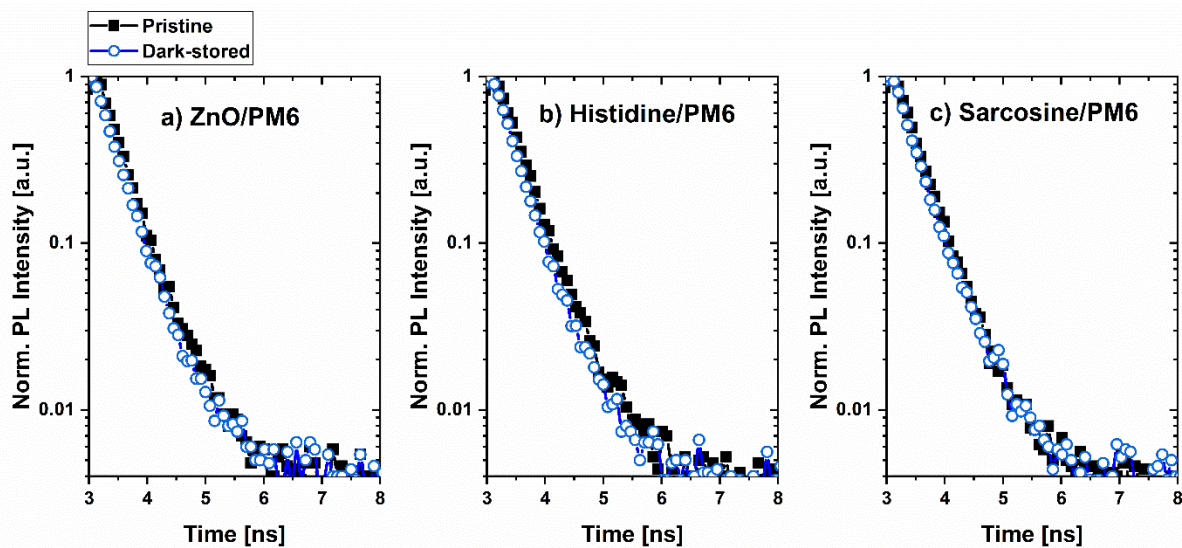


**Figure S7. 5.** Normalized TRPL spectra of pristine and dark-stored a) ZnO/PM6, b) Histidine/PM6, and c) Sarcosine/PM6.



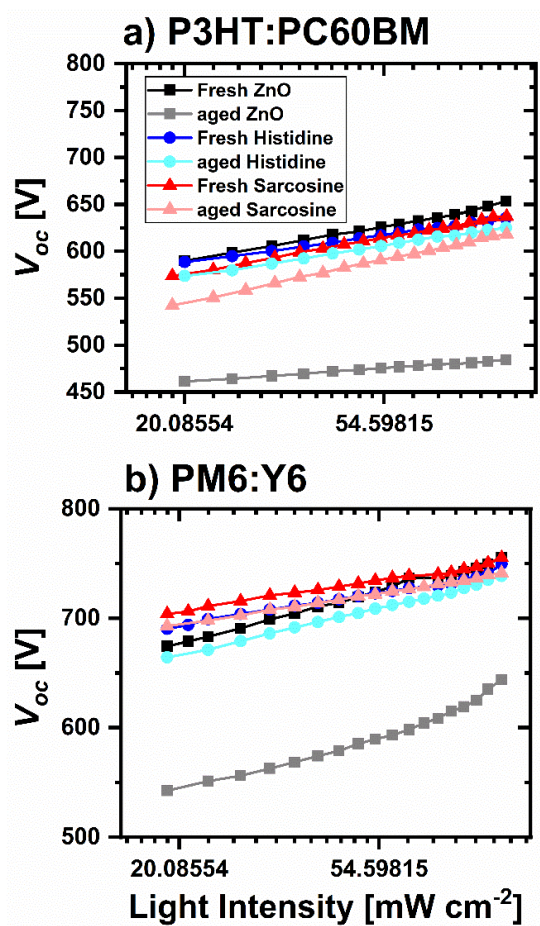


**Figure S7. 6.**  $V_{oc}$  versus the natural logarithm of light intensity of (a) P3HT:PC60BM (Fresh vs. UV-irradiated) cells and (b) PM6:Y6 (Fresh vs. Dark-stored) cells. Aged means after UV-irradiation in (a) and after dark storage in (b).

**Table S7. 1.** Values of alpha ( $\alpha$ ), extracted from the slope of the linear fit in Figure 3. The Aged cells refer to the UV-irradiated cells for the P3HT:PC60BM case and the Dark-stored cells for the PM6:Y6 case.

	P3HT:PC60BM			PM6:Y6		
	ZnO	Histidine	Sarcosine	ZnO	Histidine	Sarcosine
Fresh cells	0.99	1	0.97	0.94	0.97	0.98
Aged cells	1.04	1.06	1	0.94	0.99	0.99

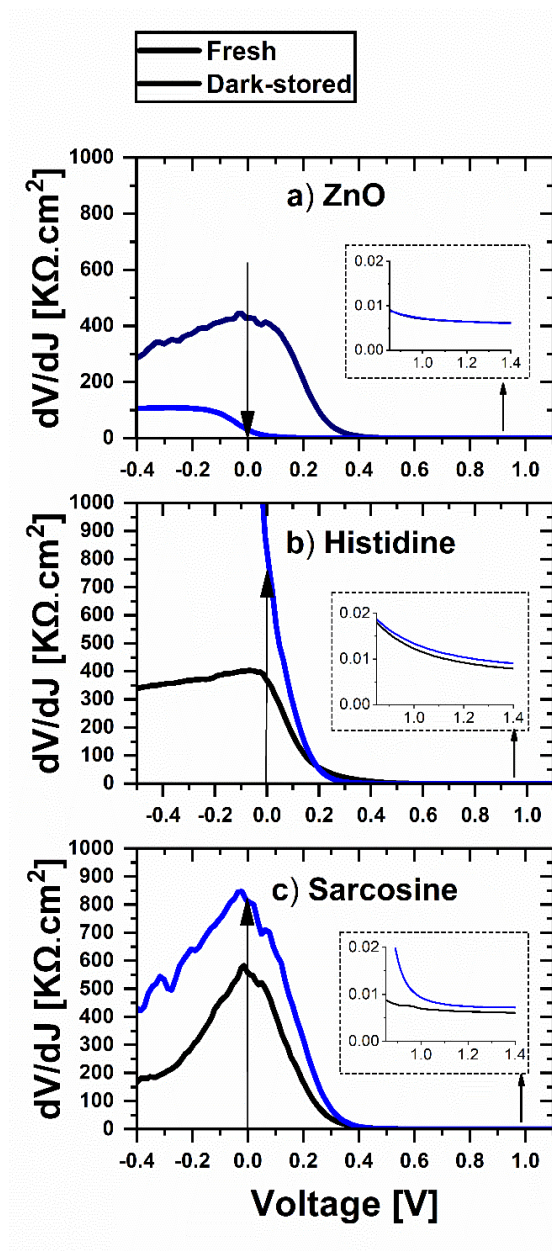


**Figure S7. 7.** Differential resistance ( $dV/dJ$ ) versus the applied voltage, extracted from dark  $J$ - $V$  characteristics of PM6:Y6 OSCs with (a) ZnO, (b) Histidine, and (c) Sarcosine. Shunt and series resistance values were extracted at voltages around 0 V and above 0.8 V, respectively. The data is obtained from the fresh cells and after their storage in the dark.

## Appendix D

### **Potential Benefits of Polyethyleneimine as an Electron Extraction Layer for Inverted Organic Solar Cells' Manufacturing**

*This work has been published in Sadeghianlemraski, M., and Aziz, H., Organic, Hybrid, and Perovskite Photovoltaics XXII. Vol. 11809. International Society for Optics and Photonics, 2021. It has been reproduced with permission from the publisher.*

#### **Introduction**

Although the solution processability of OSCs made them a cost-effective and environmentally-friendly solar technology and enabled the roll-to-roll fabrication of OSCs, solution-based solar cells intrinsically have less viability [7]. In addition to ZnO susceptibility to photodegradation established in Chapter 5 and 6, ZnO does not meet many requirements essential for the manufacturing and widespread application of solution-based OSCs. For instance, large-scale aggregation of pure ZnO inks causes poor ink stability [175]. In addition, OSCs with ZnO EELs show high sensitivity to the thickness variation of the ZnO layer [176, 177]. Recently, Wei et al. [175] showed that mixing ZnO nanoparticles with PEI provides not only a highly stable ink but also a low sensitivity to EEL-thickness variations for efficient large-area printed OSCs.

These challenges as well as an intrinsic incompatibility between ZnO as an inorganic metal oxide and the organic active layer [85, 86, 105, 178] led to the introduction of polymeric EELs, which benefit from the feasibility of tuning their optoelectrical and physical properties by molecular design and material synthesis. However, the application of several polymeric EELs has been limited due to the lack of solvent-robustness for solution-processed multilayer devices. Compatibility with solution-processed multilayer deposition is an essential factor in the EEL selection since solvent erosion of EELs in the bilayer EEL structures or during subsequent solution-based active-layer processing (in inverted devices) can impact charge selectivity and recombination [47, 50, 179-181]. Therefore, aside from charge selectivity, stability, and green-solvent processability, an EEL should be robust to both its processing solvents (for bilayer EELs) and to common organic solvents (for the subsequent active layer processing) to be a viable candidate for ZnO replacement.

As already discussed, among polymeric EELs, PEI has drawn a great deal of attention recently [26-28]. Considering the abovementioned critical requirements for EELs and having established (Chapter 5 & 6) that PEI outperforms ZnO in photostability while equally providing initial charge selectivity and green-solvent processability, it is imperative to explore its temporal stability and solvent-robustness. Thus, in this work, we compared the behavior of inverted OSCs with pristine PEI and N<sub>2</sub>-stored PEI EELs, utilizing for that purpose the P3HT:PC60BM OSC donor:acceptor system. We performed this experiment to test the stability of the PEI film over time, which is important when any gaps occur between the OSC manufacturing processes. Remarkably, our findings suggest that PEI is stable over time and that the time gap between PEI deposition and the active layer solution process does not affect solar cell performance and photostability. Additionally, we immersed PEI layers (on ITO) to potential processing solvents (1-propanol and/or toluene) before deposition of the active layer. Comparing the behavior of inverted OSCs with pristine PEI and solvent-immersed PEI EELs reveals that soaking the PEI film in the solvents does not significantly impact OSC performance and photostability. This observation along with XPS measurements point to the strong adhesion of the processed-PEI film to ITO, making the film insoluble and robust to solvents and preventing solvent-induced erosion during subsequent solution-based processing. These benefits of PEI demonstrate its potential as an EEL and give us much latitude during OSC fabrication and reduce the current OSC stringent manufacturing targets.

## Results and Discussion

To study the solvent-robustness and temporal stability of PEI film, we fabricated inverted OSCs with the structure of ITO/PEI (~5nm)/P3HT:PC60BM/MoO<sub>3</sub>/Al. Then, we compared the PV properties and photostability of different sets of OSCs for each case.

### Solvent-Robustness of PEI Film

First, we investigated the solvent-robustness of PEI to 1-propanol, its processing solvent, and toluene, a common organic solvent. **Figure AD.1** schematically shows the solvent-soaking process. After processing the PEI film, it is soaked in a Petri dish, filled with the solvent of interest, for 20 min before deposition of the active layer. Table AD.1 provides the PV parameters of OSCs with pristine PEI (as a control) and solvent-soaked PEI. It can be seen that soaking the PEI film in 1-propanol has an

essentially negligible impact on device performance, with respective efficiencies of 3.265 % and 3.158 % for OSCs with and without solvent soaking. Immersing the PEI layer to toluene as a common organic solvent also had minimal effects on the final device performance, with a PCE of 3.025 % (Table AD.1).

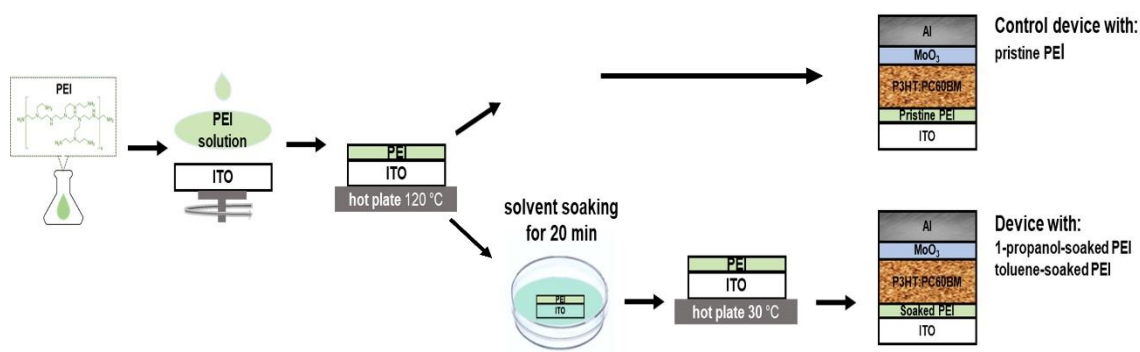


**Figure AD. 1.** Schematic illustrations of the device fabrication sequence, including the solvent exposure process.

**Table AD. 1.** PV parameters of OSCs with pristine PEI as a control, PEI soaked in 1-propanol, and PEI soaked in toluene.

EEL	PV Parameters			
	$J_{sc}$ [mA.cm <sup>-2</sup> ]	$V_{oc}$ [V]	FF [%]	PCE [%]
<b>PEI (control)</b>	9.124	0.639	55.993	3.265
<b>PEI + 1-propanol</b>	9.595	0.638	51.607	3.158
<b>PEI + toluene</b>	8.374	0.642	56.279	3.025

Seeing that soaking PEI films to the solvents does not significantly affect the initial PV properties, we also tested if it may impact the OSCs' photostability. **Figure AD.2** shows the  $J_{sc}$ ,  $V_{oc}$ , FF, and PCE under UV irradiation normalized to their initial (i.e., time zero) values. As shown in the figure, devices with pristine PEI and those with solvent-soaked PEI are all equally stable under UV irradiation. This comparable photostability indicates that soaking PEI in 1-propanol and toluene solvents does not affect device stability under UV irradiation.

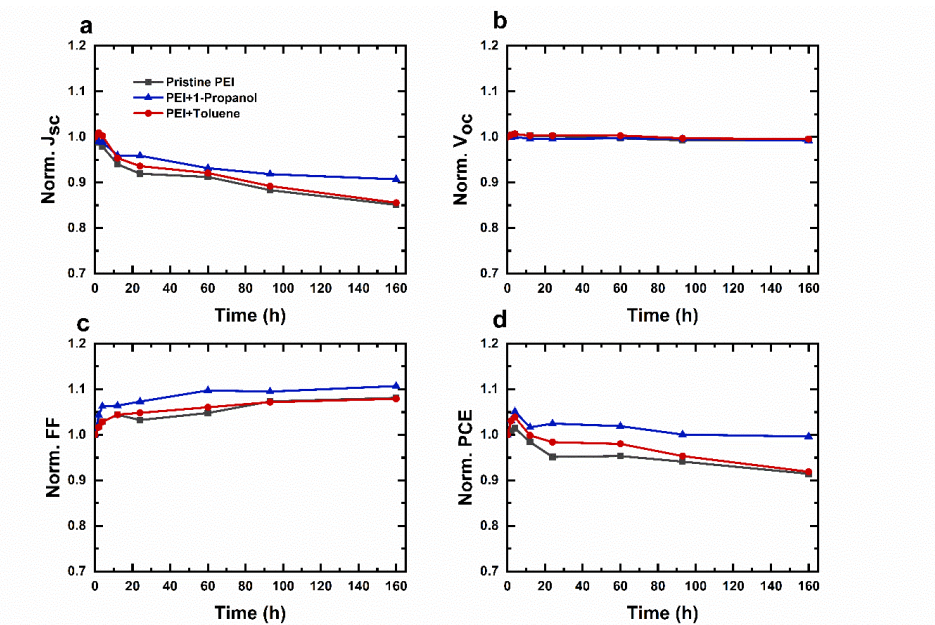


**Figure AD. 2.** Normalized  $J_{sc}$  (a),  $V_{oc}$  (b), FF (c), and PCE (d) versus time under continuous UV illumination of OSCs with pristine PEI (black squares), PEI soaked in 1-propanol (blue triangles), and PEI soaked in toluene (red circles).

Comparable efficiency and photostability of OSCs with the solvent-soaked PEI EEL and those with the pristine PEI EEL suggest two possible scenarios: (i) the PEI film does not come off by the solvents and strongly sticks to the surface and (ii) the PEI layer comes off by the solvents, but its earlier presence modifies the ITO surface permanently. To determine whether the PEI film is removed from the surface or not, we conducted XPS measurements on ITO/PEI and ITO/PEI+1-propanol samples. **Figure AD.3.a** shows N 1s peaks, as an indication of the amine group in PEI, for the ITO/PEI and ITO/PEI+1-propanol samples. Slight differences between the intensity of N 1s of the PEI and PEI+1-propanol sample suggest that the PEI layer remains after 1-propanol treatment and that the processed PEI layer can resist the solvent.

To glean some insights into the origins of the solvent-robustness of PEI deposited on ITO, we compared the interactions of PEI with ITO *vs.* PEI with glass by conducting XPS measurements on ITO/PEI and glass/PEI samples. **Figure AD.3.b** shows a  $\sim 2.4$  eV shift to higher binding energies in the N 1s peaks of the ITO/PEI sample relative to those of the glass/PEI samples, suggesting the presence of electronic interactions between ITO and PEI that leads to increased stability of electrons in  $N_2$

orbitals. These solid physical interactions confirm the strong adhesion of PEI to ITO, making PEI robust to solvents.

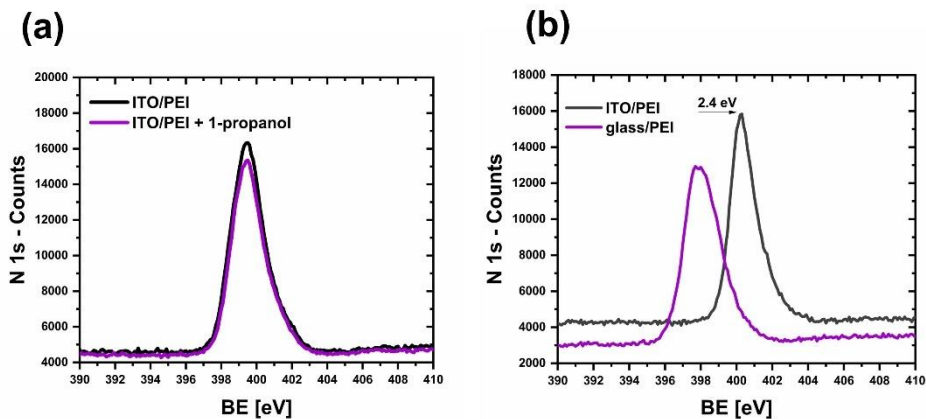


**Figure AD. 3.** (a) N 1s spectrum for pristine ITO/PEI sample and ITO/PEI sample soaked in 1-propanol. (b) N 1s spectrum for ITO/PEI and glass/PEI samples.

### Temporal stability of PEI film

To study the temporal stability of PEI, we fabricated inverted OSCs with fresh PEI and N<sub>2</sub>-stored PEI. For this purpose, after the substrates were cleaned, they were divided into two groups. PEI layers were deposited on ITO for one set while the other set was left as bare substrates. Then, after five days of storage in N<sub>2</sub>, PEI deposition was done on the other sets of samples (bare substrates). On the same day, the other OSC layers were deposited on both sets of samples using the same procedures and conditions followed with the earlier sets of OSCs. Generally, both the devices with fresh PEI and those with N<sub>2</sub>-stored PEI show comparable PV properties (Table AD.2), with the PCE of 2.229 % and 2.360 %, respectively. The cells with N<sub>2</sub>-stored PEI show slightly lower  $J_{sc}$ , exhibiting  $J_{sc}$  of 6.588 mA.cm<sup>-2</sup> compared to  $J_{sc}$  of 6.845 mA.cm<sup>-2</sup> of the cells with fresh PEI, respectively. Also, a somewhat higher FF of 55.931% is observed in cells with N<sub>2</sub>-stored PEI versus FF of 50.696% in the cells with fresh PEI, respectively. This finding suggests that PEI is stable over time, and the time gap between PEI deposition and the active layer coating does not affect solar cell performance. This high temporal stability of PEI clearly provides a significant advantage for OSC manufacturing. Notably, we repeated the same experiment with ZnO as an EEL; the OSCs with N<sub>2</sub>-stored ZnO did not exhibit reasonable performance (PCE ≤ 0.1 %), indicating higher compatibility of PEI over ZnO for OSC manufacturing.

**Table AD. 2.** PV parameters of organic solar cells with fresh and N<sub>2</sub>-stored PEI.

EEL	PV Parameters			
	$J_{sc}$ [mA.cm <sup>-2</sup> ]	$V_{oc}$ [V]	FF [%]	PCE [%]
Fresh PEI	6.845	0.642	50.696	2.229
N <sub>2</sub> -stored PEI	6.588	0.640	55.931	2.360

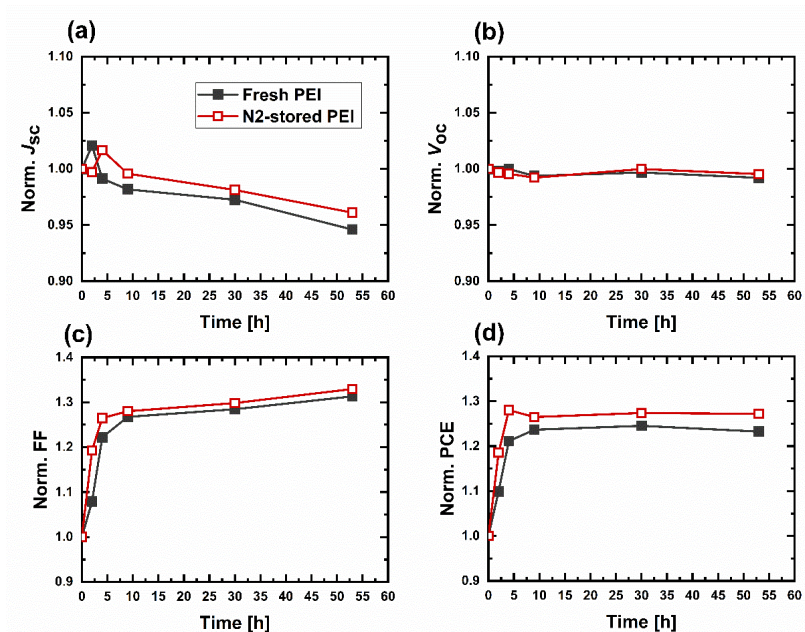


**Figure AD. 4.** Normalized  $J_{sc}$  (a),  $V_{oc}$  (b), FF (c), and PCE (d) versus time under continuous UV illumination of OSCs with the fresh PEI and N<sub>2</sub>-stored PEI EELs.

Knowing that the time gap between PEI deposition and the active layer solution process does not affect solar cell performance, we also test if it may influence the OSCs photostability. **Figure AD.4** depicts photostability data of OSCs with fresh PEI and of those with N<sub>2</sub>-stored PEI. The PV properties of both sets of devices remain essentially unchanged, and the cells exhibit comparable photostability behavior. This finding suggests that gaps between the PEI process and other fabrication procedures do not substantially affect device durability.



## **Conclusions**

The robustness of PEI to potential processing solvents (1-propanol and/or toluene) and its temporal stability have been studied. Results reveal that the soaking of PEI in the solvents has a negligible influence on device performance and photostability. Furthermore, XPS measurements reveal that adhesion of the PEI film to the surface of the ITO electrode is very strong so that PEI cannot be removed by its processing solvents or common organic solvents. Additionally, the temporal stability of the processed PEI film and its advantages for OSC performance and stability are demonstrated. We, therefore, suggest PEI as a potential environmentally-friendly EEL that opens up opportunities for the practical application of OSC devices by eliminating the need for precise control during manufacturing processes as well as by providing good OSC performance and stability.